KAUNAS UNIVERSITY OF TECHNOLOGY

AUDRIUS NEČIŪNAS

ALGORITHMS OF NUMERICAL SIMULATION OF ELASTIC WAVES PROPAGATING IN DISSIPATIVE ENVIRONMENTS

Doctoral Dissertation
Physical Sciences, Informatics (09P)

2018, Kaunas

This doctoral dissertation was prepared at Kaunas University of Technology, Faculty of Informatics, Department of Applied Informatics during the period of 2013–2017.

Scientific Supervisor:

Prof. Dr. Habil. Rimantas BARAUSKAS (Kaunas University of Technology, Physical Sciences, Informatics, 09P).

Doctoral dissertation has been published in:
http://ktu.edu

Editor:

Armandas Rumšas (Publishing Office “Technologija”)

ISBN 978-609-02-1482-4

The bibliographic information about the publication is available in the National Bibliographic Data Bank (NBDB) of the Martynas Mažvydas National Library of Lithuania.

KAUNO TECHNOLOGIJOS UNIVERSITETAS

AUDRIUS NEČIŪNAS

TAMPRIŲJŲ BANGŲ SKLIDIMO SLOPINANČIOSE TERPĖSE SKAITINIO MODELIAVIMO ALGORITMAI

Daktaro disertacija
Fiziniai mokslai, Informatika (09P)

2018, Kaunas

Disertacija rengta 2013-2017 metais Kauno technologijos universiteto Informatikos fakultete Taikomosios informatikos katedroje.

Mokslinis vadovas:

Prof. habil. dr. Rimantas BARAUSKAS (Kauno technologijos universitetas, fiziniai mokslai, informatika, 09P).

Interneto svetainės, kurioje skelbiama disertacija, adresas:
http://ktu.edu

Redagavo:

Inga Nanartonytė (leidykla “Technologija”)

ISBN 978-609-02-1482-4

Leidinio bibliografinė informacija pateikiama Lietuvos nacionalinės Martyno Mažvydo bibliotekos Nacionalinės bibliografijos duomenų banke (NBDB).

NOMENCLATURE

SAFEM – Semi Analytical Finite Element Method;
WFEM – Wave Finite Element Method;
WSFEM – Wave Spectral Finite Element Method;
SBFEM – Scaled Boundary Finite Element Method;
FEM – Finite Element Method;
BEM – Boundary Finite Element;
FFT – Fast Fourier transform;
SHM – Structural health monitoring;
NDT – Non-destructive testing;
dof – the number of degrees of freedom;
$\mathrm{Re}(\cdot)$ – the real part of a complex number;
$\mathrm{Im}(\cdot)$ – the imaginary part of a complex number;
ν – Poisson's ratio;
λ – wavelength;
k – wavenumber;
ω – angular frequency;
f – frequency;
σ – stress;
ε – strain;
t – time;
V – volume;
S – square;
c_{ph} – phase velocity;
c_{gr} – group velocity;
E – Young's modulus;
ζ – viscosity;
ρ – mass density;
i – complex unit;
δ – Kronecker's delta;
Q – quality factor;
$\boldsymbol{u}$ – displacement vector;
$\boldsymbol{M}$ – mass matrix;
$\boldsymbol{K}$ – stiffness matrix;
$\boldsymbol{D}$ – elasticity tensor.

TABLE OF CONTENTS

TABLE OF FIGURES

Introduction

The simulation of propagating waves is of primary importance in many engineering applications, such as planning ultrasonic measurement procedures, monitoring of the structural integrity of pipelines by analyzing pressure pulses propagation, earthquake waves propagation and many other types of real-life applications. Traditionally, the computational methods of wave propagation analysis in geometrically complex structures and environments use the finite element or the finite difference approaches. However, inherent shortcomings arise due to huge dimensionalities of the models in cases when the length of the analyzed waves is much lesser than the linear dimensions of the structure. The limit situation is the infinite wave propagation environment in one or several directions, which actually is extremely difficult to simulate by traditional FEM because fictitious wave reflections form artificially introduced boundaries of the computational domain. The existing techniques within traditional FEM which enable to cope with the infinite domains are the non-reflecting boundary condition (suitable only for acoustic waves), scaled-boundary FEM techniques and perfectly matched layers. However, the latter approaches are approximate, and they also require significant computational resources, anyway. The semi-analytical approaches such as the SAFE method seem to be promising as they enable their users to avoid the discretization of the structures along the infinite direction. Even though the principles of SAFE have been well-known for several decades, the approach is still underdeveloped as perfectly as the traditional FEM – therefore, further research is still necessary.

The guided waves in the waveguide (plate, bar, pipe, *etc.*) are described by their dispersion curves. The dispersion curves present the relationships of phase, group and energy velocities of the waves against the wave frequency. The SAFE method facilitates the calculation of dispersion curves for waveguides having uniform cross-section geometries along at least one direction. The finite element covers the discretization of the waveguide cross-section only. Along the wave propagation direction, the harmonic solutions in space and time are used. The expressions of such solutions use the exponential functions in the space of complex numbers. Similarly to the conventional FEM, the SAFEM enables to express forced time-dependent wave response analysis as a superposition of modal responses.

While there are many researches addressing waveguides in vacuum, SAFE modeling of traveling waves in dissipative environments is still a challenging task. It is caused by the fact that the traditional SAFE analyses presume the amplitude decay of the traveling wave as negligible and, therefore, certain mathematical simplifications of the FE formulation are possible. In the case of higher damping, such simplifications would lead to considerable errors of the solution. In this research, the SAFE formulation is extended in order to treat the wave propagation problems in viscous environments. The energy dissipation model is presented via Rayleigh damping (i.e., energy dissipation caused by material damping) and via the leaky wave, where the waveguide immersed into the perfect fluid is considered.

Research Object

The research object is the semi-analytical finite element models for simulation of guided waves in viscous environments.

Research Aim

The aim of the research is the development of algorithms for obtaining the propagating wave modal solutions and forced responses of wave propagation in the environments with a higher level of viscosity.

Research Tasks

1. To implement Semi Analytical Finite Element for extracting modal solutions of guided waves in waveguides surrounded by vacuum, where the level of Rayleigh damping requires to use solutions in terms of complex wavenumbers;
2. To obtain the forced response of the waveguide with internal Rayleigh damping placed in vacuum environment to external harmonic and non-harmonic loading;
3. To verify the forced wave propagation results obtained with SAFEM along a short propagation path by comparing them against the results obtained by the 3D FEM model which represents a bounded segment of the same waveguide;
4. To develop the SAFE model of a waveguide immersed into the perfect fluid and to obtain the corresponding dispersion curves;
5. To analyze the theoretical feasibility of obtaining the forced response for an immersed rectangular waveguide.

Scientific Novelty

The scientific novelty of this dissertation is in the extension of the SAFE models of unidirectional waveguides by incorporating the Rayleigh damping of the waveguide material. Differently from the already existing analyses, the formulation containing the complex conjugate wavenumbers has been used in order to obtain mathematically exact solutions along the wave propagation direction. A novelty of this work is also the transition from the earlier known immersed into the perfect fluid plate model to the immersed waveguide model.

Practical Relevance

The developed approach can facilitate the development and enhancement of the software for the computer simulation of guided wave propagation with the application to damped waveguides positioned in fluids. From the computational standpoint, the developed approaches enable to reduce the dimensionality of the models and thus save computer resources. From the standpoint of the engineering practice, such simulations facilitate the design of the wave- and vibrations-based non-destructive measurement procedures by predicting the wave responses from fault-free structures or the structures with internal faults.

Approbation of the Research Results

The main results of the dissertation are represented in 4 scientific publications: 2 in periodical scientific journals (ISI Web of Science) and 2 in international conference proceedings.

The Structure and Volume of the Dissertation

This doctoral dissertation consists of an introduction, 3 main chapters, conclusions, references and a list of publications. The main body of the doctoral dissertation is presented in 108 pages. The main part of the dissertation contains 54 figures and 112 entries in the reference list.

1 Review of Research Related to Short Wave Modeling

1.1 The Application of Guided Waves

Mechanical stresses and strains produced by a source which releases energy into the solid body or fluid will propagate away from the source as waves. Periodic excitation imposed on an elastic structure will cause its dynamic response as the elastic harmonic wave. One of the useful engineering applications of propagating waves lies in the field of ultrasonic measurements (UM) and Non-Destructive Testing (NDT). The waves in the bodies under analysis are excited in the ultrasonic frequency range by employing piezoelectric transducers. At such high frequencies, the generated wavelengths lie in the range of millimeters or even microns; therefore, they should be regarded as short waves with respect to the dimensions of the structures under investigation.

Ultrasonic measurement procedures evaluate particular properties of the material or find the locations of internal structural non-integrity by analyzing the registered properties of the waves propagating in the structure. The locations of flaws are detected by exciting the wave at one location of the structure and by registering its reflections produced by the defects.

Along with the conventional UM technique, the guided wave technique has emerged and is already well-established for the long-range inspection. The benefit of using a measurement system based on guided waves is the ability to travel long distances along the waveguide (Fig. 1.1). The waveguide is a specially designed structure for ensuring the transfer of the wave energy over a considerable distance. In the conventional NDT, only a relatively small area can be analyzed by high frequency bulk waves. Much wider areas can be analyzed by using guided waves as they are considerably longer. Guided wave inspection uses relatively low ultrasonic frequencies compared to those used in the conventional UM, typically between $10 - 100\ kHz$ [1],[2].

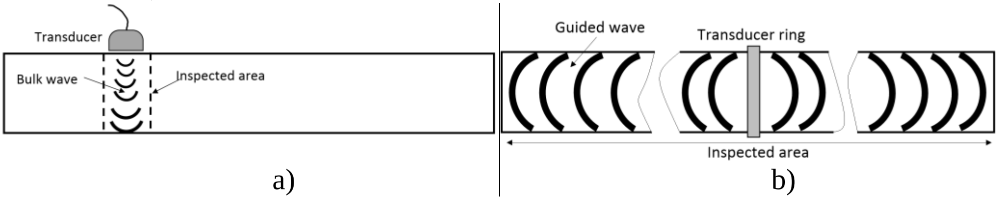

a) b)

Fig. 1.1. (a) Conventional ultrasonic testing; (b) Guided wave testing.

The guided elastic waves are widely used for the inspection of elongated structures for exploring the structural integrity or possible defects [3], [4], [5], [6]. The term *guided wave* is formed of multiple reflections from the side boundaries of the waveguide which add up to the wave traveling in the infinite direction of the waveguide. Guided waves can travel on the surface of semi-infinite solids (such as Rayleigh waves), on the interface between different material environments (such as Stoneley-Scholte waves), along homogenous or multilayered plates, in generic cross-section beams, axial symmetric rods and cylinders. Only the plate, cylinder and beam types are the *simplest waveguides*. Generally, any structure uniform (both in the geometrical and in the physical sense) in at least one direction can be regarded as a waveguide. For example, the simulation in waveguides consisting of carbon fiber reinforced plastics (CFRP) rods can help to find delamination regions in samples [7]. The inspected elongated structures, such as pipes and rails, are also treated as waveguides in many practical applications [8], [9]. UM could also be applied for measuring the viscosity of viscous substances surrounding the waveguide [10], the viscosity of fluid density [11], or the viscosity of the properties of frequency-dependent viscoelastic polymers [12], etc.

For the characterization of guided waves, dispersion curves are used which display the relationship of wave velocities against frequencies. There are a number of different types of waves which can propagate along the waveguides. The types of the waves are determined by their displacement shapes over the waveguide's cross-section, by the wave frequency and by the wavelength (even though, most commonly, the *wavenumber* – which is the inverse of the wavelength – is used). Such wave characteristics of each wave type refer to as the *wave mode*. Wave modes are the solutions to the homogenous wave equation. This means that such non-zero solutions corresponding to the modes are possible without any external excitation. They present the wave motions which are naturally inclined to propagate along this particular waveguide. Each mode of the waveguide represents a stationary traveling wave. Dispersion curves also provide information about the phase and group velocities of the waves at a particular frequency. This information provides the basis for the design of angle- and comb-type transducers used for ultrasonic inspection [13]. The calculations acquiring dispersion curves are necessary *apriori*. They provide a foundation for planning the inspection procedure. The wave dispersion phenomenon causes a distortion of the shape of the wave pulse when traveling a longer distance since the propagation velocity of each wave mode combined in the wavepulse as a superposition term may be different. This dispersion may reduce the resolution of UM, therefore, wave simulation analysis is crucially important for the understanding and evaluation of the effect caused by this phenomenon. In the engineering practice, the effect of dispersion is reduced by using the tone burst of a limited bandwidth in those ranges where the rate of the group velocity change with respect to time is minimal [14].

1.2 Calculating the Solutions for Guided Waves

The first theoretical approach to guided waves dates back to Pochhammer and Chree who were the first researchers to provide a solution in terms of dispersion curves of rod waveguides [15], [16]. The traveling wave solutions for plates were obtained by Rayleigh and Lamb. The dispersion curves of homogenous and isotropic plates can be analytically derived from the Rayleigh-Lamb equation [17], however, such solutions are available just for the waveguides of the simplest geometry [18].

The extension of the analytical approach is the Global matrix method. It is an exact method based on the superposition of bulk waves. The dispersion equations are formulated via interference of partial bulk waves which satisfy the boundary conditions of the waveguide [19]. For damped and/or leaky waves, solutions are as pairs of the modal frequency and the complex modal wavenumber which satisfy the dispersion equation. During the search for such pairs, some of them might be missed [20]. Moreover, the Global matrix method can be applied only to simple waveguides such as axisymmetric rods or multilayer plates which are uniform and homogenous within a layer in at least one direction.

Obtaining the dispersion characteristics of complex structures requires different numerical approaches, most often based on the finite element method (FEM). Many authors, such as Sorohan [9], Hladky-Hennion [21], Damljanovic and Weaver [22], and Zienkiewicz [23] have researched FEM application for propagating waves in waveguides. FEM is a robust and flexible tool widely preferred for solving general problems of physical behavior of structures of the generic geometry and material setup.

However, the traditional 3D finite element approach becomes unsuitable in cases of infinite domains. Propagating wave solutions require the infinity of the domain at least in one dimension in order to eliminate wave reflections which form a standing wave rather than a propagating one. On the other hand, the FE mesh density must be adjusted to the analyzed wavelengths. Usually, 20 to 30 FEs are necessary along the characteristic wavelength; therefore, huge dimensionality of the computational models is required in those cases when the wavelength is considerably smaller than the characteristic length of the structure.

1.3 Obtaining the Guided Waves Solutions by Using Semi-Analytical Methods

The dimensionality of 3D FE models of waveguides can be reduced by taking just a small representative segment of the waveguide structure by using the periodicity condition along the wave propagation direction. This enables to obtain the wave characteristics via Eigenproblem, where the whole number of wavelengths is contained along the length of the structure. This technique is used in the wave finite element method (WFEM) and is easily adopted in commercial FE software in order to reduce the computational resources for the simulation of propagating waves [24], [25] [26], [27]. However, in cases of complex structures, standard wave elements require cumbersome formulations due to the exact analytical wave solutions as the interpolation functions of the FE. Moreover, WFEM leads to numerical inaccuracies when short waves (compared to the length of the FE slice) are considered. Further development of WFEM is the Wave Spectral Finite Element Method (WSFEM). In this approach, the transfer matrix of the structural waveguide is obtained from a thin slice by using the conventional FEM. Then, dispersion relations are obtained from the transfer matrix and used to build the spectral element matrix. These spectral elements could be used to model homogenous waveguides with an invariant cross section over long distances [28].

Another approach based on the semi-analytical method that requires discretization of the boundary only is the Scaled Boundary Finite Element Method (SBFEM) [29], [30], [31], [32]. The Semi Analytical Finite Element Method (SAFE) requires the discretization of the cross-section in the waveguide and differs from SBFEM in terms of FE interpolation functions and leads to another form of the obtained Eigenvalue problem [33], [34], [35]. The common assumption for WFEM, SBFEM and SAFE is the separation of the wave displacement field along the propagation direction OZ from the displacements in other directions by using harmonic term e^{-ikz}. As in most FE formulations, the time domain is transformed to the frequency domain by using a harmonic term e^{-iwt}[36] which allows to calculate the steady state solutions via Eigenproblems formulated in real numbers. Whenever the material damping in a waveguide is present, much more difficult problems arise as the Eigenvalue problem in terms of complex numbers evolves. Thus solutions attenuated both in space in time can be expressed [37], [33], [38], [39]. However, such an approach still requires further mathematical and algorithmic elaborations, whereas the physical interpretation of the obtained complex modal solutions is not always obvious. Some of such problems are solved in this work by using SAFEM as a base for the computational approach.

1.4 Semi Analytical Finite Element Method

The SAFE methodology was first introduced by Lagasse [40] and Aalami [41]. Gavrić assumed that the displacement time law along the wave propagation direction is shifted by phase π/2 with respect to the in-plane displacement time law over the cross section of the waveguide. This shift allowed to formulate the Eigenvalue problem in terms of real symmetric matrices [42]. Viola, Marzani and Bartoli [43], [44] further developed this technique. They introduced the complex stiffness term which allowed simulation of the wave propagation in attenuating media.

The SAFE technique combines the analytical solution of the propagating wave along the length of the uniform waveguide with the FE solution of the 2D displacement field over the cross-section of the waveguide. Therefore, it enables the modeling of very short waves propagating over very long distances since the approximation of the displacement field along the length of the waveguide is not necessary. Simultaneously, the SAFE formulation employs only 2D FE discretization for obtaining the 3D solution of the propagating wave [30], [45].

Waves in infinite uniform structures such as rails, bars, beams, pipes, etc., were efficiently treated by applying SAFEM [46], [47]. The SAFE formulation was applied for calculating the wave propagation characteristics of fluid-filled composite pipes [38]. It enabled to solve guided wave dispersion relations in structures with a periodic geometrical pattern along the wave propagation direction. In this way, waves in a stranded wire [48], helical spring [49], laminar [50] waveguides or waves in a grooved aluminum plate [50] have been investigated. Waves in a thin elastic cylindrical shell were analyzed in [51], [52], [53] in order to predict vibrations and underwater acoustic radiations caused by hammer impacts. In addition to acquiring dispersion curves, SAFE applications also included modeling of piezoelectric transducers attached to waveguides and forced response computation [8, 22, 54, 55]. SAFEM and FEM were coupled to solve Lamb waves’ reflections at plate edges [56, 57].

1.5 Modeling Dissipative Environment

The propagating waves in real environments experience attenuation, the main sources of which are the internal material damping and the leaky surrounding environment. In the SAFE approach, the material damping was usually approximated by linear viscoelasticity by introducing the complex Young’s modulus [58–61]. However, the application of Rayleigh damping seems to have been absent in SAFEM until now, though this damping approximation is much more versatile. It is capable of accounting for linear viscoelasticity and introduce the mass-proportional, stiffness-proportional, as well as mass-stiffness-proportional damping. In this way the damping models resembling fluid loads may be constructed, as well as the creation of different laws of the damping level against frequency may be enabled. Therefore, mass Rayleigh damping was explored in this work.

There are many studies devoted to the investigation of waveguides in vacuum with the stress-free boundary condition on its sides (the so-called closed waveguides). However, the techniques that support a waveguide’s interaction with a leaky medium (open waveguides) are still under development. Concrete rods buried in soil, thin-walled pipes filled with a fluid and similar structures require modeling of the surrounding medium, which causes the propagating wave to attenuate due to the leakage of the energy. Leaky waves are also important in ultrasonic applications. When a leaky wave propagates, it quickly attenuates because of losing energy to the surroundings. For instance, a crack in the inspected structure can partially block the energy leakage and hence reduce attenuation. The size of the crack can be evaluated by measuring the amplitude of the leaky wave [62].

The leaky medium surrounding the waveguide is commonly assumed to be unbounded. This creates additional difficulties for computational modeling. An artificial infinity of the surrounding medium can create wave-absorbing regions [63, 64]. However, such absorbing regions require highly refined meshes, the number of FE in which may be much bigger than the number of FEs in the waveguide itself.

An approach combining SAFEM and the perfectly matched layer (PML) technique may be used for computing the leaky modes which carry energy away from the waveguide to the surroundings. Complex coordinates are used in the PML domain, and therefore complex wavenumbers are obtained which describe rapidly absorbed leaky waves [37, 49, 61, 65, 66]. However, in this formulation, the computational domain surrounding the waveguide is necessary. In addition, the sorting procedure of the Eigenvalue solutions is necessary in order to identify the physically meaningful solutions.

The 2.5 D boundary element technique [67] was used to model the surrounding leaky medium. This approach involves the complex non-linear Eigenvalue problem for obtaining the wavenumbers of the damped waveguides. However, the computational time was longer compared to the SAFEM coupled to infinite elements or PML [68].

The simple approximation by dashpot boundary conditions included in SBFEM can lead to sufficiently accurate results for waveguides embedded in the surrounding solid medium [31], [69]. An iterative exact dashpot boundary condition was employed in SBFEM for obtaining the wavenumbers for a waveguide immersed in the perfect fluid [70]; Hayashi *et al*. have extended the SAFE formulation for plates surrounded by the leaky medium [71]. Waveguides interacting with a fluid support distinct quasi-Scholte surface waves which are absent in the case of vacuum. The Scholte wave propagates at the interference between the waveguide and the fluid; it tends to dissipate energy rather slowly.

In this work, the approach of the immersed plate will be adopted to account for the surrounding perfect fluid. The leaky medium combined with material damping is treated as a dissipative environment for the propagating wave.

1.6 Bulk Wave Propagation in Unbounded Medium

The general equation for the time harmonic elastic wave in unbounded isotropic medium reads as [58]:

$$\begin{aligned} \rho\frac{\partial^2 u_x}{\partial t^2} &= \frac{\partial\sigma_{xx}}{\partial x}+\frac{\partial\sigma_{xy}}{\partial y}+\frac{\partial\sigma_{xz}}{\partial z} \\ \rho\frac{\partial^2 u_y}{\partial t^2} &= \frac{\partial\sigma_{yx}}{\partial x}+\frac{\partial\sigma_{yy}}{\partial y}+\frac{\partial\sigma_{yz}}{\partial z} \\ \rho\frac{\partial^2 u_z}{\partial t^2} &= \frac{\partial\sigma_{zx}}{\partial x}+\frac{\partial\sigma_{zy}}{\partial y}+\frac{\partial\sigma_{zz}}{\partial z} \end{aligned} \tag{1}$$

where ρ is the mass density, $\boldsymbol{u} = (u_x \quad u_y \quad u_z)^T$ is the displacement vector and $\boldsymbol{\sigma}$ is the 3×3 stress tensor.

When using vector operator $\nabla = \begin{pmatrix}\frac{\partial}{\partial x} & \frac{\partial}{\partial y} & \frac{\partial}{\partial z}\end{pmatrix}^T$ and notation $i, j, k \in \{x, y, z\}$, (Eq. 1) reads as:

$$\nabla\boldsymbol{\sigma} = \rho\frac{\partial^2\boldsymbol{u}}{\partial t^2} \text{ or } \sigma_{ij,j} = \rho\frac{\partial^2 u_i}{\partial t^2}. \tag{2}$$

Due to the symmetry of $\boldsymbol{\sigma}$, the constitutive Hook's law for the isotropic material reads as [58]:

$$\sigma_{ij} = \lambda\delta_{ij}\varepsilon_{kk}+2\mu\varepsilon_{ij}, \tag{3}$$

where λ and μ are Lame constants describing material stiffness properties, δ is the Kronecker delta, and $\varepsilon_{i,j} = \frac{1}{2}(\nabla\boldsymbol{u} + (\nabla\boldsymbol{u})^T)$ is the strain. Lame constants are interlinked with Young's modulus E and Poisson's ratio ν as [58]:

$$\lambda = \frac{E\nu}{(1+\nu)(1-2\nu)} \text{ and } \mu = \frac{E}{2(1+\nu)}. \tag{4}$$

The vector form of Navier's governing dynamic equation can be obtained from (Eqs. 1–3) [46]:

$$\rho\ddot{\boldsymbol{u}} = (\lambda+\mu)\nabla(\nabla\boldsymbol{u})+\mu\nabla^2\boldsymbol{u}. \tag{5}$$

The displacement vector $\boldsymbol{u}$ can be decomposed in terms of derivatives of compressional scalar potential $\boldsymbol{\phi}$ and an equivoluminal vector $\boldsymbol{\psi} = (\psi_x \quad \psi_y \quad \psi_z)^T$ [46]:

$$\boldsymbol{u} = \nabla\boldsymbol{\phi} + \nabla\times\boldsymbol{\psi}. \tag{6}$$

Substitution of (Eq. 6) to (Eq. 5) yields two (due to displacement decomposition) Helmholtz differential equations [46]:

$$\frac{\partial^2 \boldsymbol{\phi}}{\partial t^2} = \frac{\lambda + 2\mu}{\rho} \nabla^2 \boldsymbol{\phi} = {c_{phL}}^2 \nabla^2 \boldsymbol{\phi}, \tag{7}$$

$$\nabla^2 \boldsymbol{\psi} = \frac{\mu}{\rho} \frac{\partial^2 \boldsymbol{\psi}}{\partial t^2} = {c_{phS}}^2 \frac{\partial^2 \boldsymbol{\psi}}{\partial t^2}, \tag{8}$$

where c_{phL} and c_{phS} are phase velocities of longitudinal and shear waves, respectively. Their wavenumbers are obtained as $k_{L,S} = \frac{\omega}{c_{phL,S}}$, where ω is an angular frequency of the wave.

The solutions to (Eq. 7) and (Eq. 8) read as [46]:

$$\boldsymbol{\phi} = \boldsymbol{\Phi} e^{i(\pm k_{L_x} x \pm k_{L_y} y \pm k_{L_z} z - \omega t)} \text{ and } \boldsymbol{\psi} = \boldsymbol{\Psi} e^{i(\pm k_{S_x} x \pm k_{S_y} y \pm k_{S_z} z - \omega t)}, \tag{9}$$

where $\boldsymbol{\Phi}$ and $\boldsymbol{\Psi}$ are the amplitudes of longitudinal and shear waves, respectively, k_{L_x}, k_{L_y}, k_{L_z}, k_{S_x}, k_{S_y} and k_{S_z} are projections of the wavenumbers of longitudinal and shear waves on the $0X$, $0Y$ and $0Z$ axes, respectively.

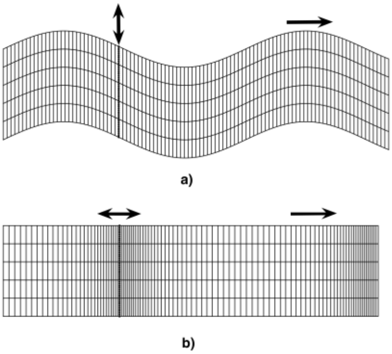

Fig. 1.2. A representation of (a) shear and (b) longitudinal bulk waves.

The oscillations of the shear (dilatational, or S) wave occur perpendicularly to the direction of the propagation of the wave. The oscillations of the longitudinal (pressure, or P) wave take place in the same direction as the direction of propagation of the wave (Fig. 1.2). These are the two main types of waves in the elastic medium.

1.7 Guided Wave Propagation in Bounded Medium

When a harmonic bulk wave propagates in bounded media, reflections and refractions occur from the boundaries. Let us consider the boundary between the isotropic medium and vacuum. In this case, no energy losses due to the radiation of bulk waves occur (i.e., there is no refraction), since incident bulk waves at the solid-vacuum interface are fully reflected, and also another wave type is generated as $P \rightarrow S$ or $S \rightarrow P$. Fig. 1.3 shows incident longitudinal P^I (Fig. 1.3 (a)) and shear S^I (Fig. 1.3 (b)) waves with incidence angles γ and , respectively, in the semi-infinite isotropic medium. Each incident bulk wave yields reflected and converted waves. The total wave potential ($\boldsymbol{\phi}$, $\boldsymbol{\psi}$) is the superposition of incident and reflected waves, which can be presented as [72]:

$$\boldsymbol{\phi}^{P} = \mathbf{\Phi}_{P^I} e^{i(k_L\cos(\theta)y + k_L\sin\theta x - \omega t)} + \mathbf{\Phi}_{P^R} e^{i(-k_L\cos(\theta)y + k_L\sin\theta x - \omega t)}$$
$$\boldsymbol{\psi}^{P} = \mathbf{\Psi}_{P^R} e^{i(-k_S\cos(\gamma)y + k_S\sin(\gamma)x - \omega t)}, \tag{10}$$

where $\mathbf{\Phi}_{P^R}$, $\mathbf{\Psi}_{P^R}$ are the amplitudes of the reflected longitudinal and shear waves generated by the incident longitudinal wave with amplitude $\mathbf{\Phi}_{P^I}$.

Similarly, the total wave potential for the shear waves can be written as [72]:

$$\boldsymbol{\phi}^{S} = \mathbf{\Phi}_{S^R} e^{i(-k_L\cos(\theta)y + k_L\sin\theta x - \omega t)}$$
$$\boldsymbol{\psi}^{S} = \mathbf{\Psi}_{S^I} e^{i(k_S\cos(\gamma)y + k_S\sin(\gamma)x - \omega t)} + \mathbf{\Psi}_{S^R} e^{i(-k_S\cos(\gamma)y + k_S\sin(\gamma)x - \omega t)}, \tag{11}$$

where $\mathbf{\Phi}_{S^R}$, $\mathbf{\Psi}_{S^R}$ are the amplitudes of the reflected longitudinal and shear waves generated by the incident shear wave with amplitude $\mathbf{\Psi}_{S^I}$.

The wavenumbers of the longitudinal and shear waves are linked by Snell's law as [72]:

$$\frac{\sin(\theta)}{\sin(\gamma)} = \frac{k_S}{k_L} = \frac{c_{phL}}{c_{phS}}. \tag{12}$$

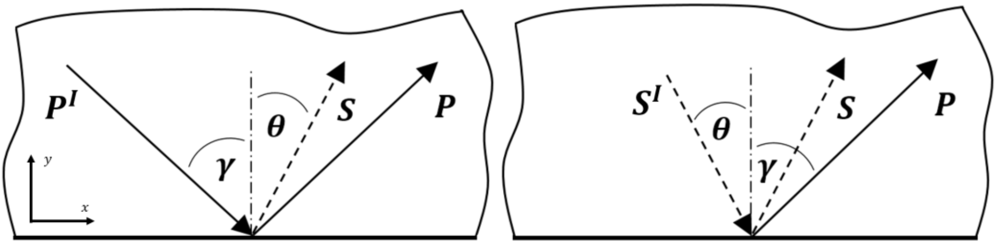

a) b)

Fig. 1.3. Incidence of (a) longitudinal and (b) shear waves at the boundary of the semi-infinite isotropic medium.

In the homogenous elastic layer, harmonic waves propagate due to the back and forth reflections between the two planar boundary surfaces. The steady state of the harmonic Lamb wave as a guided wave finally appears as a result of the superposition (constructive interference) of the bulk waves traveling obliquely to the waveguide direction and repeatedly reflected and type-converted at the two boundaries (see Fig. 1.4). Lamb waves are referred to as the *elastic waves* where the oscillations take place over all the volume of the plate, and the direction displacements vector of each point contains the direction of the wave propagation and the plate normal. Wavenumber k of the Lamb wave is related to the bulk waves wavenumbers k_L and k_S as [72]:

$$(k_L\sin(\theta))^2 + k^2 = \left(\frac{\omega}{c_{phL}}\right)^2$$
$$(k_S\sin(\gamma))^2 + k^2 = \left(\frac{\omega}{c_{phS}}\right)^2, \tag{13}$$

where θ and γ are incident angles of longitudinal and shear waves that make up the Lamb wave.

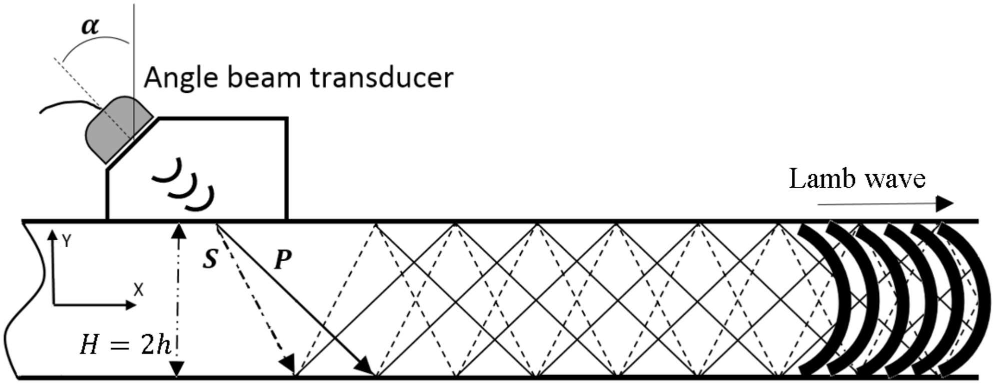

Fig. 1.4. The built-up Lamb wave in the plate.

The dispersion relations (ω, k) of Lamb waves can be obtained from the Rayleigh-Lamb equation as [26]:

$$\frac{\tan\left(\frac{q}{2}\right)}{\tan\left(\frac{p}{2}\right)} = -\frac{4k^2pq}{(q^2-k^2)^2} \tag{14}$$

$$\frac{\tan\left(\frac{q}{2}\right)}{\tan\left(\frac{p}{2}\right)} = -\frac{\left(q^2-k^2\right)^2}{4k^2pq}, \tag{15}$$

where $p^2 = \left(\frac{\omega h}{c_{phL}}\right)^2 - k^2$, $q^2 = \left(\frac{\omega h}{c_{phS}}\right)^2 - k^2$, $h = \frac{H}{2}$, and H is the height of the plate.

From (Eq. 14) and (Eq. 14), it follows that only the height of the plate and the phase velocities of the bulk waves determine the properties of the Lamb wave at given wave frequency ω. The two equations provide the dispersion relations for symmetrical and asymmetrical wave modes, respectively.

As calculated, wavenumber k represents a stationary harmonic wave, it provides the modal solution for the dynamic equation in the finite elastic isotropic medium. With the increasing ω (Eq. 14) and (Eq. 15) provide more and more modal wavenumbers. The two fundamental wave modes exist over the whole frequency range, beginning from very low frequency values. As the frequency increases, new higher order modal wavenumbers appear at ‘cut-on’ frequencies.

For symmetrical wavenumbers, the corresponding displacement field reads as [58]:

$$\boldsymbol{u}_{sym=}\begin{pmatrix} u_x \\ u_y \end{pmatrix} = \begin{pmatrix} (\Phi_1 ik\, cos(py) + \Psi_1 q\, sin(qy))e^{i(kx-\omega t)} \\ -(\Phi_1 sin(py) + \Psi_1 ik\, sin(qy))e^{i(kx-\omega t)} \end{pmatrix}. \tag{16}$$

The unknown Φ_1, Ψ_1 amplitudes can be obtained after applying traction-free conditions at boundaries $y = h$ and $y = -h$ [58]:

$$\begin{cases} \mu(-2ikp\Phi_1 \sin(py) + (k^2 - q^2)\Psi_1 \sin(qy)) = 0 \\ -\lambda(k^2 + q^2)\Phi_1 \cos(py) - 2\mu(p^2\Phi_1 \cos(py) + ikq\Psi_1 \cos(qy)) = 0 \end{cases} \quad (17)$$

For asymmetrical wavenumbers, the corresponding displacement field reads as [58]:

$$\boldsymbol{u}_{asym=} \begin{pmatrix} u_x \\ u_y \end{pmatrix} = \begin{pmatrix} (\Phi_2 ik\, sin(py) - \Psi_2 q\, sin(qy))e^{i(kx-\omega t)} \\ (\Phi_2 p\, cos(py) - \Psi_2 ik\, sin(qy))e^{i(kx-\omega t)} \end{pmatrix}. \quad (18)$$

The unknown Φ_2, Ψ_2 amplitudes can be obtained from the equation system [58]:

$$\begin{cases} \mu(2ikp\Phi_2 \cos(py) + (k^2 - q^2)\Psi_2 \cos(qy)) = 0 \\ -\lambda(k^2 + q^2)\Phi_2 \sin(py) - 2\mu(p^2\Phi_2 \sin(py) - ik\mathrm{q}\Psi_1 \sin(qy)) = 0 \end{cases} \quad (19)$$

(Fig. 1.5) represents the two fundamental wave modes. As from (Eq. 16), the symmetrical mode in (Fig. 1.5 (a)) contains both components of longitudinal and shear waves. However, because of the dominating longitudinal wave component, the symmetrical mode is closer to the longitudinal wave. Similarly, the asymmetrical wave mode in (Fig. 1.5 (b)) is closer to the shear wave. However, at higher frequencies with the increasing wavenumbers, the curvature of the mode shapes increases, and Lamb waves obtain complex vibrational patterns over the height of the plate.

It can be shown analytically that (Eq. 14) and (Eq. 15) may be reduced to the Rayleigh wave dispersion equation in a homogenous half space when the frequency approaches infinity [73]. As a result, phase velocities of symmetrical and asymmetrical modes converge to each other in the high frequency range.

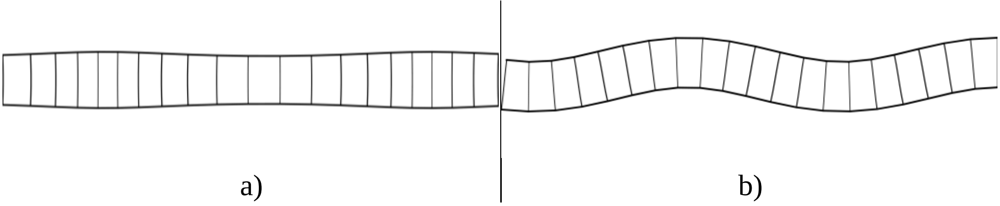

a) b)

Fig. 1.5. Representation of the fundamental symmetrical (a) and asymmetrical (b) Lamb modes.

In 3D bodies, the number of fundamental modes increases due to the additional boundaries. For example, three groups of modes exist in the rectangular rod (Fig. 1.6). The flexural (F) modes are characterized by the prevailing bending deformations in the rod, (see Fig. 1.6 (a)). In the longitudinal (L) modes, the particles predominantly oscillate along the length of the rod, however, simultaneously, small breathing-like transverse displacements are visible in (Fig. 1.6 (b)). The torsional (T) mode describes the twisting about the longitudinal axis oscillations of the rod, (see Fig. 1.6 (c)).

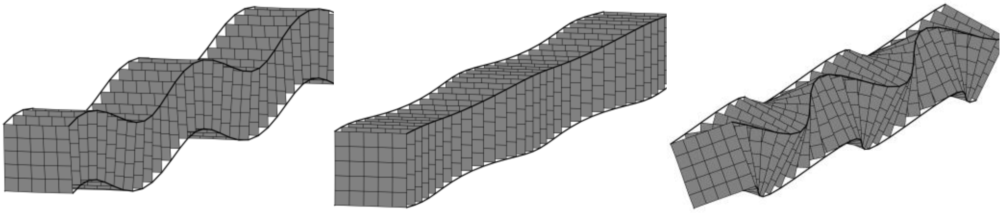
a) b) c)

Fig. 1.6. Fundamental flexural (a), longitudinal (b) and torsional (c) modes in a rectangular rod.

At particular incidence angles of bulk waves, the guided surface Rayleigh and Love waves can be excited when the waveguide has a boundary with vacuum. The surface waves combine both longitudinal and transverse motions where the particles of the waveguide move in elliptic orbital paths. Both types of waves have dominant S-wave components in the plane normal to the surface and the propagation direction (in the Rayleigh surface wave case) or in the plane tangent to the surface and the normal to the propagation direction (in the Love surface wave case).

In those cases when the waveguide is in contact with a solid or a fluid with significantly different wave propagation characteristics, the Stoneley and Scholte waves similar to leaky Rayleigh waves may exist. Their mechanical energy content is concentrated over a few wavelengths around the interface in each medium, depending on the material properties of the medium at the interface. However, the major part of the wave energy is on the liquid side, whereas the lesser part is on the solid side [74]. The velocity of the Scholte wave is smaller, but it is close to the acoustic bulk wave velocity in a fluid [75].

1.8 Wave Attenuation

A more general and realistic propagation scenario includes attenuation, which describes the decrease of the wave amplitude. The decay of the elastic wave may be caused by geometrical damping, scattering, material damping, fluid viscosity or by energy leakage into an infinite medium surrounding the waveguide [39], [76], [77]. Besides that thermo-effect, it also influences wave attenuation [36]. For simplicity, damping can be considered as internal if caused by materials structure and characteristics, and external if caused by boundary effects.

For example, in an unbound isotropic elastic medium in cases of the point source, the amplitude decay occurs when affected by only geometrical damping, due to which, the spherical wave front varies inversely with the square of the distance from the source. This so-called radiational (or geometrical) damping is caused by the spreading of the wave energy and mainly depends on the type of excitation and body geometry. For example, the amplitude will decrease much faster in cases of the spherical pattern point source when compared to two-dimensional energy spread to the infinity in a circular pattern from a point source. Due to the finite geometries of ultrasonic sources, true bulk waves whose wave fronts are parallel planes cannot be excited.

Material damping or material absorption is responsible for wave energy conversion to heat due to the internal friction forces in the material. As a consequence, wave energy is dissipated due to frictional losses. Viscoelasticity, while simulating material damping in solids, is usually modeled by using hysteretic or Kelvin-Voigt approaches and introducing Young's complex valued modulus.

Scattering is caused by inhomogeneities and variations in the material structure. Traveling ultrasonic waves may encounter material variations which cause the wave to scatter – to refract, reflect or mode convert. Material variations can be inclusions, physical disbands, geometrical discontinuities when composites are concerned, etc. [58]. Scattering is mostly the reflection wave in directions other than its original direction of propagation; as a result, part of the energy from the initial wave is sent randomly into different directions within the material.

Fluid viscosity must be taken into account when the wave in the fluid domain is concerned. A hypothetical isotropic solid can represent the fluid accommodating viscosity [78].

Attenuation due to energy leakage occurs in inhomogenous layered media and affects both elastic and viscoelastic materials. As the material parameters in the layers significantly differ, so do the phase velocities of bulk waves. Then, the energy leakage from the layer with the greater phase velocity to the layer with the smaller one occurs [79], [63]. In the case of vacuum, all the bulk waves fully reflect and mode convert from the boundary (Fig. 1.3), but at the interface with a different medium, the part of the bulk wave is refracted, another part is mode-converted, and the remaining part is reflected. Let us consider a medium that supports the higher phase velocity of the longitudinal bulk wave when compared with that of the second medium that has a boundary with the first one. Let us consider only the longitudinal incident wave in the first medium, which at the interface between the media reflects, refracts and mode converts (Fig. 1.7). Snell law interlinks incidence θ_1, mode conversion θ_3 and refraction θ_4, θ_5 angles with phase velocities of incident P^I, mode converted shear S^R and refracted P^F, S^F waves as

$$\frac{\sin(\theta_1)}{c_{phP^I}} = \frac{\sin(\theta_3)}{c_{phS^R}} = \frac{\sin(\theta_4)}{c_{phP^F}} = \frac{\sin(\theta_5)}{c_{phS^F}}. \tag{20}$$

If the first medium is a waveguide and the second medium is the perfect fluid, the waveguide under harmonic excitation would dissipate energy only via refracted P^F longitudinal modes since fluids do not support shear waves.

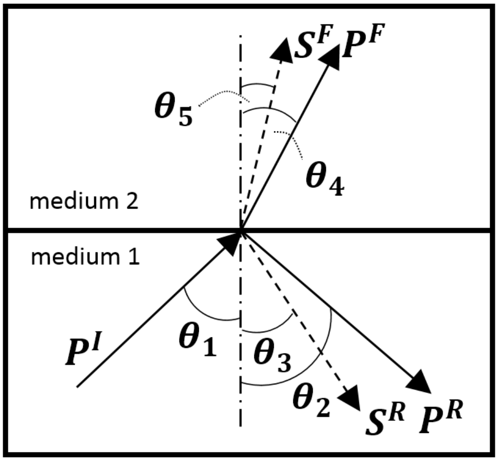

Fig. 1.7. Leaky bulk waves.

Listed attenuation mechanisms are the main sources of energy dissipation of ultrasonic guided waves. However, further in our study, only material damping and energy leakage due to the surrounding perfect fluid will be explicitly modeled.

1.9 Material Rheological Models

Rheological models are used for the representation of the viscoelastic nature of solid materials. Viscoelasticity is the property of materials which exhibit both viscous and elastic properties during the deformation. Only linear viscoelastic models which are defined in terms of stresses-strains and their first order time derivatives will be discussed in the present thesis. Moreover, the idealized models take into account the elasticity and the damping of the material separately.

Simple rheological models are provided in (Fig. 1.8). Springs with parameter $E\ [Pa]$ represent elasticity, whereas dashpots with $\zeta\ [Pa \cdot s]$ represent viscosity. For small strains, the stress in the Hook model (Fig. 1.8 (a)) is proportional to the instantaneous strain and is independent from the strain rate as $\sigma = E\varepsilon$. In the Newtonian model (Fig. 1.8 (b)) which represents a viscous fluid, according to the theory of hydrodynamics [80], stress is proportional to the instantaneous strain rate and is independent from the strain value as $\sigma = \zeta\dot{\varepsilon}$. Viscoelastic damping combines the strain rate-dependent energy dissipation of viscous fluids with the strain-dependent energy storing capacity of elastic solids. The Maxwell and Kelvin-Voigt models (Fig. 1.8 (c), (d)) are commonly used for the simulation of linear viscoelasticity. The unidimensional Maxwell model consists of a spring and a dashpot connected in sequence, where the stress-strain is presented via differential equation $\frac{\dot{\sigma}}{E} + \frac{\sigma}{\zeta} = \dot{\varepsilon}$. The Kelvin-Voigt model consists of a spring and a dashpot connected in parallel, where the stress-strain relation reads as $\sigma = \zeta\dot{\varepsilon} + E\varepsilon$. Generally, different combinations of springs and dashpots enable to simulate a large variety of features of viscoelastic materials.

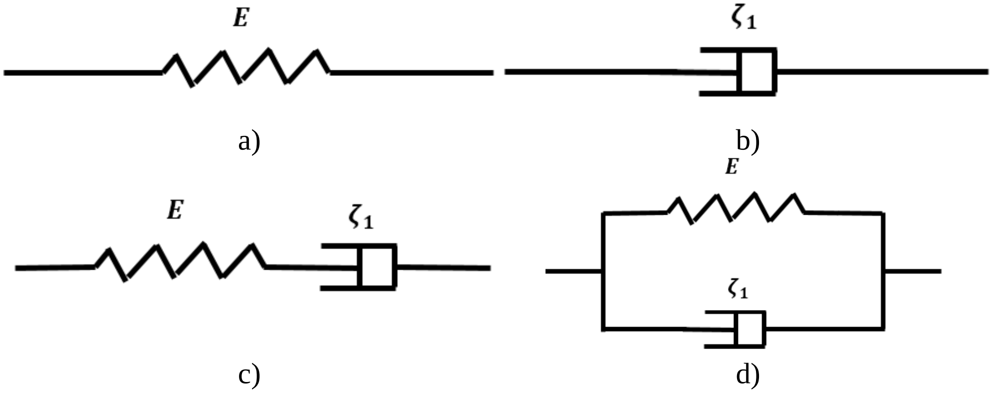

a) b)

c) d)

Fig. 1.8. Rheological models: (a) Hook, (b) Newton, (c) Maxwell and (d) Kelvin-Voigt.

The wave attenuation properties of rheological models can be defined in terms of complex valued Young's modulus $\hat{E}$, the real and imaginary parts of which enable to represent the average stored and dissipated energies.

Complex Young's modulus can be considered by assuming harmonic displacements in the material. Under harmonic stress $\sigma = \sigma_0 e^{i\omega t}$, the strain varies with the same frequency but generally with a different phase $\varepsilon = \varepsilon_0 e^{i(\omega t+\varphi)}$. Therefore, complex Young's modulus under assumption of harmonic vibrations reads as [81]:

$$\hat{E}(\omega) = \frac{\sigma}{\varepsilon} = \frac{\sigma_0}{\varepsilon_0} e^{i\varphi} = Re\big(\hat{E}(\omega)\big) + i \cdot Im(\hat{E}(\omega)), \qquad (21)$$

where $Re(\hat{E})$ is the storage modulus which determines the stiffness of the relevant material, and $Im(\hat{E})$ is the loss modulus which defines the energy dissipation of the material.

Such a model of viscoelasticity resulting in the complex structural stiffness matrix is widely recognized as the most suitable approach towards introducing material damping [82]. In the case of Hook's model $Re\big(\hat{E}\big) = E$ and $Im\big(\hat{E}\big) = 0$, Newton's model $Re\big(\hat{E}\big) = 0$ and $Im\big(\hat{E}\big) = \zeta\omega$, Maxwell's model $Re\big(\hat{E}\big) = \frac{E\omega^2\zeta^2}{E^2+\omega^2\zeta^2}$ and $Im\big(\hat{E}\big) = \frac{E^2\omega\zeta}{E^2+\omega^2\zeta^2}$, Kelvin-Voigt's model $Re\big(\hat{E}\big) =$ E and $Im\big(\hat{E}\big)= \zeta\omega$ [81].

Quality factor Q is used to evaluate the stored energy and the rate of dissipation of energy in viscoelastic materials as [81]:

$$Q = \frac{4\pi\bar{V}}{\Delta V}, \qquad (22)$$

where $\bar{V}$ is the average stored energy, $\Delta V$is the dissipated energy per cycle.

If viscoelasticity is modeled via the rheological model consisting of spring-dashpot networks, the quality factor reads as [81]:

$$Q = \frac{Re(\hat{E})}{Im(\hat{E})}. \qquad (23)$$

The attenuation of the rheological model can be described as Q^{-1}. The attenuation for Hook's model is $Q^{-1} = 0$, as it behaves as a perfectly elastic material and is not defined for Newton's model because it represents the perfect viscous material. In Maxwell's model, the formula reads as $Q^{-1} = \frac{E}{\omega\zeta}$ whereas for Kelvin-Voigt's model, it is $Q^{-1} = \frac{\omega\zeta}{E}$ (Fig. 1.9) [81].

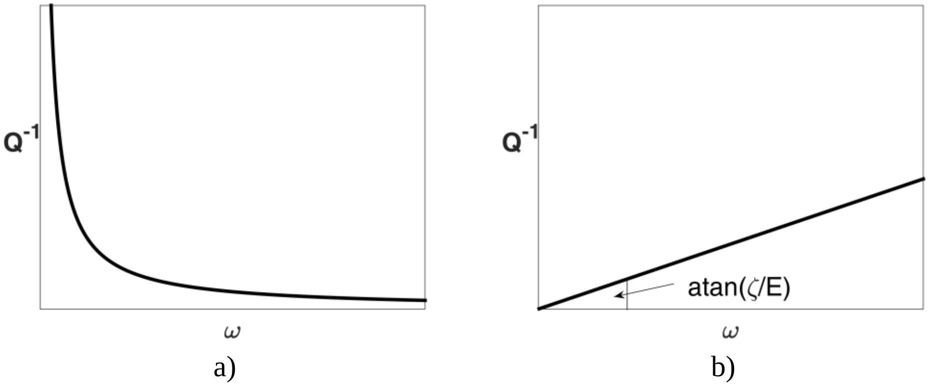

a)   b)

Fig. 1.9. (a) Attenuation Q^{-1} of (a) Maxwell's and (b) Kelvin-Voigt's models.

As seen in (Fig. 1.9), Maxwell's model behaves like a viscous fluid in the low frequency range and resembles an elastic material at high frequencies. Kelvin-Voigt's model exhibits just the opposite behavior. Maxwell's model predicts that stress decays exponentially with time, which is accurate for most polymers or soft solids, such as numerous metals at temperatures close to the melting point [59]. The attenuation of Kelvin-Voigt's model does not decrease with frequency, therefore it is suitable for the representation of material damping in ultrasound propagation.

In structural analysis, the distribution of Kelvin-Voigt's rheological model elements over the whole structure is conveniently represented by Rayleigh damping model which has a conducive mathematical form.

1.10 Rayleigh Damping Model for Vibrating Structures

Rayleigh damping enables to take into account the general internal losses in vibrating systems. Even though Rayleigh damping has no unambiguous physical interpretation, it is widely applied due to its convenient mathematical formulation. In case of Rayleigh damping, the structural dynamic equation is supplemented by the damping term as:

$$\boldsymbol{M}\ddot{\boldsymbol{U}} + \boldsymbol{C}\dot{\boldsymbol{U}} + \boldsymbol{K}\boldsymbol{U} = \boldsymbol{0} \tag{24}$$

where $\boldsymbol{C} = a\boldsymbol{M} + b\boldsymbol{K}$ is the damping matrix expressed as a weighted sum of the mass and stiffness matrices.

Coefficients of Rayleigh damping are interrelated in terms of damping ratio ξ_j and modal angular frequency ω_j of j-th vibration mode of the structure as:

$$\xi_j = \frac{a}{2\omega_j} + \frac{b\omega_j}{2}, \tag{25}$$

where coefficients a and b can be determined by using the approach of the single control frequency or two control frequencies.

In the first approach, the control frequency ω_m is chosen as the Eigenfrequency of the dominant fundamental mode whereas ξ_m is regarded as a given value. In this case, the Rayleigh coefficients are obtained as

$$a = \xi_m \cdot \omega_m, \; b = \frac{\xi_m}{\omega_m}\,. \tag{26}$$

Damping ratio ξ_j is minimum at frequency ω_m, while over other frequency ranges, the damping ratio is higher (see Fig. 1.10 (a)).

In the case of two control frequencies ω_m and ω_n (Fig. 1.10 (b)), it is assumed that the damping ratio has the same value at the m-th and n-th modes $\xi_k = \xi_m = \xi_n$; therefore, the damping coefficients are obtained as [83]:

$$a = \xi_k \cdot \frac{2\omega_m \cdot \omega_n}{\omega_m + \omega_n}\omega_m, \; b = \xi_k \frac{2}{\omega_m + \omega_n}. \tag{27}$$

The selection of m-th and n-th modes at which the damping ratio is prescribed as ξ_k, which the most commonly leads to similar damping ratio values over all the frequency range in between the m-th and n-th modal frequencies. Therefore, these frequencies shall be selected in order to encompass all the frequency components which contribute significantly to the overall vibrational response [84].

The major limitation of the mass and stiffness proportional damping approximation is its inability to represent an arbitrary experimentally observed variation of the damping ratios against the vibration frequency in complex situations [85].

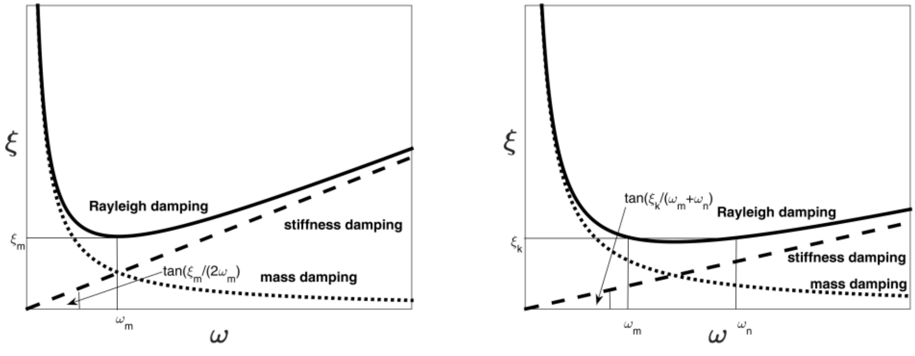

a) b)

Fig. 1.10. (a) Rayleigh damping determined at a single mode frequency; (b) Rayleigh damping determined at two modal frequencies.

Rayleigh coefficient a (*mass damping*) may be physically interpreted as the external viscous damping component because of the vibration velocities of the nodes. Mass damping has a resemblance with Maxwell’s model in terms of the inverse proportionality of the damping ratio against frequency (see Fig. 1.10). Rayleigh coefficient b may be physically interpreted as the internal viscous damping property which is proportional to the strain rate. It is inclined to damp the higher frequency components. For high frequencies $(> 20\,kHz)$, as it is usually in ultrasound applications, mass damping can be considered as negligible [60].

1.11 Coefficients of Rayleigh Damping for Viscoelastic Material

As previously discussed, the rheological model of linear viscoelasticity is formulated by using complex Young's modulus. Rayleigh damping can also be specified for taking into account the material viscoelasticity. What concerns the practical value for the analysis, the characterization of the material properties on the basis of wave propagation features should be mentioned.

The determination of a and b coefficient can be linked with complex Young's modulus. The damping loss factor η is the ratio of the dissipated energy versus the input energy and is defined as [83]:

$$\eta = \frac{1}{Q} = \frac{Im(\hat{E})}{Re(\hat{E})} = 2\xi = \frac{a}{2\omega} + \frac{b\omega}{2}, \tag{28}$$

(Eq. 28) provides the relations between complex Young's modulus and coefficients of Rayleigh damping. In case of high frequencies, where $\left(\frac{a}{2\omega} \to 0\right)$, only b coefficient is retained in the model and can be obtained as:

$$b \approx \frac{Im(\hat{E})}{\omega Re(\hat{E})}. \tag{29}$$

As it is evident, the b coefficient depends on complex Young's modulus $\hat{E}$ and angular frequency ω. The $\hat{E}$ value can by acquired from the wave solution. At first, let us consider 1D elastic wave traveling along the $0X$ axis in a viscoelastic material [85] as:

$$\hat{c}\frac{\partial^2 u}{\partial x^2} = \frac{\partial^2 u}{\partial t^2}, \tag{30}$$

where $\hat{c}(\omega)$ is the complex valued phase velocity. The real part of the complex wavenumber is related with the angular frequency via the phase velocity: $Re(k) = Re\left(\frac{\omega}{\hat{c}}\right) = \frac{\omega}{c_{ph}}$. The solution to (Eq. 30) at ω reads as:

$$u(x,t) = Ue^{-Im(k)}e^{i(Re(k)x-\omega t)} = Ue^{\alpha(\omega)}e^{i\left(\frac{\omega}{c_{ph}}x-\omega t\right)}, \tag{31}$$

where $\alpha(\omega) = -Im(k) = Im\left(\frac{\omega}{\hat{c}}\right)$ is the attenuation coefficient which describes the exponential decay of the wave along the $0X$ axis.

In the general case, the solution of the wave in an infinite viscoelastic solid reads as [86]:

$$\boldsymbol{u}_{L,S} = \boldsymbol{U}_{L,S}e^{-\boldsymbol{k}_{ImS,L}}e^{i(\boldsymbol{k}_{ReS,L}x-\omega t)}, \tag{32}$$

where $\boldsymbol{U}_{L,S}$ corresponds to the amplitude of the longitudinal (L) and shear (S) wave, respectively, $\boldsymbol{k} = \boldsymbol{k}_{Re} + i\cdot\boldsymbol{k}_{Im} = Re(k)\boldsymbol{n} - i\cdot Im(k)\boldsymbol{b}$ is the complex vector of the wavenumber where unit vector $\boldsymbol{n}$ describes the direction of propagation, and unit vector $\boldsymbol{b}$ describes the direction in which the wave exponentially decays [82].

Then relations between the wavenumber and the angular frequency can be written as [82]:

$$\boldsymbol{k}_{L,S}\cdot\boldsymbol{k}_{L,S} = Re\left(k_{L,S}\right)^2 - 2i\cdot Re(k_{L,S})Im(k_{L,S})\boldsymbol{n}\cdot\boldsymbol{b} - Im\left(k_{L,S}\right)^2 = \frac{\omega^2}{\hat{c}_{phL,S}{}^2}, \quad (33)$$

where $\hat{c}_{phL,S}$ is the complex valued velocity of the wave.

When the medium is elastic, the right-hand side of (Eq. 33) is a real number. As a result, the term $Im\left(k_{L,S}\right) = 0$ (no decay), or $\boldsymbol{n}\cdot\boldsymbol{b} = 0$, i.e., the decay direction must be the normal to the direction of propagation. When the wavenumber is a real number, (Eq. 32) corresponds to the plane wave. When the medium is elastic, the propagation direction and the phase propagation direction are always coincident [82].

When the medium is viscoelastic, the right-hand side of (Eq. 33) is a complex number. The material acoustic properties of a viscoelastic medium can be specified in terms of longitudinal and shear waves. However, for the particular material, an infinite number of bulk waves can propagate depending on the angle between $\boldsymbol{n}$ and $\boldsymbol{b}$. For practical reasons, material characterization is measured by setting $\boldsymbol{n}$ and $\boldsymbol{b}$ in parallel, i.e., when the wave decays only along the direction of propagation. This definition of orientation between $\boldsymbol{n}$ and $\boldsymbol{b}$ also includes the case of elastic materials, for which the acoustic properties are defined by considering the longitudinal and shear plane waves [82].

The complex bulk wave velocities read as [86]:

$$\hat{c}_{phL,S} = \frac{\omega}{k_{Re}+i\cdot k_{Im}} = \frac{c_{phL,S}}{1+i\cdot\frac{k_{Im}}{k_{Re}}} = \frac{c_{phL,S}}{1+i\cdot\alpha(\omega)_{L,S}}. \quad (34)$$

where c_{ph} is the phase velocity and $\alpha(\omega)$ is the angular frequency-dependent attenuation coefficient that can be experimentally measured [87], [88], [89].

As mentioned, the viscoelastic material properties can be presented in terms of complex bulk velocities [33], [90], [61]. Since the wavelength equals $\lambda = \frac{1}{k_{Re}}$, the attenuation coefficient $\frac{\alpha(\omega)}{2\pi}$ in (Eq. 34) uses the measure unit of Nepers per wavelength $\left[\frac{Np}{wl}\right]$. An alternative unit for attenuation can be acquired from (Eq. 31). As the attenuation coefficient is in the exponent term $e^{-\alpha(\omega)x}$, attenuation in units of decibels $[dB]$ can be obtained as

$$20log_{10}\left(e^{-\alpha(\omega)x}\right) = -\alpha(\omega)x20log_{10}(e) \approx -8.686\alpha(\omega)x \quad (35)$$

Attenuation in alternative units $\left[\frac{dB}{m}\right]$ is simply calculated as $-8.686\alpha(\omega)$.

The properties of a viscoelastic isotropic material, the complex Young's modulus and the complex Poisson's ratio can be obtained from complex velocities $\hat{c}_{phL}$ and $\hat{c}_{phS}$ as [43]:

$$\hat{E} = \rho \hat{c}_{phS}{}^2 \left(\frac{3\hat{c}_{phL}{}^2 - 4\hat{c}_{phS}{}^2}{\hat{c}_{phL}{}^2 - \hat{c}_{phS}{}^2} \right) \text{ and } \hat{\nu} = \left(\frac{\hat{c}_{phL}{}^2 - 2\hat{c}_{phS}{}^2}{\hat{c}_{phL}{}^2 - \hat{c}_{phS}{}^2} \right). \tag{36}$$

Finally, the approximate value of the b coefficient that accounts for linear viscoelasticity in material under harmonic excitation can be found from (Eq. 29).

It has been demonstrated [91] that Rayleigh damping, retaining both mass and stiffness damping, can be approximated by the analytical generalized three element Maxwell's model obtained by adding a dashpot in parallel to the classical Maxwell's cell (see Fig. 1.11 (a)). For small to moderate damping ($\xi < 0.25$), the attenuation of the generalized Maxwell's model and the damping ratio are linked as [91]:

$$\eta = \frac{1}{Q} \approx 2\xi. \tag{37}$$

The attenuation of the generalized Maxwell's model is obtained as a sum of two terms, one of which is proportional to the frequency whereas the other is inversely proportional to the frequency [91]:

$$\frac{1}{Q} = \frac{1}{\omega} \frac{E(\zeta_1 + \zeta_2)}{\zeta_1{}^2} + \omega \frac{\zeta_2}{E}. \tag{38}$$

It can be noted that, for low damping ratio values, the attenuation curve (Fig. 1.10) is similar to that of the resulting attenuation curve for the generalized Maxwell's model (Fig. 1.11 (b)).

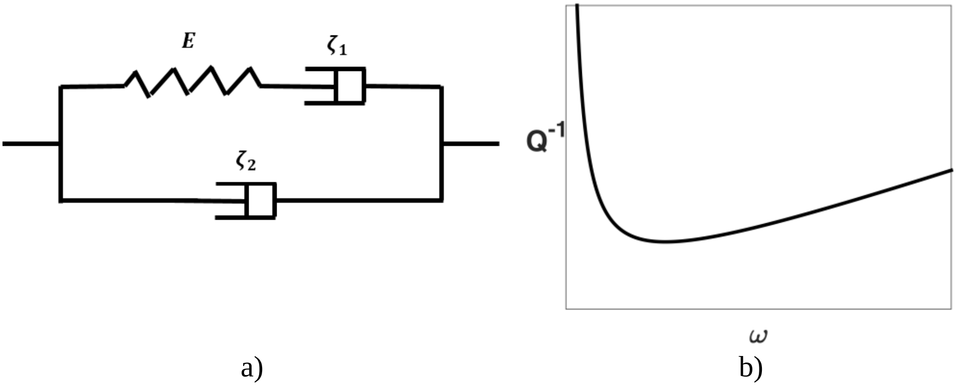

a) b)

Fig. 1.11. (a) Generalized Maxwell's model; (b) Attenuation of generalized Maxwell's model.

The corresponding Rayleigh damping model coefficients can be easily obtained from (Eq. 38) as [91]:

$$a = \frac{E(\zeta_1 + \zeta_2)}{\zeta_1{}^2} \text{ and } b = \frac{\zeta_2}{E}. \tag{39}$$

The obtained estimates of parameters allow easier adjustment of the models to the experimental measurement results. It is of interest to note that when only mass damping is considered ($b = 0$), Rayleigh damping consisting of only term aM is still linked with the stiffness matrix via a, which depends on Young's modulus (Eq. 39).

1.12 Concluding Remarks

Guided waves have a broad field of application in NDT, mainly in the inspection of elongated structures, flaws detection and material parameters determination.

Extractable analytical solutions for guided waves exist for simple geometry waveguides only under certain simplifying assumptions, one of which is the lossless material of the waveguide.

3D FE methods offer a solution for wave propagation in almost any reasonably described environments, however, they only do this at high computational costs. The assumption that the waveguide is homogenous in at least one direction allows using semi analytical methods, for example, SAFEM, which reduce the computational resources. Moreover, semi-analytical methods coupled with other techniques, for example, the 2.5D boundary element technique, enable users to simulate dissipative environments and non-reflecting boundary conditions. These methods also enable to reduce the computational resources even more compared to the conventional FEM models.

The presented literature review revealed that wave propagation in dissipative environments lacks an unambiguous attenuation mechanism due to the complexity of the dissipation phenomenon. A large variety of approximations in accordance to the physical nature of the considered problem are applied. There is no general rule of choosing the energy dissipation model, therefore, the formulation of wave solutions is not straightforward.

The main sources of wave attenuation in homogenous materials is absorption and energy leakage to the surroundings. Leaky waves are not considered when the traction boundary condition for the waveguide is set to be free. Idealized rheological models account for the material damping in the waveguide.

From the theory of plane wave propagation in a homogenous isotropic elastic body, it was shown that only two types of bulk waves propagate. The superposition of these bulk waves results in a complex harmonic displacement field that could be used for practical applications. The measured phase velocities and the attenuation of bulk waves in real materials can help to determine the attenuation parameters simulated by the rheological model. Yet, compromises are inevitable when choosing rheological models for damped materials since viscoelasticity generally may depend on the frequency in an arbitrary way.

Rayleigh damping was chosen to simulate material damping since it is employed with ease and provides more capabilities for material dissipation behavior when compared to constitutive linear viscoelastic models such as Maxwell’s or Kelvin-Voigt’s. Moreover, to the best of the author’s knowledge, the SAFEM has never been applied directly with Rayleigh damping before.

As material damping and leaky waves are the main sources for attenuation, both of these mechanisms will be coupled and applied in SAFEM throughout the remainder of this study.

2 Safe Formulation for Elastic Waves in Undamped Waveguide

2.1 Governing Equation

The detailed mathematical framework of SAFE is presented in [59], [58], [92]. Let us consider a 3D waveguide which is uniform and infinite in the $0Z$ direction with a stress-free surface.

The vectors of displacement $\boldsymbol{u}$, Voigt's stresses $\boldsymbol{\sigma}$ and strains $\boldsymbol{\varepsilon}$ at each point of the cross-section are presented as:

$\boldsymbol{u} = (u_x \quad u_y \quad u_z)^T, \boldsymbol{\sigma} = (\sigma_x \quad \sigma_y \quad \sigma_z \quad \sigma_{xy} \quad \sigma_{xz} \quad \sigma_{yz})^T$ and

$\boldsymbol{\varepsilon} = (\varepsilon_{xx} \quad \varepsilon_{yy} \quad \varepsilon_{zz} \quad \varepsilon_{xy} \quad \varepsilon_{xz} \quad \varepsilon_{yz})^T$.

The generalized Hook's law is used for determining the 3D volumetric stress-strain relation as [59]:

$$\boldsymbol{\sigma} = \boldsymbol{D}\boldsymbol{\varepsilon}, \tag{40}$$

where $\boldsymbol{D}$ is the stiffness tensor.

The small strain against the displacement relation reads as [59]:

$$\boldsymbol{\varepsilon} = \begin{pmatrix} \varepsilon_{xx} \\ \varepsilon_{yy} \\ \varepsilon_{zz} \\ \varepsilon_{xy} \\ \varepsilon_{xz} \\ \varepsilon_{yz} \end{pmatrix} = \begin{pmatrix} \frac{\partial u_x}{\partial x} \\ \frac{\partial u_y}{\partial y} \\ \frac{\partial u_z}{\partial z} \\ \frac{\partial u_x}{\partial y} + \frac{\partial u_y}{\partial x} \\ \frac{\partial u_x}{\partial z} + \frac{\partial u_z}{\partial x} \\ \frac{\partial u_y}{\partial z} + \frac{\partial u_z}{\partial y} \end{pmatrix}. \tag{41}$$

The matrix form reads as [59]:

$$\boldsymbol{\varepsilon} = \left(\boldsymbol{L}_x \frac{\partial}{\partial x} \quad \boldsymbol{L}_y \frac{\partial}{\partial y} \quad \boldsymbol{L}_z \frac{\partial}{\partial z}\right) \boldsymbol{u}, \tag{42}$$

where

$$\boldsymbol{L}_x = \begin{pmatrix} 1 & 0 & 0 \\ 0 & 0 & 0 \\ 0 & 0 & 0 \\ 0 & 0 & 0 \\ 0 & 0 & 1 \\ 0 & 1 & 0 \end{pmatrix}, \boldsymbol{L}_y = \begin{pmatrix} 0 & 0 & 0 \\ 0 & 1 & 0 \\ 0 & 0 & 0 \\ 0 & 0 & 1 \\ 0 & 0 & 0 \\ 1 & 0 & 0 \end{pmatrix}, \boldsymbol{L}_z = \begin{pmatrix} 0 & 0 & 0 \\ 0 & 0 & 0 \\ 0 & 0 & 1 \\ 0 & 1 & 0 \\ 1 & 0 & 0 \\ 0 & 0 & 0 \end{pmatrix}.$$

In the SAFE formulation, the displacement field along the waveguide is assumed as a harmonic propagating wave described analytically by complex exponential function $e^{-i\omega t}$, where $\omega \left[\frac{rad}{s}\right]$, $k \left[\frac{rad}{m}\right]$ are the angular frequency of the wave and the wavenumber, correspondingly. The cross-section of the waveguide (Fig.

2.1) is discretized into 2D first-order serendipity finite elements (FE) [93] and are thus used in the following study.

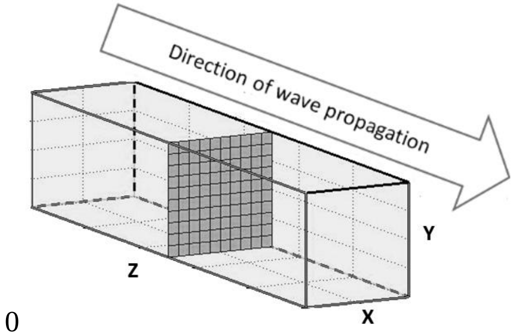

Fig. 2.1. Discretization with FE in the cross-section of the waveguide.

The approximate displacement field within the FE reads as:

$$\boldsymbol{u}_e(x,y,z,t) = \boldsymbol{N}(x,y)\boldsymbol{U}_e(z)e^{-i\omega t} = \begin{pmatrix} \sum_{a=1}^{4}\boldsymbol{N}_a(x,y)\overline{U}_{xa} \\ \sum_{a=1}^{4}\boldsymbol{N}_a(x,y)\overline{U}_{ya} \\ \sum_{a=1}^{4}\boldsymbol{N}_a(x,y)\overline{U}_{za} \end{pmatrix} e^{i(kz-\omega t)} = \\ = \boldsymbol{N}(x,y)\overline{\boldsymbol{U}}_e e^{i(kz-\omega t)}. \tag{43}$$

where $\overline{\boldsymbol{U}}_e$ is the nodal displacements vector containing displacements of each node in the directions of the three axes, $\boldsymbol{N}(x,y)$ is the matrix of approximation functions; a is the node number within the four nodded FE; $\overline{U}_x, \overline{U}_y$ and $\overline{U}_z$ are the nodal displacements of a -th node in the OX, OY and OZ directions, correspondingly, and i stands for imaginary units.

Vector $\boldsymbol{U}_e(z)$ denotes the Fourier transform of nodal displacement vector $\boldsymbol{u}_e(x,y,z,t)$ in respect to time t [13]:

$$\boldsymbol{u}_e(x,y,z,t) = \int_{-\infty}^{+\infty} \boldsymbol{U}_e(z)e^{-i\omega t}d\omega. \tag{44}$$

$\overline{\boldsymbol{U}}_e$ is the Fourier transform of $\boldsymbol{U}_e(z)$ in respect of the OZ direction:

$$\boldsymbol{U}_e(z) = \int_{-\infty}^{+\infty} \overline{\boldsymbol{U}}_e e^{ikz}dk. \tag{45}$$

By substituting (Eq. 43) by (Eq. 42), the strain-displacement relation reads as:

$$\boldsymbol{\varepsilon} = \left(\boldsymbol{L}_x\frac{\partial}{\partial x} \quad \boldsymbol{L}_y\frac{\partial}{\partial y} \quad \boldsymbol{L}_z\frac{\partial}{\partial z}\right)\boldsymbol{N}(x,y)\overline{\boldsymbol{U}}_e e^{i(kz-\omega t)} = \\ = (\boldsymbol{B}_1 + ik\boldsymbol{B}_2)\overline{\boldsymbol{U}}_e e^{i(kz-\omega t)}, \tag{46}$$

where $\boldsymbol{B}_1 = \boldsymbol{L}_x\frac{\partial \boldsymbol{N}(x,y)}{\partial x} + \boldsymbol{L}_y\frac{\partial \boldsymbol{N}(x,y)}{\partial y}$ and $\boldsymbol{B}_2 = \boldsymbol{L}_z\boldsymbol{N}(x,y)$.

When applying Hamilton’s virtual work principle for a single FE, it yields [59]:

$$\int_{t1}^{t2} \delta(E_s - E_k)dt = 0, \tag{47}$$

where δ stands for a virtual quantity; $\delta E_s = \int_{V_e} \delta \boldsymbol{\varepsilon}_e^T \boldsymbol{D}\, \boldsymbol{\varepsilon}_e dV_e$ is the variation of the strain energy, and $\delta E_k = \int_{V_e} \delta \dot{\boldsymbol{u}}_e^T \rho_e\, \dot{\boldsymbol{u}} dV_e$ is the variation of the kinetic energy within the volume of FE, ρ_e is the material density within the FE element, and T denotes the matrix conjugate transpose.

The integration of the kinetic term by parts and the virtual work principle yields [43]:

$$\int_{t1}^{t2} \left(\int_{V_e} \delta \boldsymbol{\varepsilon}_e^T \boldsymbol{D}\, \boldsymbol{\varepsilon}_e dV_e + \int_{V_e} \delta \boldsymbol{u}_e^T \rho\, \ddot{\boldsymbol{u}}_e dV_e \right) dt = 0. \tag{48}$$

The constitutive strain and the kinetic terms can be expanded to [43]:

$$\begin{gathered}\int_{V_e} \delta \boldsymbol{\varepsilon}_e^T \boldsymbol{D}\, \boldsymbol{\varepsilon}_e dV_e = \int_{S_e} \int_z \ \delta \left((\boldsymbol{B}_1 + ik\boldsymbol{B}_2) \overline{\boldsymbol{U}}_e e^{i(kz-\omega t)} \right)^T \boldsymbol{D} \cdot \\ \cdot (\boldsymbol{B}_1 + ik\boldsymbol{B}_2) \overline{\boldsymbol{U}}_e e^{i(kz-\omega t)} dz dS_e.\end{gathered} \tag{49}$$

and

$$\begin{gathered}\int_{V_e} \delta \boldsymbol{u}_e^T \rho\, \ddot{\boldsymbol{u}}_e dV_e = \int_{S_e} \int_z \ \delta \left(\boldsymbol{N}(x,y) \overline{\boldsymbol{U}}_e e^{i(kz-\omega t)} \right)^T \rho_e(-\omega^2) \cdot \\ \cdot \boldsymbol{N}(x,y)\, \overline{\boldsymbol{U}}_e e^{i(kz-\omega t)} dz dS_e.\end{gathered} \tag{50}$$

The complex wavenumber $k = Re(k) + i \cdot Im(k)$ describes the spatial configuration of the wave propagating along the waveguide. $Imag(k)$ means the exponent of the wave decay in space. In practical applications, attenuation is preferably measured in $\frac{Np}{m}$ (Nepers per meter, $1Np = 8.6859\ dB$), that is, $\frac{1}{Im(k)}$ is the distance over which the amplitude of the travelling wave decreases by $\frac{1}{e}$. As (Eq. 49) and (Eq. 50) produce complex quantities, the conjugate transposes of matrices are used where transposition converts complex numbers to their conjugates, as:

$$\begin{gathered}\int_{V_e} \delta \boldsymbol{\varepsilon}_e^T \boldsymbol{D}\, \boldsymbol{\varepsilon}_e dV_e = \int_{S_e} \int_z \ \delta \left(\overline{\mathbf{U}}_e^T (\boldsymbol{B}_1^T - ik^* \boldsymbol{B}_2^T) e^{-i(k^* z-\omega t)} \right) \boldsymbol{D} \cdot \\ \cdot (\boldsymbol{B}_1 + ik\boldsymbol{B}_2) \overline{\boldsymbol{U}}_e e^{i(kz-\omega t)} dz dS_e = \\ \int_{S_e} \int_z \ \delta \left(\overline{\mathbf{U}}_e^T (\boldsymbol{B}_1^T - ik^* \boldsymbol{B}_2^T) e^{-Im(k)z} e^{-i(Re(k)z-\omega t)} \right) \boldsymbol{D} \cdot \\ \cdot (\boldsymbol{B}_1 + ik\boldsymbol{B}_2) \overline{\boldsymbol{U}}_e e^{-Im(k)z} e^{i(Re(k)z-\omega t)} dz dS_e = \\ \int_{S_e} \int_z \ \delta \overline{\mathbf{U}}_e^T \left((\boldsymbol{B}_1^T - ik^* \boldsymbol{B}_2^T) e^{-2Im(k)} e^{-i(Re(k)z-\omega t)} \right) \boldsymbol{D} \cdot \\ \cdot (\boldsymbol{B}_1 + ik\boldsymbol{B}_2) e^{i(Re(k)z-\omega t)} \overline{\boldsymbol{U}}_e dz dS_e = \\ \int_{S_e} \int_z \ \delta \overline{\mathbf{U}}_e^T e^{-2Im(k)} \left((\boldsymbol{B}_1^T - ik^* \boldsymbol{B}_2^T) \right) \boldsymbol{D} \cdot (\boldsymbol{B}_1 + ik\boldsymbol{B}_2) \overline{\boldsymbol{U}}_e dz dS_e = \\ \frac{e^{-2Im(k)}}{-2Im(k)} \delta \overline{\mathbf{U}}_e^T \int_{S_e} \ ((\boldsymbol{B}_1^T \boldsymbol{D} \boldsymbol{B}_1 - ik^* \boldsymbol{B}_2^T \boldsymbol{D} \boldsymbol{B}_1 + \\ + ik \boldsymbol{B}_1^T \boldsymbol{D} \boldsymbol{B}_2 + k^* k \boldsymbol{B}_2^T \boldsymbol{D} \boldsymbol{B}_1)) dS_e \overline{\boldsymbol{U}}_e.\end{gathered} \tag{51}$$

and

$$\begin{aligned}\int_{V_e} \delta\boldsymbol{u}_e^T \rho\, \ddot{\boldsymbol{u}}_e dV_e &= \int_{S_e}\int_z \delta\bar{\mathbf{U}}_e^T \boldsymbol{N}(x,y)^T e^{-Im(k)} e^{-i(Re(k)z-\omega t)}\rho_e \cdot \\ &\cdot(-\omega^2)\boldsymbol{N}(x,y)\,\bar{\boldsymbol{U}}_e e^{-Im(k)} e^{i(Re(k)z-\omega t)} dz dS_e = \\ &= -\frac{e^{-2Im(k)}}{-2Im(k)}\omega^2\delta\bar{\mathbf{U}}_e^T \int_{S_e}\boldsymbol{N}(x,y)^T\rho_e\boldsymbol{N}(x,y)dS_e\,\bar{\boldsymbol{U}}_e,\end{aligned} \tag{52}$$

where k^* is the complex conjugate of k.

By substituting (Eq. 52) and (Eq. 51) into (Eq. 48), we obtain the finite element equation of the FE of the waveguide cross-section as:

$$\begin{aligned}\int_{t1}^{t2}\Big(\frac{e^{-2Im(k)}}{-2Im(k)}\delta\bar{\mathbf{U}}_e^T(\boldsymbol{K}_{1e} + ik\boldsymbol{K'}_{2e} - ik^*\boldsymbol{K'}^T_{2e} + \\ + k^*k\boldsymbol{K}_{3e} - \omega^2\boldsymbol{M}_e)\,\bar{\boldsymbol{U}}_e\Big)dt = 0,\end{aligned} \tag{53}$$

where the FE matrices read as:

$$\boldsymbol{M}_e = \int_x\int_y \boldsymbol{N}(x,y)^T\rho_e\boldsymbol{N}(x,y)\,dxdy,$$

$$\boldsymbol{K}_{1e} = \int_x\int_y \boldsymbol{B}_1^T\boldsymbol{D}\boldsymbol{B}_1\,dxdy,$$

$$\boldsymbol{K'}_{2e} = \int_x\int_y \boldsymbol{B}_1^T\boldsymbol{D}\boldsymbol{B}_2\,dxdy,$$

$$\boldsymbol{K}_{3e} = \int_x\int_y \boldsymbol{B}_2^T\boldsymbol{D}\boldsymbol{B}_2\,dxdy,$$

where $\boldsymbol{M}_e$ is the mass matrix, $\boldsymbol{K}_{1e}$ is the stiffness matrix related with planar deformations of the cross-section, $\boldsymbol{K}_{3e}$ is the symmetric stiffness matrix related with the out-of-plane deformations, $\boldsymbol{K'}_{2e} - \boldsymbol{K'}^T_{2e}$ is the skew symmetric stiffness matrix which couples planar and out-of-plane effects.

The integrals in (Eq. 53) are computed by using the Gaussian quadrature rule. Since the term $\frac{e^{-2Im(k)}}{-2Im(k)}$ can be arbitrary (infinite length in the OZ direction) due to the arbitrary nature of the variation of the displacements, thus SAFE Eigenvalue equation for FE becomes:

$$\left(\boldsymbol{K}_{1e} + ik\boldsymbol{K'}_{2e} - ik^*\mathbf{K'}^T_{2e} + k^*k\boldsymbol{K}_{3e} - \omega^2\boldsymbol{M}_e\right)\bar{\boldsymbol{U}}_e e^{i(kz-\omega t)} = 0. \tag{54}$$

As external excitation in terms of the cross-section tractions is given, the SAFE equation reads as:

$$\begin{aligned}\left(\boldsymbol{K}_{1e} + ik\boldsymbol{K'}_{2e} - ik^*\boldsymbol{K'}^T_{2e} + k^*k\boldsymbol{K}_{3\mathrm{e}} - \omega^2\boldsymbol{M}_e\right)\bar{\boldsymbol{U}}_e e^{i(kz-\omega t)} = \\ = \boldsymbol{F}_e(z)e^{-i\omega t} = \bar{\boldsymbol{F}}_e e^{i(kz-\omega t)},\end{aligned} \tag{55}$$

where $\bar{\boldsymbol{F}}_e$ is a nodal vector of external forces acting upon FE throughout all the length of the waveguide given as a propagating excitation wave.

As SAFE matrices and vectors are assembled to the SAFE structural matrix and vector, the structural SAFE equation is obtained as:

$$\left(\boldsymbol{K}_1 + ik\boldsymbol{K'}_2 - ik^*\boldsymbol{K'}^T_2 + k^*k\boldsymbol{K}_3 - \omega^2\boldsymbol{M}\right)\bar{\boldsymbol{U}}e^{i(kz-\omega t)} = \bar{\boldsymbol{F}}e^{i(kz-\omega t)}, \tag{56}$$

where $\overline{\boldsymbol{U}}$ is the global vector of unknown nodal displacements over the cross-section.

In case $\overline{\boldsymbol{F}} = \boldsymbol{0},$ the homogenous version of (Eq. 56) is obtained as:

$$\left(\boldsymbol{K}_1 + ik\boldsymbol{K'}_2 - ik^*\boldsymbol{K'}_2^T + k^*k\boldsymbol{K}_3 - \omega^2\boldsymbol{M}\right)\overline{\boldsymbol{U}}e^{i(kz-\omega t)} = 0, \tag{57}$$

which is treated as an Eigenvalue problem with ω or k treated as the unknowns.

2.2 Dispersion Relations

2.2.1 Dispersion Curves

The solution of a complex Eigenvalue problem (Eq. 57) at numerous ω values within the selected range provides a number of propagating wave modes. The modes are presented in terms of k, $\boldsymbol{U}$ pairs of the wavenumber, and oscillatory displacement shape over the cross section. The number of the obtained modes at each ω value depends on the refinement of the FE mesh over the cross-section of the waveguide. Each modal displacement shape defines the type of the wave. The relationship of the wavenumbers of the same type of the wave against the frequency values is referred to as the dispersion relationship (the dispersion curve) of the particular type of the wave. The dispersion relationships of the real waveguides are all non-linear.

Wavenumbers k may be real, complex or purely imaginary values. Real values k represent propagating waves. In such a case, $k^* = k$, therefore, (Eq. 57) can be simplified as:

$$\left(\boldsymbol{K}_1 + ik\left(\boldsymbol{K'}_2 - \boldsymbol{K'}_2^T\right) + k^2\boldsymbol{K}_3 - \omega^2\boldsymbol{M}\right)\overline{\boldsymbol{U}}e^{i(\mathrm{k}z-\omega t)} = \boldsymbol{0}. \tag{58}$$

Complex wavenumbers k represent damped waves. Complex wavenumbers are obtained from (Eq. 58), however, they are mathematically correct only in case $Re(k) \gg Im(k)$, until relation $(k^* \approx k)$ may be assumed as approximately valid. In a general case, the matrix expression in (Eq. 58) has to be adjusted by taking into account the real and imaginary parts of k^* thus generating a non-linear Eigenvalue problem.

Purely imaginary k values $(k^* = -k)$, or $Re(k) \ll Im(k)$ represent end-mode solutions as ‘non-propagating waves’. In such a case (Eq. 58) reads as:

$$\left(\boldsymbol{K}_1 + ik\left(\boldsymbol{K'}_2 + \boldsymbol{K'}_2^T\right) - k^2\boldsymbol{K}_3 - \omega^2\boldsymbol{M}\right)\overline{\boldsymbol{U}}e^{i(\mathrm{k}z-\omega t)} = \boldsymbol{0}. \tag{59}$$

In our further exploration, we shall use Eigenvalue problem formulation (Eq. 58) for obtaining solutions which are able to approximately describe weakly-evanescent guided waves.

Equation (Eq. 57) is a quadratic Eigenvalue problem with respect to k. It may be transformed into the first order problem as [59]:

$$(\boldsymbol{A} - k\boldsymbol{B})\boldsymbol{Q} = \boldsymbol{P}, \tag{60}$$

where

$$\boldsymbol{A} = \begin{pmatrix} \boldsymbol{0} & \boldsymbol{K}_1 - \omega^2\boldsymbol{M} \\ \boldsymbol{K}_1 - \omega^2\boldsymbol{M} & i\boldsymbol{K}_2 \end{pmatrix}, \boldsymbol{B} = \begin{pmatrix} \boldsymbol{K}_1 - \omega^2\boldsymbol{M} & \boldsymbol{0} \\ \boldsymbol{0} & -\boldsymbol{K}_3 \end{pmatrix}, \boldsymbol{Q} = \begin{pmatrix} \overline{\boldsymbol{U}} \\ k\overline{\boldsymbol{U}} \end{pmatrix}$$

$$\boldsymbol{P} = \begin{pmatrix} \boldsymbol{0} \\ \overline{\boldsymbol{F}} \end{pmatrix} \text{ and } \boldsymbol{K}_2 = \boldsymbol{K'}_2 - \boldsymbol{K'}_2^T.$$

The homogenous version of equation (Eq. 60) reads as:

$$(\boldsymbol{A} - k\boldsymbol{B})\boldsymbol{V} = \boldsymbol{0}, \tag{61}$$

where for each given real ω value $2 \times TotalDegreesOfFreedom = 2N$, natural wavenumbers k with corresponding natural vectors describing the shape of the mode may be obtained.

Simultaneously, we formulate the left Eigenvalue problem as:

$$\boldsymbol{W}(\boldsymbol{A} - k\boldsymbol{B}) = \boldsymbol{0} \tag{62}$$

even though vector $\boldsymbol{W}_{1\times 2N}$ has no immediate physical meaning.

Further, we shall use notations for the first halves of vectors $\boldsymbol{V}$, $\boldsymbol{W}$ as $\boldsymbol{v}_{N\times 1}$ and $\boldsymbol{w}_{N\times 1}$, where:

$$\boldsymbol{W}_j = \begin{pmatrix} \boldsymbol{w}_j & k\boldsymbol{w}_j \end{pmatrix} \text{ and } \boldsymbol{V}_j = \begin{pmatrix} \boldsymbol{v}_j \\ k\boldsymbol{v}_j \end{pmatrix}.$$

The natural wavenumber values are obtained from (Eq. 58) in pairs. Solutions with positive and negative $Re(k)$ parts represent propagating wave modes in the forward and backward $0Z$ directions, correspondingly. Complex solutions $\pm(Re(k) + i \cdot Im(k))$ represent evanescent waves with the amplitude decaying along $0Z$. Solutions $\pm(Re(k) - i \cdot Im(k))$ have no physical meaning [94]. Pairs of purely imaginary solutions with positive and negative $Im(k)$ values represent non-propagating end-modes. The immediate practical value can be traced in the propagating and evanescent (in the case of a dissipative environment) wave solutions.

The algorithm to acquire dispersion relations for propagative waves using SAFEM is summarized in (Fig. 2.2).

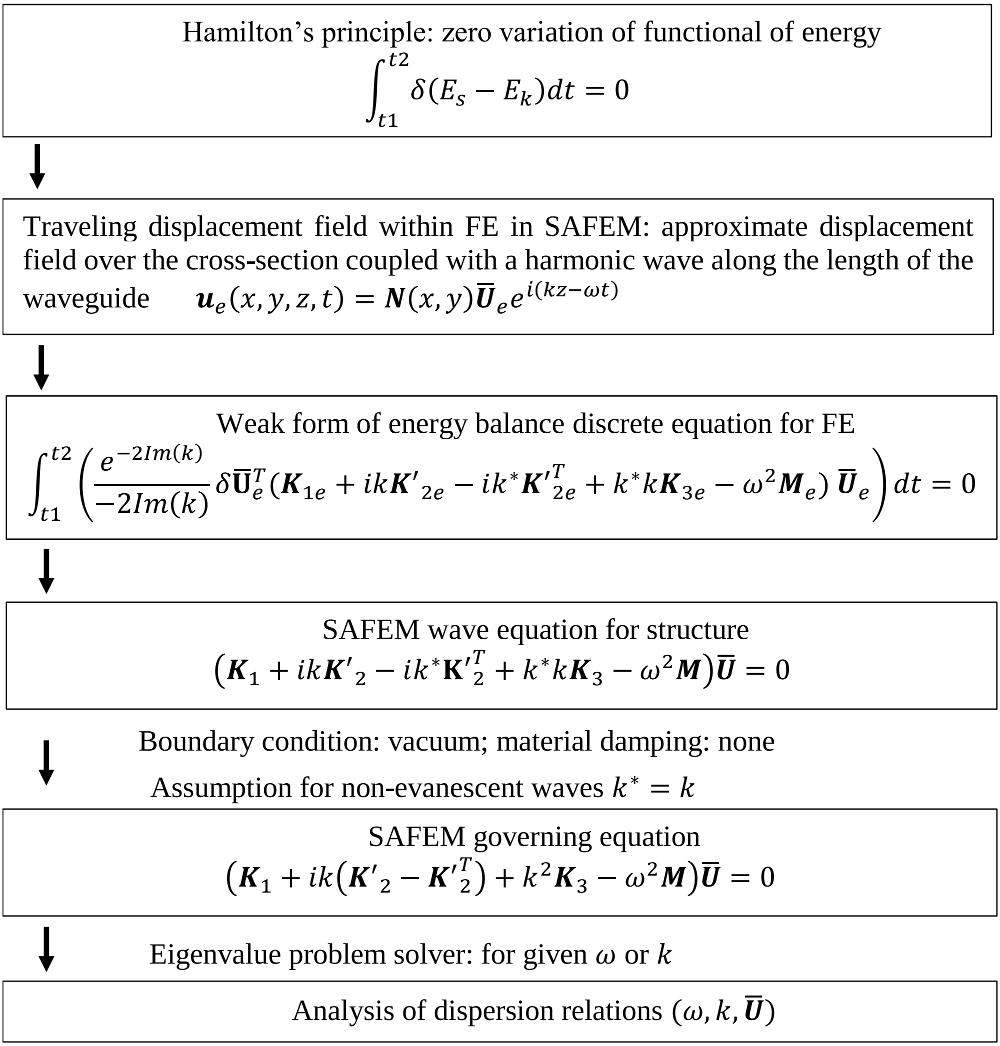

Hamilton’s principle: zero variation of functional of energy

$$\int_{t1}^{t2}\delta(E_s-E_k)dt=0$$

Traveling displacement field within FE in SAFEM: approximate displacement field over the cross-section coupled with a harmonic wave along the length of the waveguide $\boldsymbol{u}_e(x,y,z,t)=\boldsymbol{N}(x,y)\bar{\boldsymbol{U}}_e e^{i(kz-\omega t)}$

Weak form of energy balance discrete equation for FE

$$\int_{t1}^{t2}\left(\frac{e^{-2Im(k)}}{-2Im(k)}\delta\bar{\mathbf{U}}_e^T(\boldsymbol{K}_{1e}+ik\boldsymbol{K'}_{2e}-ik^*\boldsymbol{K'}_{2e}^T+k^*k\boldsymbol{K}_{3e}-\omega^2\boldsymbol{M}_e)\,\bar{\boldsymbol{U}}_e\right)dt=0$$

SAFEM wave equation for structure

$$\left(\boldsymbol{K}_1+ik\boldsymbol{K'}_2-ik^*\mathbf{K'}_2^T+k^*k\boldsymbol{K}_3-\omega^2\boldsymbol{M}\right)\bar{\boldsymbol{U}}=0$$

Boundary condition: vacuum; material damping: none

Assumption for non-evanescent waves $k^*=k$

SAFEM governing equation

$$\left(\boldsymbol{K}_1+ik\left(\boldsymbol{K'}_2-\boldsymbol{K'}_2^T\right)+k^2\boldsymbol{K}_3-\omega^2\boldsymbol{M}\right)\bar{\boldsymbol{U}}=0$$

Eigenvalue problem solver: for given ω or k

Analysis of dispersion relations $(\omega,k,\bar{\boldsymbol{U}})$

Fig. 2.2. Flowchart of the algorithm to obtain dispersion relations for propagating waves using SAFEM.

For the model verification purposes, dispersions curves of a steel waveguide with a rectangular cross-section $0.00508\times 0.00508\,m$ were calculated. The material properties were: mass density $\rho=7850\frac{kg}{m^3}$, Young’s modulus $E=2\cdot 10^{11}\,Pa$ and Poisson’s ratio $\nu=0.3$. The FE mesh was 4×4 over the cross-section of the waveguide. (Fig. 2.3) (a) and (b) show $f(k)$ and $k(f)$ solutions presented as dispersion curves for the forward-direction travelling waves, where $f=\frac{\omega}{2\pi}$ is the frequency in cycles per second. The $f(k)$ solutions are acquired from the homogenous version of equation (Eq. 60), where wavenumber k is considered to be given, and its values run in the range of $0-250\,1/m$. The $k(f)$ solutions are acquired from the homogenous version of equation (Eq. 60), when frequency f is considered to be given, and its values run in the range of $0 - 1\ MHz$. The results agreed reasonably well with those published by Hayashi and were backed up by experimental data presented in [34].

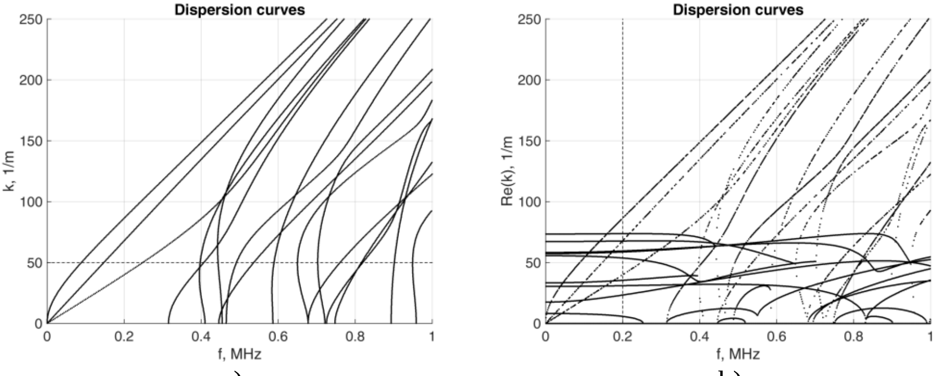

a) b)

Fig. 2.3. (a) $f(k)$ solutions with $k = 50\ 1/m$ are shown as the dotted line mark; (b) $k(f)$ solutions with $f = 0.2\ MHz$ are shown as the dotted line mark.

(Fig. 2.4) shows the classified natural wavenumbers for forward and backward traveling waves at $f = 0.2\ MHz$ in the complex plane, where the symmetry in-between wavenumbers is evident. Four forward-propagating modes were obtained as two identical pairs because of the square shape of the waveguide.

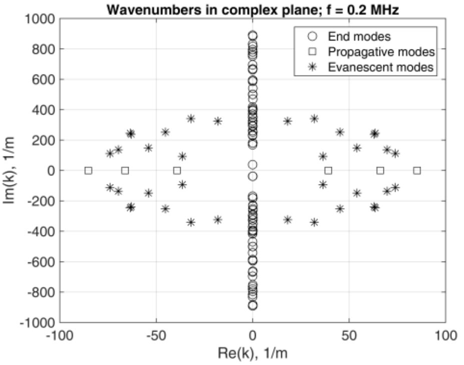

Fig. 2.4. Natural wavenumbers in the complex number plane at $f = 0.2\ MHz$.

For representation purposes, the set of numerous obtained natural wavenumbers was classified in order to distinguish among the propagating, evanescent and end-mode waves from each other. As the natural wavenumbers are always calculated with a certain numerical error, the symmetry of the values over the complex plane implies that arithmetic averages of real and imaginary parts should be calculated. Several similarity measures are used in order to determine the type of symmetry of the obtained natural wavenumbers.

(Fig. 2.5) summarizes the convergence of $k(f)$ fundamental modes solutions at $f = 0.2\ MHz$ (the doted vertical line in (Fig. 2.3 (b)). It can be seen that a small number of FE in the squared $N \times N$ cross-section yields the wavenumber of the longitudinal mode to converge rapidly. The accuracy of the solutions for the flexural and torsional modes is more sensitive to the mesh size.

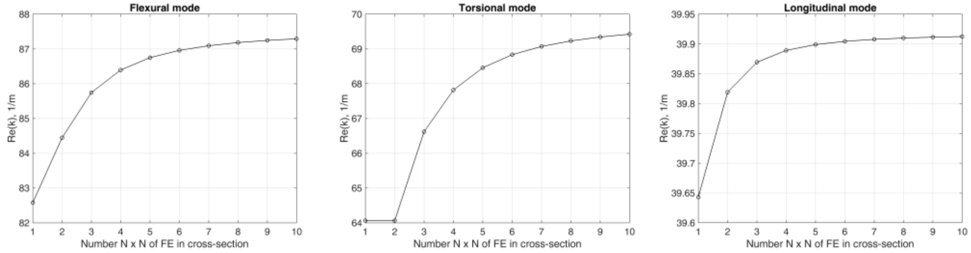

a) b) c)

Fig. 2.5. The convergence of the wavenumber of the fundamental (a) flexural, (b) torsional and (c) longitudinal modes of $k(f)$ solutions due the increment of the mesh size at $f = 0.2\,MHz$.

A similar convergence behavior is seen in (Fig. 2.6) for $f(k)$ fundamental modes at given wavenumber $k = 50\ 1/m$ (the horizontal dotted line in Fig. 2.3 (a)).

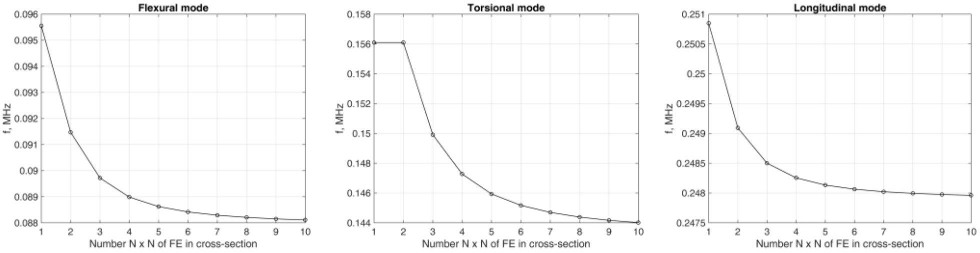

Fig. 2.6. The convergence of frequency of the fundamental (a) flexural, (b) torsional and (c) longitudinal modes of $f(k)$ solutions due to the increment of the mesh size at $k = 50\ 1/m$.

It can be noted that the 10×10 FE cross-section assures sufficiently accurate dispersion relations results for $f(k)$ and $k(f)$ fundamental modes.

2.2.2 Phase and Group Velocities

Along with the dispersion relations, phase velocity $c_{ph} = \frac{\omega}{Re(k)}$ is another way for expressing the relations between the wavelength, which is the inverse of the real part of k, and frequency. (Fig. 2.7) (a) and (b) shows the phase velocities of propagative modes of the same waveguide presented by 10×10 and 6×6 FEs over the cross-section. The theoretical values of longitudinal [35] $c_L = \sqrt{\frac{E(1-\nu)}{\rho(1+\nu)(1-2\cdot\nu)}}$, shear $c_S = \sqrt{\frac{E}{2\cdot\rho(1+\nu)}}$ and bar $c_b = \sqrt{\frac{E}{\rho}}$ (the speed of sound for the pressure wave) velocities are presented by the dashed lines. The phase velocities of fundamental flexural F_0 and longitudinal L_0 modes approach Rayleigh wave velocity

$c_R \approx \frac{0,862+1.14\nu}{1+\nu} c_S$ as the frequency increases. Velocity c_b coincides with the velocity of L_0 mode at the zero frequency. Phase velocities of higher order modes velocities approach c_L at higher frequencies, see (Fig. 2.7 (b)). The phase velocity of the fundamental torsional mode T_0, which, in the case of plates and cylindrical bars, coincides with c_S and is nondispersive, reaches the value of $c_{torsional} \approx 0.92c_S$ [95]. However, over a higher frequency range, it does not approach the horizontal line of c_S any more, thus implying a low dispersion. The phase velocities of L_0, F_0 tend towards c_S due to their numerical errors.

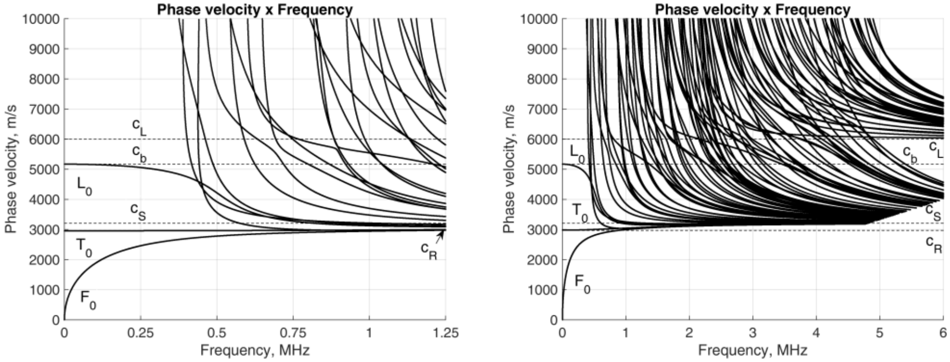

a) b)

Fig. 2.7. Phase velocity of a square bar with a mesh of 10 × 10 (a) and 6 × 6 (b) on the cross-section.

The group velocity represents the velocity at which the mechanical energy travels in a lossless waveguide and is defined as $c_{gr} = \frac{\partial \omega}{\partial k}$. The phase and group velocities are interlinked through Rayleigh's formula:

$$c_{gr} = \frac{c_{ph}}{\left(1 - \frac{\omega}{c_{ph}} \frac{\partial c_{ph}}{\partial \omega}\right)}. \tag{63}$$

For example, two similar (in terms of frequency) harmonic waves of the same mode added together result in an envelope wave due to the fact that the phase velocity varies with frequency. The velocity of the formed packet (envelope) travels at the group velocity. The effect of dispersion on a propagating mode means that the shape of the wave packet is distorted, and the peak amplitude of the packet decreases in space.

However, if the wave transferring medium is non-dispersive, the phase and group velocities coincide.

Tracking a separate mode over the frequency axis might be a challenging task since many modes with close wavenumbers exist – it is evident in (Fig. 2.3 (b)). Therefore, the usage of direct numerical differentiation $\frac{\omega+\Delta\omega}{k+\Delta k}$ might produce misleading results by losing the observed mode.

For given ω, the group velocity of the j-th mode could be derived from homogenous equation (Eq. 58) by taking the derivative with respect to the wavenumber as [43]:

$$\frac{\partial(-\omega^2\boldsymbol{M}+\boldsymbol{K}_1+ik\boldsymbol{K}_2+k^2\boldsymbol{K}_3)\boldsymbol{v}}{\partial k} = \left(-2\omega\frac{\partial\omega}{\partial k}\boldsymbol{M} + i\boldsymbol{K}_2 + 2k\boldsymbol{K}_3\right)\boldsymbol{v} = \boldsymbol{0}. \tag{64}$$

Pre-multiplying (Eq. 64) by the left natural vector $\boldsymbol{w}$ gives [43]:

$$\boldsymbol{w}\left(-2\omega\frac{\partial\omega}{\partial k}\boldsymbol{M} + i\boldsymbol{K}_2 + 2k\boldsymbol{K}_3\right)\boldsymbol{v} = \boldsymbol{0}. \tag{65}$$

Eventually, we obtain [43]:

$$c_{gr} = \frac{\partial\omega}{\partial k} = \frac{\boldsymbol{w}_j(i\boldsymbol{K}_2+2k_j\boldsymbol{K}_3)\boldsymbol{v}_j}{2\omega\boldsymbol{w}_j\boldsymbol{M}\boldsymbol{v}_j}. \tag{66}$$

(Fig. 2.8) shows the results obtained by applying (Eq. 66) for the waveguide with a 4×4 FEs mesh.

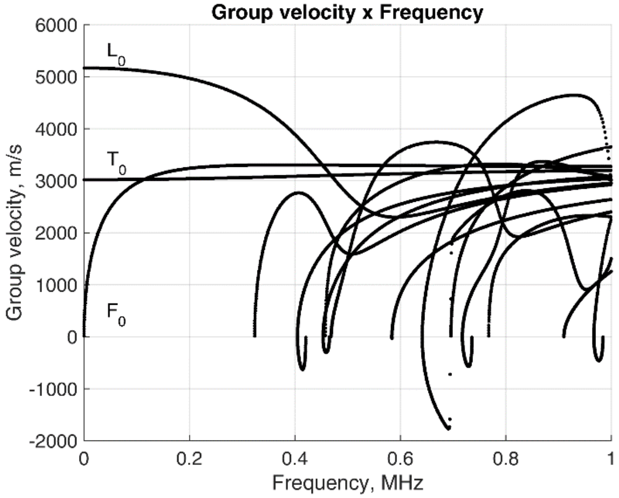

Fig. 2.8. Group velocity.

It may be observed that the modes with negative group velocities do exist, which indicates that the mechanical energy of the wave travels in the direction opposite to that of the phase velocity at particular frequency ranges. Unlike plates and cylindrical bars, the group velocity of T_0 mode is also denoted by low dispersion.

In the practical ultrasound applications group, the velocity dispersion curves are used to recognize and isolate modes observing different arrival times in the signals obtained when employing experimental measures.

2.3 Excitation of Guided Waves in Waveguide

2.3.1 Single Frequency Response

The j-th mode k_j and $\boldsymbol{V}_j$ satisfies the equation:

$$(\boldsymbol{A} - k_j\boldsymbol{B})\boldsymbol{V}_j = \boldsymbol{0}, \tag{67}$$

where the right natural vector $\boldsymbol{V}_j$ has a clear physical interpretation as the displacement profile of the propagating wave over the cross-section of the waveguide.

The natural wavenumber k_m and $\boldsymbol{W}_m$ are obtained as a solution of the left Eigenvalue problem as:

$$\boldsymbol{W}_m(\boldsymbol{A} - k_m\boldsymbol{B}) = \boldsymbol{0}. \tag{68}$$

Pre-multiplying (Eq. 67) by $\boldsymbol{W}_m$ and post-multiplying (Eq. 68) by $\boldsymbol{V}_j$ yields the following relations:

$$\begin{cases} \boldsymbol{W}_m\left(\boldsymbol{A} - k_j\boldsymbol{B}\right)\boldsymbol{V}_j = \boldsymbol{0} \\ \boldsymbol{W}_m(\boldsymbol{A} - k_m\boldsymbol{B})\boldsymbol{V}_j = \boldsymbol{0}. \end{cases} \tag{69}$$

This expands to:

$$\begin{cases} \boldsymbol{W}_m\boldsymbol{A}\boldsymbol{V}_j - \boldsymbol{W}_m k_j \boldsymbol{B}\boldsymbol{V}_j = \boldsymbol{0} \\ \boldsymbol{W}_m\boldsymbol{A}\boldsymbol{V}_j - \boldsymbol{W}_m k_m \boldsymbol{B}\boldsymbol{V}_j = \boldsymbol{0}. \end{cases} \tag{70}$$

which is equivalent to the left and right natural vector orthogonality relations:

$$\begin{cases} \boldsymbol{W}_m\boldsymbol{A}\boldsymbol{V}_j = \begin{cases} \boldsymbol{W}_j\boldsymbol{A}\boldsymbol{V}_j & j = m \\ 0 & j \neq m \end{cases} \\ \boldsymbol{W}_m\boldsymbol{B}\boldsymbol{V}_j = \begin{cases} \boldsymbol{W}_j\boldsymbol{B}\boldsymbol{V}_j & j = m \\ 0 & j \neq m \end{cases} \\ k_j = \frac{\boldsymbol{W}_j\boldsymbol{A}\boldsymbol{V}_j}{\boldsymbol{W}_j\boldsymbol{B}\boldsymbol{V}_j}. \end{cases} \tag{71}$$

Any vector of length l can be cast in the basis of l independent vectors. In the case of external loading presented in (Eq. 60) as $\boldsymbol{P}$, solution $\boldsymbol{Q}$ is presented as the weighted superposition of natural vectors [34]:

$$\boldsymbol{Q} = \sum_{j=1}^{2N} o_j \boldsymbol{V}_j. \tag{72}$$

(Eq. 60) can now be presented as [34]:

$$(\boldsymbol{A} - k\boldsymbol{B})\sum_{j=1}^{2N} o_j \boldsymbol{V}_j = \boldsymbol{P}. \tag{73}$$

Pre-multiplying (eq. 73) equation by left natural vector $\boldsymbol{W}_m$ yields [34]:

$$\sum_{j=1}^{2N}(\boldsymbol{W}_m\boldsymbol{A}\boldsymbol{V}_j - k\boldsymbol{W}_m\boldsymbol{B}\boldsymbol{V}_j)o_j = \boldsymbol{W}_m\boldsymbol{P}. \tag{74}$$

Due to the orthogonality of the natural vectors, the scalar weight of the m-th natural vector reads as [34]:

$$o_m = \frac{\boldsymbol{W}_m\boldsymbol{P}}{(k_m - k)\boldsymbol{W}_m\boldsymbol{B}\boldsymbol{V}_m}. \tag{75}$$

And, finally, the nodal displacement vector is [34]:

$$\overline{\boldsymbol{U}} = \sum_{m=1}^{2N} o_m \boldsymbol{v}_m. \tag{76}$$

The force is considered to be applied at a particular point z_0 on the $0Z$ axis over the cross-section of the waveguide as nodal amplitudes vector $\overline{\boldsymbol{F}}(z) = \overline{\boldsymbol{F}}\delta(z - z_0)$.

The weight of the m-th mode contribution to the overall solution can now reads as [34]:

$$o_m = \frac{\boldsymbol{W}_m \boldsymbol{P}}{(k_m - k)\boldsymbol{W}_m \boldsymbol{B} \boldsymbol{V}_m} \delta(z - z_0), \tag{77}$$

where δ defines the Dirac delta. The substitution of (Eq. 77) into (Eq. 76) yields:

$$\overline{\boldsymbol{U}} = \sum_{m=1}^{2N} \frac{-\boldsymbol{W}_m \boldsymbol{P}}{(k - k_m)\boldsymbol{W}_m \boldsymbol{B} \boldsymbol{V}_m} \boldsymbol{v}_m \, \delta(z - z_0). \tag{78}$$

Since $\boldsymbol{U}(z)$ is a Fourier transform with respect to wavenumber k (Eq. 45), the application of Cauchy residue theorem [34] leads to:

$$\boldsymbol{U}(z) = i \sum_{m=1}^{N} \frac{-\boldsymbol{W}_m \boldsymbol{P}}{\boldsymbol{W}_m \boldsymbol{B} \boldsymbol{V}_m} \boldsymbol{v}_m \, e^{i(k_m(z - z_0))}. \tag{79}$$

Displacements expressed by relation (Eq. 79) at points $z > z_0$ are expressed via the superposition of N modes propagating forwards. At points $z < z_0$ in relation to (Eq. 79), the backwards-propagating modes are engaged. Relation (Eq. 79) can also be considered as a response to the general excitation, while both types of modes (propagating and evanescent) are engaged. Finally, the displacement vector as a response to a harmonic load with particular angular frequency ω is obtained as:

$$\boldsymbol{u}(x, y, z, t) = i\boldsymbol{N}(\boldsymbol{x}, \boldsymbol{y}) \sum_{m=1}^{N} \frac{-\boldsymbol{W}_m \boldsymbol{P}}{\boldsymbol{W}_m \boldsymbol{B} \boldsymbol{V}_m} \boldsymbol{v}_m \, e^{i(k_m(z - z_0) - \omega t)}. \tag{80}$$

It is worth noting that the calculation of the left-side natural vectors for lossless waveguides is not necessary. They can be substituted by the right-side ones as both $\boldsymbol{A}$ and $\boldsymbol{B}$ are Hermitian matrices ($\boldsymbol{A}^T = \boldsymbol{A}$ and $\boldsymbol{B}^T = \boldsymbol{B}$) because of the symmetry of matrices $\boldsymbol{K}_1, \boldsymbol{K}_3, \boldsymbol{M}$ and skew-symmetry of matrix $\boldsymbol{K}_2$. Under such conditions, (Eq. 68) may be re-cast as:

$$(\boldsymbol{A} - k^* \boldsymbol{B})\boldsymbol{W}^T = \boldsymbol{0}. \tag{81}$$

For propagating modes corresponding to real valued natural wavenumbers, the left natural vectors can be obtained as $\boldsymbol{W} = \boldsymbol{V}^T$ since $k^* = k$. In the case of complex natural wavenumbers $Re(k) + i \cdot Im(k)$ and $0 + i \cdot Im(k)$, the left-side natural vectors are conjugate transposes of the right ones as $Re(k) - i \cdot Im(k)$ and $0 - i \cdot Im(k)$, respectively. The graphical point of feasibility for the above mentioned substitutions is clearly depicted in (Fig. 2.4). In the presence of damping, the technique for overcoming the necessity of the left-side natural vector calculation has been proposed by Gavrić and Hladky-Hennion [21, 96]. They suggested a displacement field at the FE level in order to obtain real symmetric matrices in homogenous (Eq. 43):

$$\boldsymbol{u}_e(x,y,z,t)=\boldsymbol{N}(x,y)\begin{pmatrix}\bar{U}_{ex}e^{i(kz-\omega t)}\\ \bar{U}_{ey}e^{i(kz-\omega t)}\\ \bar{U}_{ez}e^{i\left(\frac{\pi}{2}+kz-\omega t\right)}\end{pmatrix}=$$
$$=\boldsymbol{N}(x,y)\begin{pmatrix}\bar{U}_{ex}e^{i(kz-\omega t)}\\ \bar{U}_{ey}e^{i(kz-\omega t)}\\ \bar{U}_{ez}e^{i\frac{\pi}{2}}e^{i(kz-\omega t)}\end{pmatrix}=\boldsymbol{N}(x,y)\begin{pmatrix}\bar{U}_{ex}e^{i(kz-\omega t)}\\ \bar{U}_{ey}e^{i(kz-\omega t)}\\ i\bar{U}_{ez}e^{i(kz-\omega t)}\end{pmatrix}. \quad (82)$$

As an equivalent to this field, Viola [43] instead introduced a quadratic $N \times N$ matrix $\boldsymbol{T}$ which has units in the diagonal, except that every third term is imaginary unit i:

$$\boldsymbol{T}=\begin{pmatrix}1&0&0&\cdots&0&0&0\\0&1&0&\cdots&0&0&0\\0&0&i&\cdots&0&0&0\\\vdots&\vdots&\vdots&\ddots&\vdots&\vdots&\vdots\\0&0&0&\cdots&1&0&0\\0&0&0&\cdots&0&1&0\\0&0&0&\cdots&0&0&i\end{pmatrix} \quad (83)$$

Pre-multiplying (Eq. 58) by $\boldsymbol{T}^T$ yields:

$$\begin{gathered}\boldsymbol{T}^T\left(\boldsymbol{K}_1+ik\left(\boldsymbol{K'}_2-\boldsymbol{K'}_2^T\right)+k^2\boldsymbol{K}_3-\omega^2\boldsymbol{M}\right)\boldsymbol{T}\boldsymbol{T}^{-1}\,\bar{\boldsymbol{U}}e^{i(\mathrm{kz}-\omega t)}=\\=(\boldsymbol{T}^T\,\boldsymbol{K}_1\boldsymbol{T}+ik\boldsymbol{T}^T\boldsymbol{K}_2\boldsymbol{T}+k^2\boldsymbol{T}^T\boldsymbol{K}_3\boldsymbol{T}-\omega^2\boldsymbol{T}^T\boldsymbol{M}\boldsymbol{T})\boldsymbol{T}^{-1}\,\bar{\boldsymbol{U}}e^{i(\mathrm{kz}-\omega t)}=\\=\left(\boldsymbol{K}_1+k\widehat{\boldsymbol{K}}_2+k^2\boldsymbol{K}_3-\omega^2\boldsymbol{M}\right)\widehat{\boldsymbol{U}}e^{i(\mathrm{kz}-\omega t)}=\boldsymbol{0}\end{gathered} \quad (84)$$

where $\widehat{\boldsymbol{U}}=\boldsymbol{T}^{-1}\,\bar{\boldsymbol{U}}$ and $\boldsymbol{T}^T\,\boldsymbol{K}_2\boldsymbol{T}=-i\widehat{\boldsymbol{K}}_2$, because matrix $\boldsymbol{K}_2=\boldsymbol{K'}_2-\boldsymbol{K'}_2^T$ is skew symmetric; $\boldsymbol{T}^T\,\boldsymbol{K}_1\boldsymbol{T}=\boldsymbol{K}_1$, $\boldsymbol{T}^T\,\boldsymbol{K}_3\boldsymbol{T}=\boldsymbol{K}_3$, $\boldsymbol{T}^T\,\boldsymbol{M}\boldsymbol{T}=\boldsymbol{M}$ due to the symmetry of $\boldsymbol{K}_1$, $\boldsymbol{K}_3$ and $\boldsymbol{M}$; the transform matrix $\boldsymbol{T}$ has a property of $\boldsymbol{T}^T=\boldsymbol{T}^*=\boldsymbol{T}^{-1}$.

The matrices become real and symmetric in (Eq. 84), and, as a result of this, the corresponding homogenous (Eq. 61) yields $\boldsymbol{W'}=\pm\boldsymbol{V}$, where $\boldsymbol{W'}$ contains the left natural vector $\boldsymbol{W}$ in $2N\times 1$ dimensions, while the alternating sign cancels in (Eq. 79).

However, a more convenient way to obtain the left natural vectors from the right ones by omitting algebra manipulations with $\boldsymbol{T}$ is the introduction of transformation matrix $\boldsymbol{G}$ which differs from $\boldsymbol{T}$ by substituting the imaginary unit i with -1. After acquiring the right natural vector from (Eq. 61), the left one is simply obtained as follows:

$$\boldsymbol{W'}=\boldsymbol{G}\boldsymbol{V}. \quad (85)$$

(Eq. 85) allows calculating only the right natural vectors.

2.3.2 Non-Harmonic Force Response

What concerns the general time law, the excitation of the guided wave can be presented as a superposition of numerous Fourier components. In such a case, the response to each single harmonic component is obtained as described in the previous section. The overall response equals the sum of time relationships corresponding to all the single-frequency responses. Further in this study, non-harmonic force response analysis is discussed.

Let us consider an aluminum waveguide of mass density $\rho = 2700\ \frac{kg}{m^3}$, Young's modulus $E\ = 70\ \cdot\ 10^9\ \ Pa$ and Poisson's ratio $\nu = 0.33$. The cross-section of the waveguide is $0.001\ \times\ 0.0011\ m$, which is slightly different from a square in order to avoid multiple natural wavenumbers as it was considered in our simulation. Let us consider the external loading as the shearing force applied along a source (Fig. 2.9). The time law is given as a Hanning-windowed 5 cycle sinus burst centered at $250\ kHz$ (Fig. 2.10 (a)).

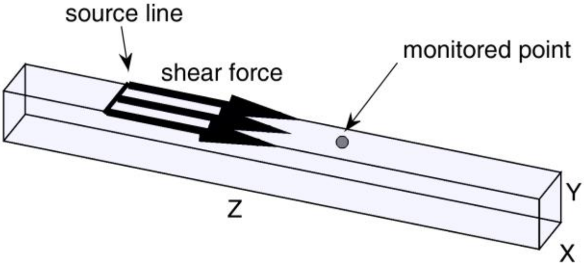

Fig. 2.9. A schematic representation of excitation.

(Fig. 2.10 (b)) displays the frequency spectrum of the modulated loading impulse. It is obtained by applying the fast Fourier transform (FFT) to the time relationship shown in (Fig. 2.10 (a)), which is followed by zero padding 50 times the duration of the impulse. The threshold for the meaningful harmonic components is assumed as $0.05\ \%$. The FFT sampling frequency was $250\ GHz$. The sum of the displacement vectors of all the harmonic components of the response in accordance with relation (Eq. 80) provides the overall response to the loading impulse.

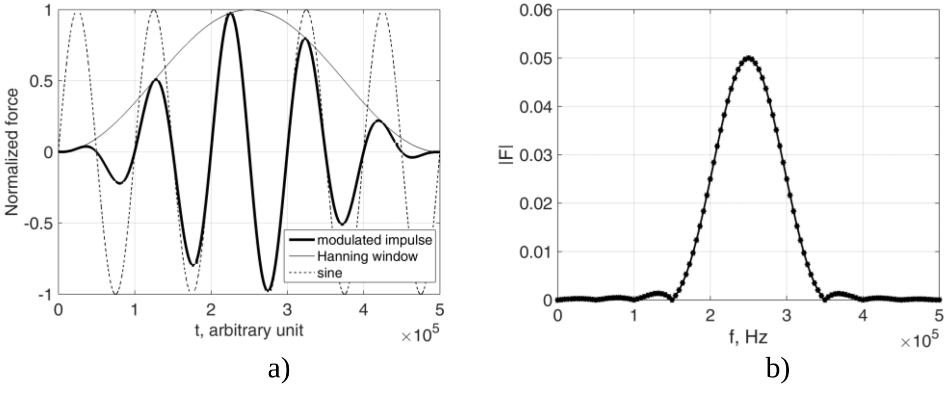

a) b)

Fig. 2.10. (a) Excitation's modulation; (b) Excitation's frequency spectrum.

(Fig. 2.11 (a)) presents the resulting displacements in the $0X$, $0Y$ and $0Z$ directions registered at the monitored point at $0.1\,m$ from the source line. Certain small wrap-around effects may be observed, such as the displacements in the $0Z$ direction at the time moment just before the arrival of the impulse. Most probably, they appear because of the artificial periodicity of the impulse due to the finite duration of the time relationship processed by FFT. Similar discrepancies are visible near to the incoming slope of the impulse in the $0Z$ direction, (Fig. 2.11 (a)). Such effects can be reduced by increasing the FFT sampling frequency and the length of zero padding.

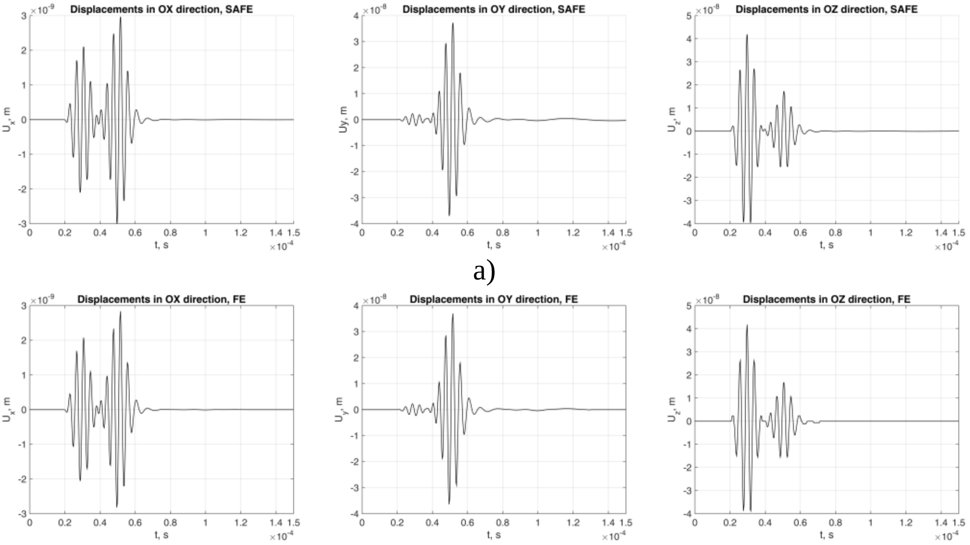

a)

b)

Fig. 2.11. Displacements of the monitored point ($z = 0.1\,m$ distance from the source in the waveguide) in the $0X, 0Y$ and $0Z$ directions obtained by using SAFEM (a) and FEM (b).

Results of the explicit simulation by means of the 3D FE model subjected to the same excitation scenario are shown (Fig. 2.11 (b)). The 3D mesh density was $4 \times 4 \times 100$ elements up to the monitored point in the $0X$, $0Y$ and $0Z$ directions. Excellent agreement of the results provided by both models was demonstrated as maximum differences of the nodal displacements calculated by both methods in the observed time-space interval did not exceed 2% for the investigated scenario. It can be noted that the SAFE approach, when compared to the conventional FE model, is capable to extract the force response invariant to time and location in the waveguide since the observed displacement field is a sum of weighted natural vectors which are calculated only once prior the numerical experiment. The complexity of FEM in the force response analysis significantly increases with the length of the waveguide (as $dofs$ increase linearly) and the duration of excitation scenario, yet, in contrast, the SAFEM complexity mainly depends on the size of the mesh on the cross-section of the waveguide, while the Eigenvalue problem is generally of $O(n^3)$ complexity, where $n = dofs$ in the cross-section.

(Fig. 2.12) shows nodal responses in the $0X$, $0Y$ and $0Z$ directions obtained by using all modes contributions (Fig. 2.12 (a)) and propagative-only modes' contributions (Fig. 2.12 (b)) to the force response at the points near the source line. The wrap-around effect is also noticeable as displacements are not equal to zero at $t = 0\ s$.

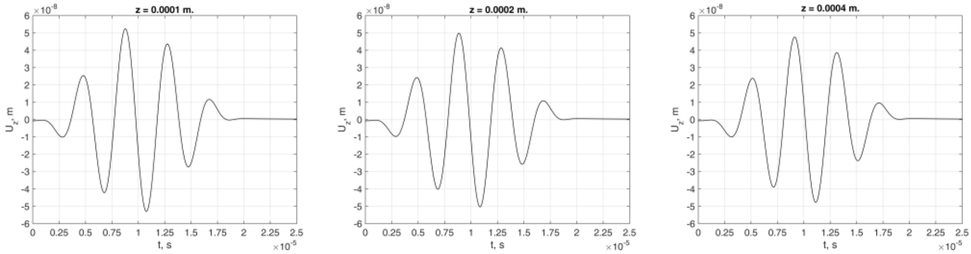

a) General excitation in the lossless waveguide.

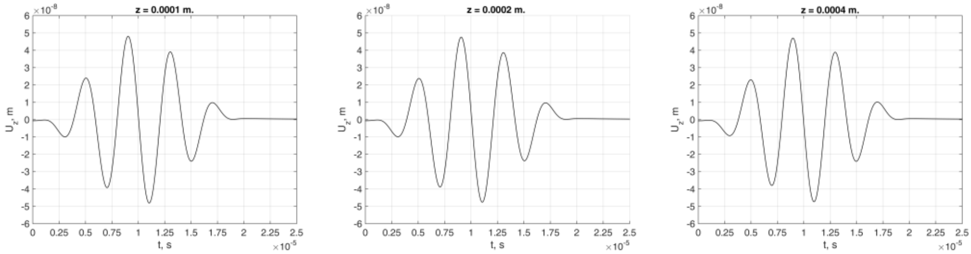

b) Propagative modes excitation in the lossless waveguide.

Fig. 2.12. The nodal response in the $0Z$ direction to (a) general and (b) propagative modes excitations at distances of $0.0001\ m$ $0.0002\ m$ and $0.0004\ m$ from the source in the $0Z$ axis.

The results imply that the evanescent and end-modes' contribution to the response decays rapidly and could be neglected in the far-field response analysis. Similar findings were reported by Weaver and Damljanovic [22].

2.4 Concluding Remarks

Despite the fact that the principles of SAFE formulation have already been known for several decades, the technique still cannot be considered as fully developed and standardized for routine simulations. Several reasons can be mentioned, such as lack of reliability when treating wave propagation solutions in environments with higher attenuation properties, the absence of approaches using direct integration techniques for obtaining transient wave pulse solutions, as well as the sophisticated interpretation of wave modes characterized by the complex space and time exponents. Also, efficient computer implementation of computational algorithms of SAFEM is important.

In this chapter, approaches to several problems related with damped wave solutions while using SAFEM were developed and implemented as software prototypes in MATLAB. Attention should be drawn to the fact that, until now, simplifications due to neglecting the complex conjugate wave numbers have been generally accepted by most authors. However, this is correct or approximately correct only for the analysis of the propagating modes in almost lossless waveguides. In case no simplifications are allowed, obtaining solutions from an Eigenvalue problem with a complex conjugate wavenumber is not straightforward anymore. It can be assumed that the conventional governing equation is accepted for propagative or lightly attenuated modes as these modes have the highest practical value.

The SAFE approach can be efficiently applied to calculate dispersion relations of the waveguide which are uniform in at least one spatial dimension in the sense of geometrical and material properties. As the SAFE approach involves the Eigenvalue problem, each modal wavenumber corresponds to a different mode. Due to the mode separation, the SAFE approach is suitable for providing dispersion relations for any wave mode of interest. As for the given wavenumber k or angular frequency ω, all the existing modes are acquired at once, yet the tracking mode of interest for varying k or ω is not straightforward; however, linear extrapolation based on mode orthogonality relations proves to be sufficient.

SAFEM enables to obtain the transient traveling-wave solutions in infinite or almost-infinite waveguide structures. The approach is based on the superposition of forced modal responses, where transient solutions are obtained via Fourier transformation. We demonstrated that the wave modes as well as the combined forced responses of the waveguides to the harmonic and general excitations during long time intervals can be obtained at a much lower cost compared to the direct simulation of a waveguide as a solid 3D FE structure. Once calculated *apriori*, the Eigenvalue solutions can be repeatedly used for acquiring different responses at any location and at arbitrary time intervals, as long as the waveguide and the localized loading pattern remain the same.

The verification of the forced damped response obtained by the SAFE approach was performed by comparing the obtained results against some test solutions acquired by the direct integration of 3D FE models. However, this does not mean anyway that 3D FEM could universally replace SAFEM in such calculations. By using the 3D FE model, only certain test situations can be created in space and time intervals of very limited magnitudes.

3 Guided Waves in Damped Waveguide

3.1.1 Rayleigh Damping in SAFE Formulation

The equation of motion using SAFE with the damping term appears as:

$$(\boldsymbol{K}_1 + ik\boldsymbol{K}_2 + k^2\boldsymbol{K}_3 - i\omega\boldsymbol{C} - \omega^2\boldsymbol{M})\overline{\boldsymbol{U}}e^{i(\mathrm{kz}-\omega t)} = \overline{\boldsymbol{F}}e^{i(\mathrm{kz}-\omega t)}. \tag{86}$$

Expanding (Eq. 86) yields:

$$\begin{gathered}\big(\boldsymbol{K}_1 + ik\boldsymbol{K}_2 + k^2\boldsymbol{K}_3 - i\omega\big(a\boldsymbol{M} + b(\boldsymbol{K}_1 + ik\boldsymbol{K}_2 + k^2\boldsymbol{K}_3)\big) - \omega^2\boldsymbol{M}\big)\cdot \\ \cdot\,\overline{\boldsymbol{U}}e^{i(\mathrm{kz}-\omega t)} = \overline{\boldsymbol{F}}e^{i(\mathrm{kz}-\omega t)}.\end{gathered} \tag{87}$$

Collecting common terms in (Eq. 87) gives us:

$$\big(\widehat{\boldsymbol{K}}_1 + ik\widehat{\boldsymbol{K}}_2 + k^2\widehat{\boldsymbol{K}}_3 - \omega^2\widehat{\boldsymbol{M}}\big)\overline{\boldsymbol{U}}e^{i(\mathrm{kz}-\omega t)} = \overline{\boldsymbol{F}}e^{i(\mathrm{kz}-\omega t)}, \tag{88}$$

where $\widehat{\boldsymbol{M}} = \left(1 + i\frac{a}{\omega}\right)\boldsymbol{M}$, $\widehat{\boldsymbol{K}}_1 = (1 - i\omega b)\boldsymbol{K}_1$, $\widehat{\boldsymbol{K}}_2 = (1 - i\omega b)\boldsymbol{K}_2$, $\widehat{\boldsymbol{K}}_3 = (1 - i\omega b)\boldsymbol{K}_3$.

As discussed previously, Rayleigh damping results in mass damping inversely proportional to the frequency and stiffness damping proportional to frequency. In this way, complex mass and stiffness matrices are introduced similarly to the Kelvin-Voigt attenuation model which involves the frequency-dependent complex stiffness matrix.

In the case of the Kelvin-Voigt model, the attenuation per distance unit increases linearly with frequency, therefore attenuation per wavelength is constant for the modes in all the frequencies.

All the solutions to homogenous (Eq. 88) are evanescent modes. Nevertheless, a mode could still be considered as traveling if an amplitude has not dropped below a reasonably small factor in relation to the initial value within the specified distance [69], [79]. One can consider a threshold for evanescent modes as an arbitrarily predefined factor a_0 by which an amplitude has dropped after traveling its wavelength. As decay of the amplitude is stored in $Im(k)\left[\frac{rad}{m}\right]$ and as the wavelength in m is $\frac{2\pi}{Re(k)}$, the threshold can be obtained as

$$-Im(k) > \frac{Re(k)}{2\pi}log_e a_0 \tag{89}$$

All the modes with wavenumbers $(Re(k) + i \cdot Im(k))$ evanescing in the positive $0Z$ direction and meeting the condition of (Eq. 89) can be retained as significant ensuring that the contribution of higher order modes is negligible and is of less interest in practical applications for further analysis. Moreover, it has been demonstrated that the calculation of the high-order wave modes which decay very rapidly with the distance is prone to poor numerical conditioning when using WFEM [97].

Analogically, homogenous (Eq. 88) can be linearized and solved as in the case of the lossless waveguide in the previously described way.

3.2 Dispersion Relations for Damped Waveguide

On the grounds of the computational experiments presented in this thesis, we investigate how the dispersion curves of different wave modes as solutions to homogenous (Eq. 88) depend on values a and b. The results are presented in (Fig. 3.1), where the cross-section mesh of the waveguide is 4×4. In the damped case, all the natural wavenumbers are complex and are therefore associated with exponentially-decaying evanescent waves. The phase velocities are obtained by using the real parts of natural wavenumbers as $c_{ph} = \frac{\omega}{Re(k)}$.

The presence of damping severely modifies the appearance of the phase velocities relationships. Due to non-zero a and b, the branches of fundamental modes tend to bend away from the Rayleigh’s wave’s velocities relationship (see Fig. 3.1(a)). Simultaneously, the attenuation of higher modes is less affected as the frequency increases, (Fig. 3.1 (b)).

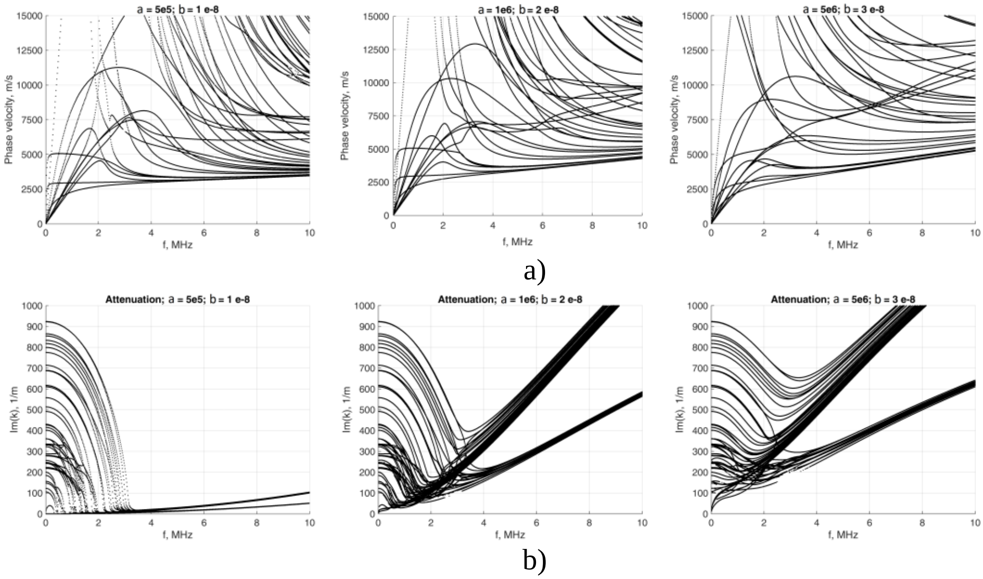

a)

b)

Fig. 3.1. a and b impact to the phase velocity (a) and attenuation (b) of the waveguide with 4×4 mesh on the cross-section.

(Fig. 3.2) shows how the phase velocities of fundamental modes are affected by severe damping. The scenario of the heaviest simulated damping clearly demonstrates a kind of behavior which may be hardly explicable. This may serve as an indication that the assumptions on which equation (Eq. 58) was based probably lack solid background, even though they had been used by many researchers before for the analysis of slightly damped structures. Thus our discovery implies the need for further research in order to revise the solutions of (Eq. 56) by fully considering the non-linear Eigenvalue problem.

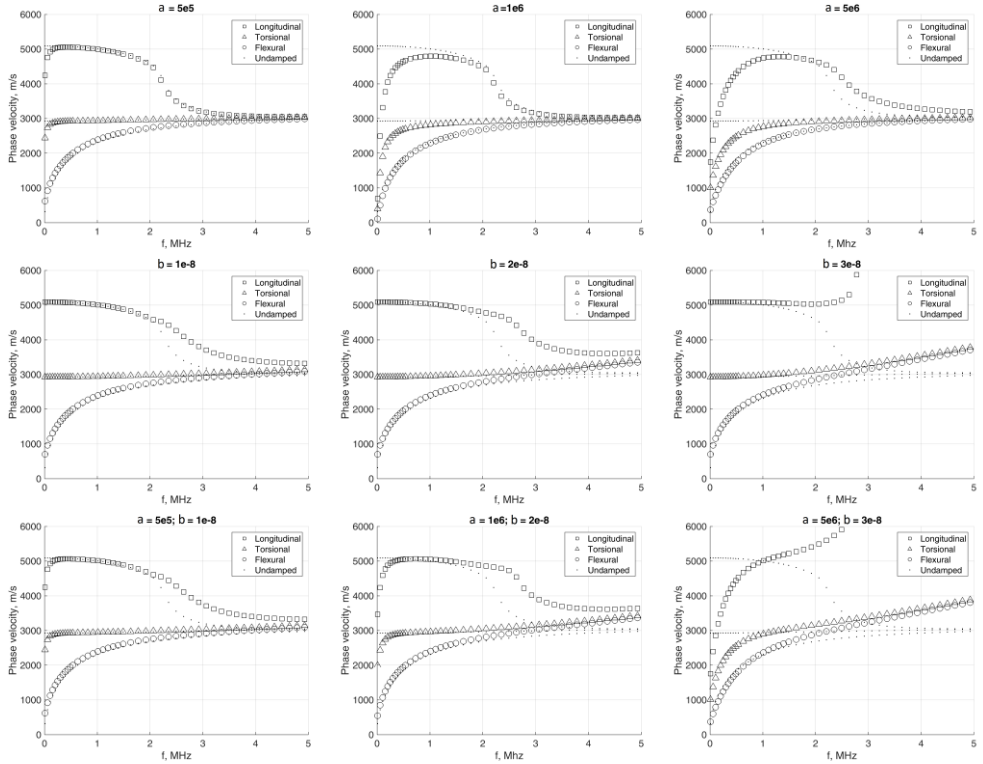

Fig. 3.2. Damping impact to the phase velocity of the fundamental modes in the waveguide with 4×4 mesh on the cross-section.

(Fig. 3.3) shows the appearance of natural wavenumbers values on the complex plane in the case of different severity of Rayleigh damping at a selected frequency $f = 1\,MHz$. As damping increases, the natural wavenumbers do not retain symmetries with respect to the $0X$ and $0Y$ axes any more.

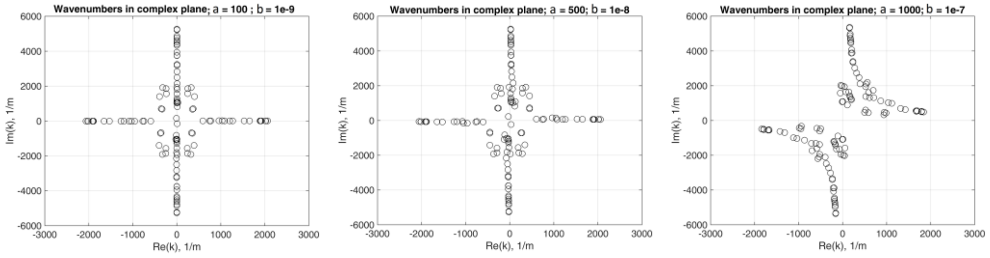

a) b) c)

Fig. 3.3. Wavenumbers in a complex plain at $f = 1\,MHz$ with the damping coefficients: (a) $a = 100$ and $b = 10^{-9}$; (b) $a = 500$ and $b = 10^{-8}$; (c) $a = 1000$ and $b = 10^{-7}$.

(Fig. 3.4) presents the response frequency spectra at the monitored point in the case of damped and undamped waveguides with the 4×4 FE cross-section. The frequency spectra describe the modal contribution in the force response. As the damping increases, the number of the dominant modes directly influencing the displacement field at the observed point decreases.

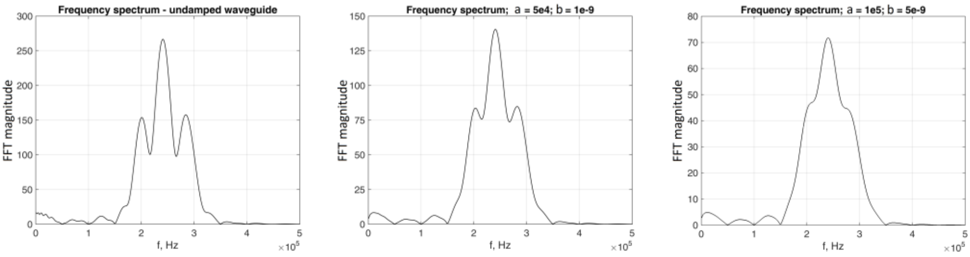

a) b) c)

Fig. 3.4. Frequency spectra of the time transient response in the $0Z$ direction of the observed point at a distance of $z = 0.1\ m$ from the forcing source in undamped (a) and damped (b), (c) waveguide.

(Fig. 3.5) demonstrates the dispersion effect which is caused by the different phase velocities of the modes excited by the loading in the lossless and damped ($a = 500$ and $b = 10^{-8}$) aluminum waveguide.

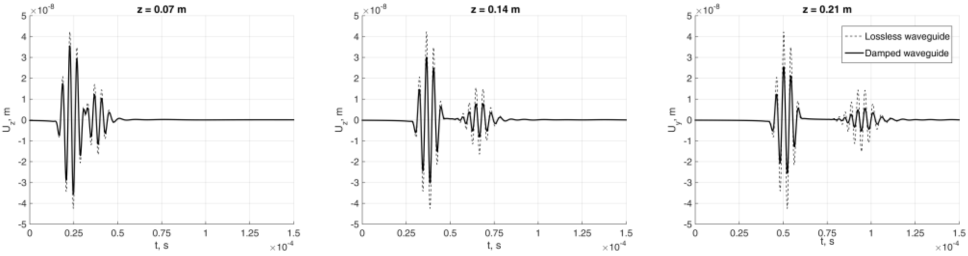

a) b) c)

Fig. 3.5. The nodal response to force in lossless and damped waveguides at distances $z\ = 0.07\ m$ (a), $z = 0.14\ m$ (b) and $z = 0.21\ m$ (c) in the $0Z$ direction from the source.

The 3D view of the waveguide structure deformed by the wave is presented in (Fig. 3.6). The displacement field is shown at time $t = 20\ \mu s$ in case of lossless and damped ($a = 500$ and $= 10^{-7}$) aluminum waveguide. Separate layers over the cross-section were drawn. A high sampling frequency was used in order to avoid aliasing in animation.

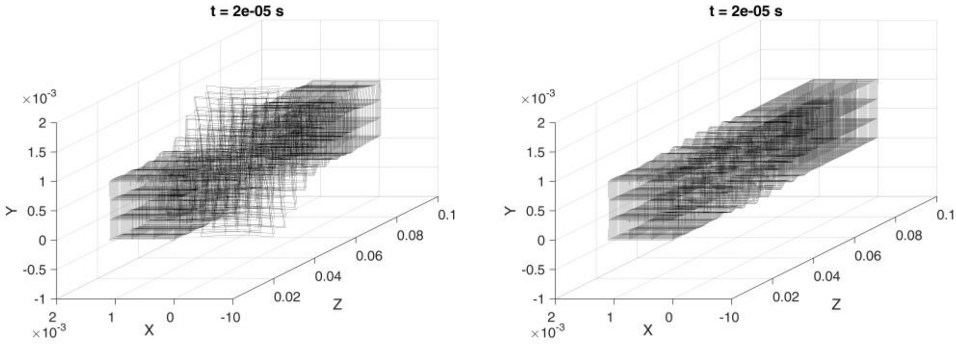

a) b)

Fig. 3.6. 3D animation representing excitation in a) lossless and b) damped ($a = 500$ and $b = 10^{-7}$) aluminum waveguide with 3×3 mesh on cross-section at $t = 20\ \mu s$.

3.3 Calculating Dispersion Relations in Damped Plate

3.3.1 Governing Equation for Damped Plate

As it was demonstrated in the previous section, it is likely that assumption $k^* = k$ leads to unsatisfactory dispersion results in the cases of extreme values of damping. We propose a retrieval of the solution to (Eq. 57) with k^* retained in the Eigenvalue problem with the added Rayleigh damping.

Without the loss of generality, let us consider the Lamb wave to be traveling in an isotropic plate of H height in the $0Z$ direction. Only the cross-section of the plate is discretized with the one-dimensional two-noded L length FE in the $0Y$ direction (Fig. 3.7). Displacement vector $\boldsymbol{u}$ in the j-th element ($j = \overline{1, N}$, where N is the number of FE in the cross-section) under harmonic wave assumption reads as:

$$\boldsymbol{u}(y, z, t)_e = \boldsymbol{N}(y)\overline{\boldsymbol{U}}_e e^{i(kz-\omega t)}, \tag{90}$$

where $\boldsymbol{N}(y) = \begin{pmatrix} 1-\frac{y}{L} & 0 & \frac{y}{L} & 0 \\ 0 & 1-\frac{y}{L} & 0 & \frac{y}{L} \end{pmatrix}$ is interpolating the form function and

$\overline{\boldsymbol{U}}_e = \begin{pmatrix} \overline{U}_{e1y} \\ \overline{U}_{e1z} \\ \overline{U}_{e2y} \\ \overline{U}_{e2z} \end{pmatrix}$ is a vector of nodal displacement within FE.

The strain vector for FE reads:

$$\boldsymbol{\varepsilon_e} = \begin{pmatrix} \boldsymbol{\varepsilon}_{yy} \\ \boldsymbol{\varepsilon}_{zz} \\ \boldsymbol{\varepsilon}_{yz} \end{pmatrix} = \begin{pmatrix} \frac{\partial \boldsymbol{u}_{ey}}{\partial y} \\ \frac{\partial \boldsymbol{u}_{ez}}{\partial z} \\ \frac{\partial \boldsymbol{u}_{ey}}{\partial z} + \frac{\partial \boldsymbol{u}_{ez}}{\partial y} \end{pmatrix}, \tag{91}$$

where $\boldsymbol{u}_{ey}$ and $\boldsymbol{u}_{ez}$ are components of displacement vector $\boldsymbol{u}_e$ in respect to the $0Y$ and $0Z$ axes, respectively.

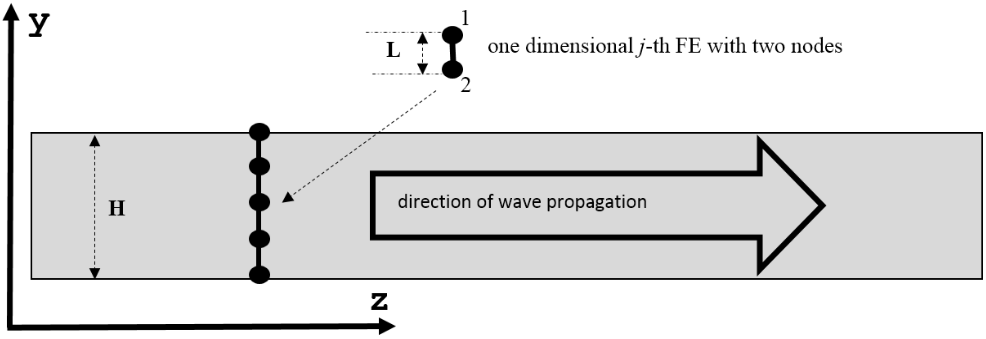

Fig. 3.7. Discretization with FE in the cross-section in a plate.

The strain vector (Eq. 91) can be rewritten as:

$$\begin{pmatrix}\boldsymbol{\varepsilon}_{yy}\\ \boldsymbol{\varepsilon}_{zz}\\ \boldsymbol{\varepsilon}_{yz}\end{pmatrix}=\begin{pmatrix}\frac{\partial}{\partial y} & 0\\ 0 & \frac{\partial}{\partial z}\\ \frac{\partial}{\partial z} & \frac{\partial}{\partial y}\end{pmatrix}\boldsymbol{N}(y)\overline{\boldsymbol{U}}_e e^{i(kz-\omega t)}=$$

$$=\begin{pmatrix}\frac{\partial}{\partial y} & 0\\ 0 & 0\\ 0 & \frac{\partial}{\partial y}\end{pmatrix}\boldsymbol{N}(y)\overline{\boldsymbol{U}}_e e^{i(kz-\omega t)}+\begin{pmatrix}0 & 0\\ 0 & \frac{\partial}{\partial z}\\ \frac{\partial}{\partial z} & 0\end{pmatrix}\boldsymbol{N}(y)\overline{\boldsymbol{U}}_e e^{i(kz-\omega t)}= \tag{92}$$

$$=\left(\begin{pmatrix}-\frac{1}{L} & 0 & \frac{1}{L} & 0\\ 0 & 0 & 0 & 0\\ 0 & -\frac{1}{L} & 0 & \frac{1}{L}\end{pmatrix}+ik\begin{pmatrix}0 & 0 & 0 & 0\\ 0 & 1-\frac{y}{L} & 0 & \frac{y}{L}\\ 1-\frac{y}{L} & 0 & \frac{y}{L} & 0\end{pmatrix}\right)\overline{\boldsymbol{U}}_e e^{i(kz-\omega t)}=$$

$$=(\boldsymbol{B}_1+ik\boldsymbol{B}_2)\overline{\boldsymbol{U}}_e e^{i(kz-\omega t)}.$$

As derived in (Eq. 53), the stiffness and mass matrices for FE can be obtained as:

$$\boldsymbol{K}_e=\int_0^L(\boldsymbol{B}_1+ik\boldsymbol{B}_2)^T\boldsymbol{D}(\boldsymbol{B}_1+ik\boldsymbol{B}_2)dy=\int_0^L{\boldsymbol{B}_1}^T\boldsymbol{D}\boldsymbol{B}_1dy+$$
$$+ik\int_0^L{\boldsymbol{B}_1}^T\boldsymbol{D}\boldsymbol{B}_2dy-ik^*\int_0^L{\boldsymbol{B}_2}^T\boldsymbol{D}\boldsymbol{B}_1dy+k^*k\int_0^L{\boldsymbol{B}_2}^T\boldsymbol{D}\boldsymbol{B}_2dy= \tag{93}$$
$$\boldsymbol{K}_{e1}+ik\boldsymbol{K}_{e2}-ik^*{\boldsymbol{K}_{e2}}^T+k^*k\boldsymbol{K}_{e3},$$
$$\boldsymbol{M}_e=\int_0^L\boldsymbol{N}(y)\rho\boldsymbol{N}(y)\,dy,$$

where elasticity matrix $\boldsymbol{D} = \frac{E(1-\nu)}{(1+\nu)(1-2\nu)} \begin{pmatrix} 1 & \frac{\nu}{1-\nu} & 0 \\ \frac{\nu}{1-\nu} & 1 & 0 \\ 0 & 0 & \frac{1-2\nu}{2(1-\nu)} \end{pmatrix}$.

The assembling procedure by overlapping the values in the stiffness and mass matrices in respect to the common nodes of FE leads to matrices $\boldsymbol{K}_1$ $\boldsymbol{K}_2$ $\boldsymbol{K}_3$ and $\boldsymbol{M}$ of the structure (cross-section). A dynamic equation $\boldsymbol{M}\ddot{\boldsymbol{u}} + \boldsymbol{C}\dot{\boldsymbol{u}} + \boldsymbol{K}\boldsymbol{u} = 0$ with damping matrix $\boldsymbol{C}$ which accounts for the viscoelasticity in the plate provides the governing equation while using the SAFE formulation. Two scenarios leading to two types of different governing equations shall be discussed. In the first one, wavenumber k of the Lamb wave is considered to be given, and angular frequency ω is to be found. In the second scenario, ω is given, and wavenumber k has to be found.

When the wavenumber of the Lamb wave is given, the governing equation can be solved for angular frequency $\omega(k)$ while introducing an equation system by reducing the order of the time derivative:

$$\begin{cases} \boldsymbol{v} = \dot{\boldsymbol{u}} \\ \boldsymbol{M}\dot{\boldsymbol{v}} + \boldsymbol{C}\boldsymbol{v} + \boldsymbol{K}\boldsymbol{u} = 0, \end{cases} \tag{94}$$

where $\dot{\boldsymbol{u}} = -i\omega\overline{\boldsymbol{U}}e^{i(kz-\omega t)} = i\overline{\boldsymbol{V}}e^{i(kz-\omega t)}$, $\ddot{\boldsymbol{u}} = -\omega^2\overline{\boldsymbol{U}}e^{i(kz-\omega t)} = -\omega\overline{\boldsymbol{V}}e^{i(kz-\omega t)}$ and $\overline{\boldsymbol{V}} = \omega\overline{\boldsymbol{U}}$.

The system (Eq. 94) can be rewritten as:

$$\begin{cases} \overline{\boldsymbol{V}} - \omega\overline{\boldsymbol{U}} = 0 \\ -\omega\boldsymbol{M}\overline{\boldsymbol{V}} - i\boldsymbol{C}\overline{\boldsymbol{V}} + \boldsymbol{K}\overline{\boldsymbol{U}} = 0, \end{cases} \tag{95}$$

The matrix form of the system can be summarized as:

$$\left(\begin{pmatrix} -i\boldsymbol{C} & \boldsymbol{K} \\ \boldsymbol{I} & \boldsymbol{0} \end{pmatrix} - \omega\begin{pmatrix} \boldsymbol{M} & \boldsymbol{0} \\ \boldsymbol{0} & \boldsymbol{I} \end{pmatrix}\right)\begin{pmatrix} \overline{\boldsymbol{V}} \\ \overline{\boldsymbol{U}} \end{pmatrix} = \boldsymbol{0}, \tag{96}$$

where $\boldsymbol{I}$ is $2(N+1) \times 2(N+1)$ dimensional identity matrix.

A canonical Eigenvalue equation for dispersion relations is obtained:

$$\left(\begin{pmatrix} -i\boldsymbol{M}^{-1}\boldsymbol{C} & \boldsymbol{M}^{-1}\boldsymbol{K} \\ \boldsymbol{I} & \boldsymbol{0} \end{pmatrix} - \omega\begin{pmatrix} \boldsymbol{I} & \boldsymbol{0} \\ \boldsymbol{0} & \boldsymbol{I} \end{pmatrix}\right)\begin{pmatrix} \overline{\boldsymbol{V}} \\ \overline{\boldsymbol{U}} \end{pmatrix} = \boldsymbol{0}. \tag{97}$$

It is a common assumption of setting $k^* = k$, i.e., a given wavenumber k is a pure real number when dealing with solutions of undamped and only propagative waves (also setting $\boldsymbol{C} = 0$). Under this assumption, the stiffness matrix within FE (Eq. 93) can be simplified:

$$\boldsymbol{K}_e = \boldsymbol{K}_{e1} + ik(\boldsymbol{K}_{e2} - {\boldsymbol{K}_{e2}}^T) + k^2\boldsymbol{K}_{e3}. \tag{98}$$

However, an accurate model of the damped waveguide ($\boldsymbol{C} \neq 0$) must retain both $k^*$and k for the waves in dissipative environment.

In the second scenario, when the angular frequency ω of the Lamb wave is given, the governing equation for wavenumber $k(\omega)$ can be derived from dynamic equation:

$$\boldsymbol{M}\ddot{\boldsymbol{u}} + \boldsymbol{C}\dot{\boldsymbol{u}} + (\boldsymbol{K}_1 + ik\boldsymbol{K}_2 - ik^*{\boldsymbol{K}_2}^T + k^*k\boldsymbol{K}_3)\boldsymbol{u} = 0, \tag{99}$$

where $\dot{\boldsymbol{u}} = -i\omega\overline{\boldsymbol{U}}e^{i(kz-\omega t)}$, $\ddot{\boldsymbol{u}} = -\omega^2\overline{\boldsymbol{U}}e^{i(kz-\omega t)}$.

The reduction of the power of the wavenumber by notation $\overline{\boldsymbol{V}} = k^*\overline{\boldsymbol{U}}$ leads to the system:

$$\begin{cases} \overline{\boldsymbol{V}} - k^*\overline{\boldsymbol{U}} = 0 \\ (-\omega^2\boldsymbol{M} - i\omega\boldsymbol{C} + \boldsymbol{K}_1)\overline{\boldsymbol{U}} + ik\boldsymbol{K}_2\overline{\boldsymbol{U}} - i{\boldsymbol{K}_2}^T\overline{\boldsymbol{V}} + k\boldsymbol{K}_3\overline{\boldsymbol{V}} = 0. \end{cases} \tag{100}$$

The matrix form of the system can be summarized as:

$$\left(\begin{pmatrix} -i{\boldsymbol{K}_2}^T & (-\omega^2\boldsymbol{M} - i\omega\boldsymbol{C} + \boldsymbol{K}_1) \\ \boldsymbol{I} & \boldsymbol{0} \end{pmatrix} + \begin{pmatrix} k\boldsymbol{K}_3 & ik\boldsymbol{K}_2 \\ \boldsymbol{0} & -k^*\boldsymbol{I} \end{pmatrix}\right)\begin{pmatrix} \overline{\boldsymbol{V}} \\ \overline{\boldsymbol{U}} \end{pmatrix} = \boldsymbol{0}. \tag{101}$$

The system (Eq. 101) is non-linear and relates the given ω with two unknowns k and its complex conjugate k^*. It is not straightforward to acquire dispersion relations $(\omega,\ k,\ k^*)$, but the iterative approach can be applied to find solutions for each mode of interest separately. At first (Eq. 101) for undamped waveguide at given ω is solved. Then, for the first approximation, real wavenumber k_0 of the propagating mode of interest is chosen. The selected k_0 is then used in (Eq. 102) to obtain updated k_{j+1}, which corresponds to the target mode. The wavenumber is updated with each j-th iteration until the solution converges. At each iteration, the Eigenvalue equation is modified to improve the solution for the tracked mode only, therefore, the procedure for the different mode must be repeated. However, input ω cannot be *apriori* exactly predefined for the damped waveguide without loss of information about the attenuation in the time domain (represented by the imaginary part of ω). Moreover, some difficulties arise in terms of assuring the convergence condition for the iterating solution and requires further analysis, which is beyond the scope of the present study.

$$\left(\begin{pmatrix} -i{\boldsymbol{K}_2}^T & (-\omega^2\boldsymbol{M} - i\omega\boldsymbol{C} + \boldsymbol{K}_1) \\ \boldsymbol{I} & \boldsymbol{0} \end{pmatrix} + k_{j+1}\begin{pmatrix} \boldsymbol{K}_3 & i\boldsymbol{K}_2 \\ \boldsymbol{0} & -\frac{k_j^*}{k_j}\boldsymbol{I} \end{pmatrix}\right)\begin{pmatrix} \overline{\boldsymbol{V}} \\ \overline{\boldsymbol{U}} \end{pmatrix} = \boldsymbol{0}. \tag{102}$$

Under the assumption that $k^* \approx k$, i.e. $Re(k) \gg Im(k)$, which is valid in the case of only light damping, (Eq. 101) is simplified to:

$$\left(\begin{pmatrix} -i{\boldsymbol{K}_2}^T & (-\omega^2\boldsymbol{M} - i\omega\boldsymbol{C} + \boldsymbol{K}_1) \\ \boldsymbol{I} & \boldsymbol{0} \end{pmatrix} + k\begin{pmatrix} \boldsymbol{K}_3 & i\boldsymbol{K}_2 \\ \boldsymbol{0} & -\boldsymbol{I} \end{pmatrix}\right)\begin{pmatrix} \overline{\boldsymbol{V}} \\ \overline{\boldsymbol{U}} \end{pmatrix} = \boldsymbol{0}. \tag{103}$$

Application of property

$$\begin{pmatrix} \boldsymbol{K}_3 & i\boldsymbol{K}_2 \\ \boldsymbol{0} & -\boldsymbol{I} \end{pmatrix}^{-1} = \begin{pmatrix} {\boldsymbol{K}_3}^{-1} & i{\boldsymbol{K}_3}^{-1}\boldsymbol{K}_2 \\ \boldsymbol{0} & -\boldsymbol{I} \end{pmatrix}$$

leads (Eq. 103) to the canonical Eigenvalue problem for dispersion relations:

$$\left(\begin{pmatrix} \boldsymbol{K}_3{}^{-1} i(\boldsymbol{K}_2 - \boldsymbol{K}_2{}^{T}) & \boldsymbol{K}_3{}^{-1}(-\omega^2\boldsymbol{M} - i\omega\boldsymbol{C} + \boldsymbol{K}_1) \\ -\boldsymbol{I} & \boldsymbol{0} \end{pmatrix} + k\begin{pmatrix} \boldsymbol{I} & \boldsymbol{0} \\ \boldsymbol{0} & \boldsymbol{I} \end{pmatrix}\right)\begin{pmatrix} \overline{\boldsymbol{V}} \\ \overline{\boldsymbol{U}} \end{pmatrix} = \boldsymbol{0}. \tag{104}$$

Under the assumption that $k^* = k$, which is valid for propagative undamped modes only, (Eq. 104) can be further simplified by omitting the damping term $-i\omega\boldsymbol{C}$.

The algorithm to acquire the dispersion relations for evanescent waves in the damped waveguide while using SAFEM is summarized in (Fig. 3.8):.

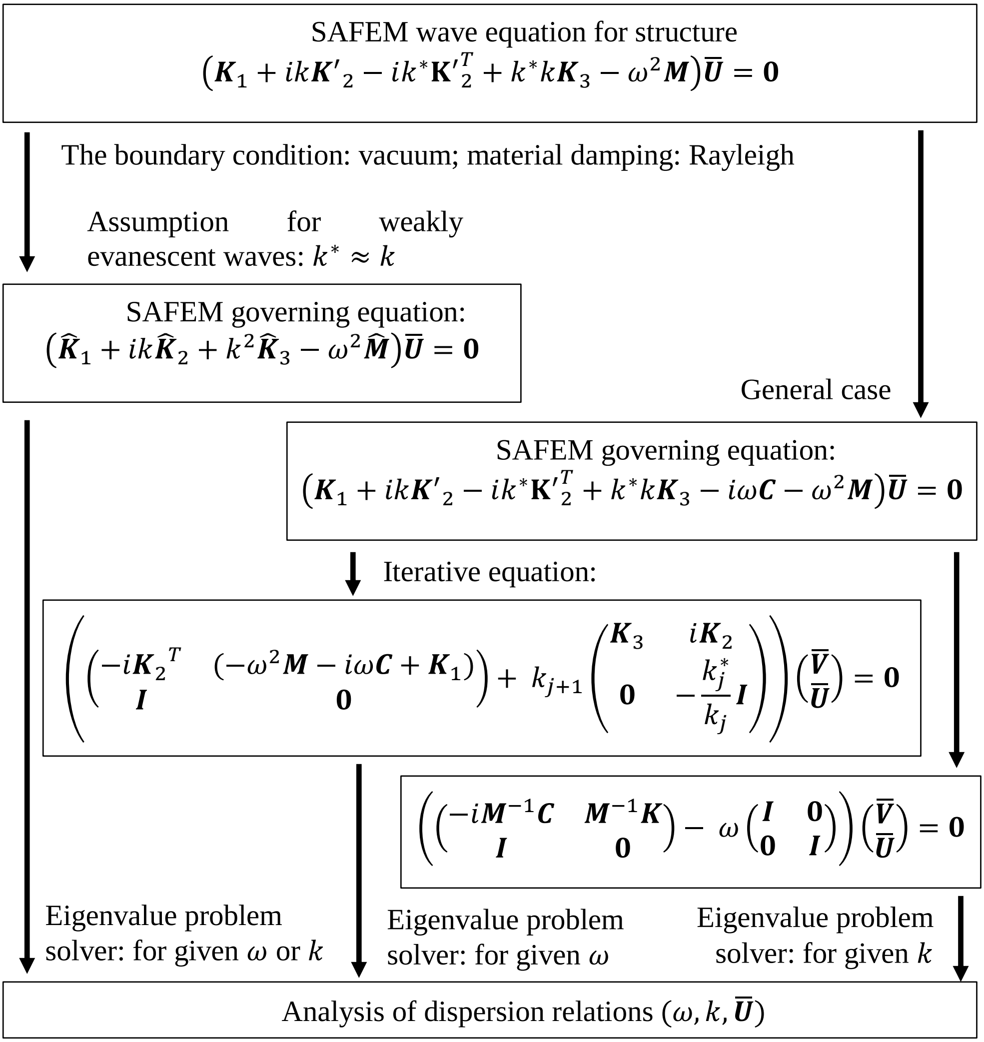

Fig. 3.8. A flowchart of the algorithm to obtain dispersion relations for evanescent waves in a damped waveguide while using SAFEM.

3.3.2 Verification of the Plate Model

As the number of FE in the structure (the cross-section of the plate) increases, the solutions to the governing equation become more accurate. In order to verify the model, the properties for an undamped ($\boldsymbol{C} = 0$) steel plate were chosen as $\rho = 7850\ kg/m^3$, $E = 2.1 \cdot 10^{11}\ Pa$, $\nu = 0.287$ and the height of the plate $H = 0.01\ m$. The convergence of solutions for the longitudinal mode acquired from (Eq. 97) at a given real wavenumber $k = 10 \cdot \frac{1}{2\pi}\,\frac{1}{m}$ (the model accepts input k in $\frac{rad}{m}$ units) due to the increasing FE in the cross-section are given in (Fig. 3.9 (a)). Already a single FE in the cross-section yields sufficient result $\omega(k)$ in low frequency when compared to the results acquired while using more FE; however, at high frequencies, the model on the single FE exhibits non-physical behavior visible in (Fig. 3.9 (b)). For example, the phase velocity of the longitudinal mode L_0 does not asymptotically approach the velocity of Rayleigh wave marked by the dotted line.

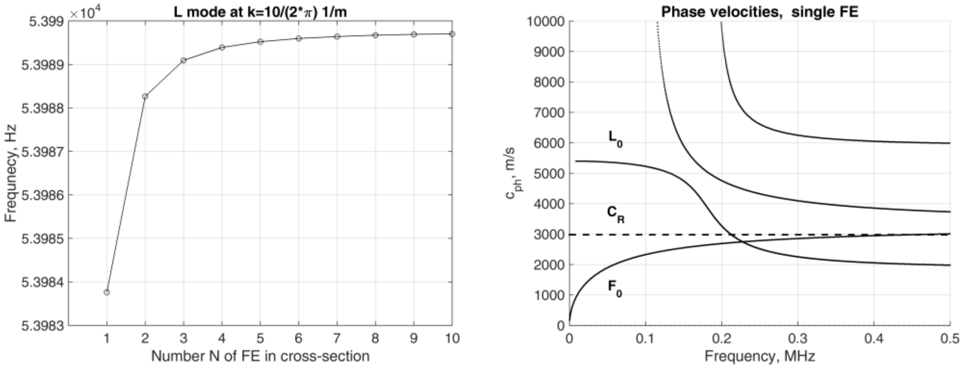

a) b)

Fig. 3.9. (a) Convergence of the longitudinal mode at $k = \frac{10}{2\pi}\,\frac{1}{m}$; (b) Phase velocities of the plate with a single FE in the cross-section.

The convergence of the solution for the longitudinal mode acquired from (Eq. 104) at given real $\omega = 10\ kHz$ due to the increasing FE in the cross-section are given in (Fig. 3.10 (a)). The same behavior of the longitudinal mode L_0 is evident in (Fig. 3.10 (b))

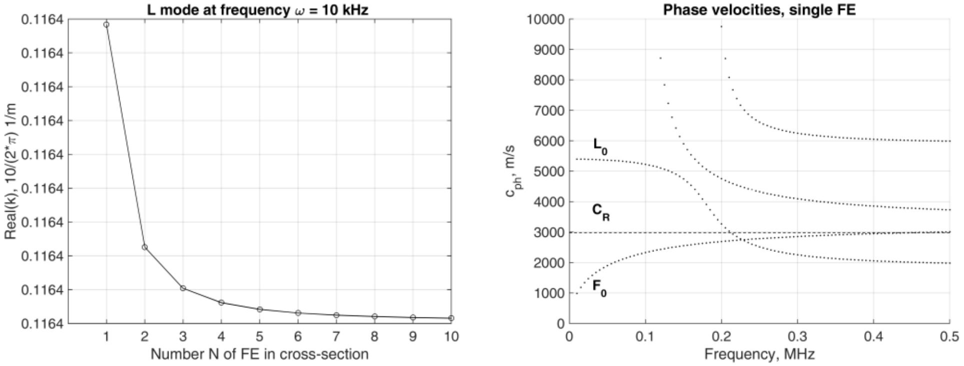

a) b)

Fig. 3.10. (a) Convergence of the longitudinal mode at real $\omega = 10\ kHz$; (b) Phase velocities of the plate with a single FE in the cross-section.

Phase velocities for a plate with $N = 10$ elements in the cross-section are provided in (Fig. 3.11).

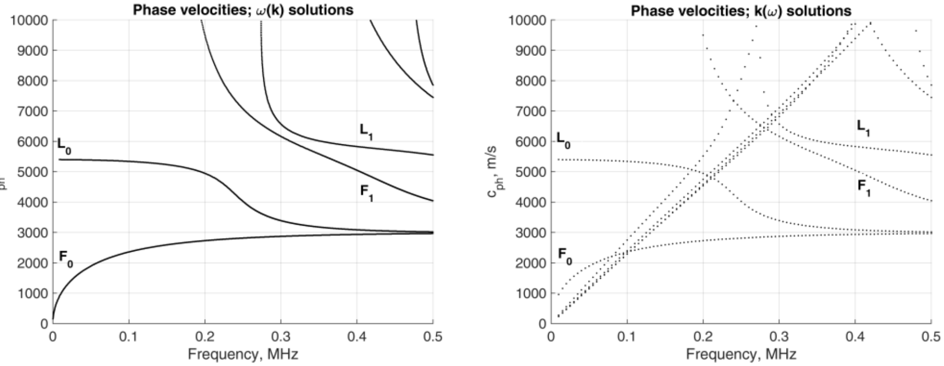

a) b)

Fig. 3.11. (a) Phase velocities acquired from $\omega(k)$ solutions; (b) Phase velocities acquired from $k(\omega)$ solutions.

The phase velocities for longitudinal L_0, L_1 and flexural F_0, F_1 modes acquired from $\omega(k)$ (Fig. 3.11 (a)) and $k(\omega)$ (Fig. 3.11 (b)) solutions excellently agree with the theoretical results for the same modes in a steel plate [98].

3.3.3 Calculating Dispersion Relations in Mass Damped Plate

Due to the absence of the research of the mass damping impact on the dispersion relations while using the SAFE formulation, the material damping in the plate model is introduced via matrix $\boldsymbol{C}$ proportional to the mass only, $\boldsymbol{C} = \alpha \boldsymbol{M}$, resulting in the complex valued mass of the plate. In the case of an undamped waveguide, the dispersion relations for propagative modes are calculated by inserting into the governing equation either the real wavenumber (then, the real $\omega(k)$ is the output), or the real angular frequency (then, the real $k(\omega)$ is the output). In the case of a damped waveguide, when free vibrations are considered, the input argument ω or k has to be a complex number and to match the given $\boldsymbol{C}$ for the structure, therefore, these inputs are unknown in advance (i.e., the imaginary parts of ω and k correspond to the attenuation of the Lamb wave in time and space and are dependent on $\boldsymbol{C}$).

The numerical exploration is performed to find $\omega(k)$ dispersion relations while using (Eq. 97). The arbitrary damping coefficient $\alpha = 11250$ is chosen. The input wavenumber is varied in respect to the real part which corresponds to the length of the Lamb wave $\lambda = \frac{1}{Re(k)}$, and the imaginary part which corresponds to the decay of the amplitude of the Lamb wave. For given $Re(k)$, successive $Im(k)$ are run from 0 to $1 \cdot 10^2 \frac{rad}{m}$ at a step of $0.2 \cdot 10^2$, i.e., the variation of attenuation is bounded only to the Lamb waves which have decayed by factor $\frac{1}{e}$ only after traveling the distance exceeding $\frac{2\pi}{1 \cdot 10^2}\, m$. At first, the impact of assumption $k^* = k$ corresponding to (Eq. 98) will be investigated. For the sake of simplicity, the dispersion relations are provided only for longitudinal mode L_0 because it has been observed that this particular mode is most sensitive to the presence of mass damping and therefore deserves detailed exploration. The numerical results expressed via phase velocity $c_{ph} = \frac{Re(\omega)}{Re(k)}$, $Re(\omega)$ versus $Re(k), Im(k)$ and $Im(\omega)$ versus $Re(k), Im(k)$ are provided in (Fig. 3.12) and (Fig. 3.13).

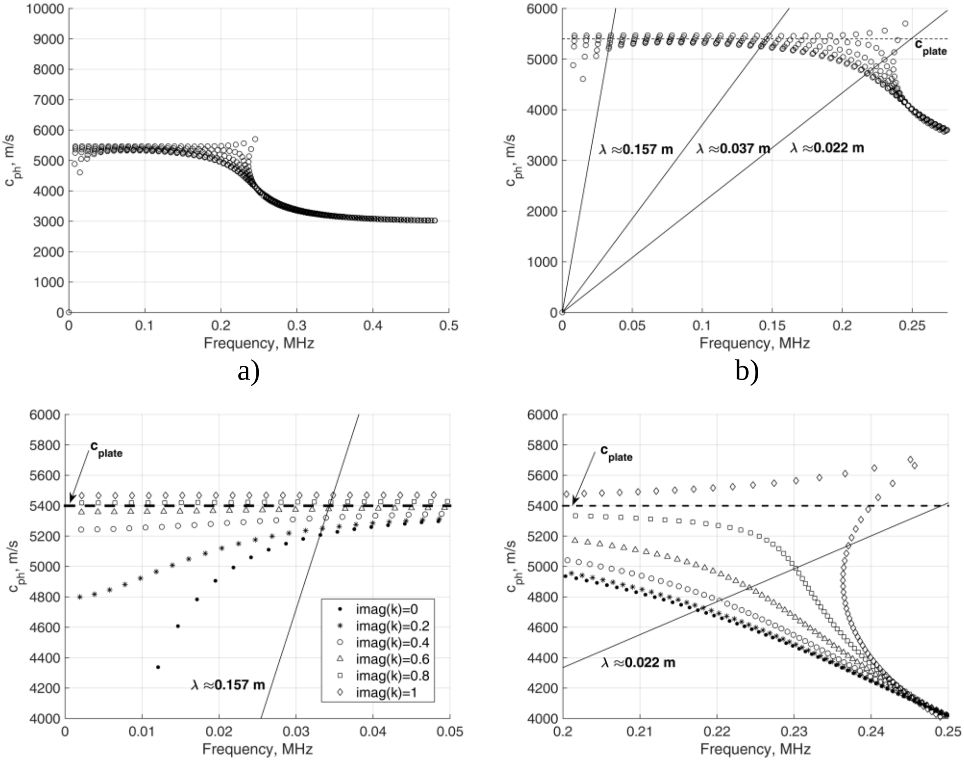

a) b)

c) d)

Fig. 3.12. (a) Phase velocities of mode L_0 due to varying $Im(k)$ of the wavenumber under assumption $k^* = k$; (b) Phase velocities of L_0 in the approximate range defined by wave lengths of $\lambda \approx 0.157\, m$ and $\lambda \approx 0.022\, m$; (c) Phase velocities of L_0 at the wave length of $\lambda \approx 0.157\, m$; (d) Phase velocities of L_0 at the wave length of $\lambda \approx 0.022\, m$.

It can be seen in (Fig. 3.12 (a)) that the imaginary part of the wavenumber has little effect to the phase velocity in the range of high frequencies. It can be noted that at the wavelengths similar to $\lambda \approx 0.157\, m$ and $\lambda \approx 0.022\, m$, the solutions of the phase velocities are sensitive to the change in the imaginary parts of the wavenumber (Fig. 3.12 (b)). The increment of $Im(k)$ in the low frequency range yields solutions to the approach and oversteps the solutions of L_0 in the undamped waveguide. Plate velocity $c_{plate} = \frac{\sqrt{E}}{\sqrt{\rho(1-\nu^2)}}$ coincides with the phase velocity of the L_0 mode at very low frequencies and can be considered as the upper physical bound of this mode across all the frequency range. A trivial bottom bound for dispersion relations are solutions with $Im(k) = 0$. The given damping matrix $\boldsymbol{C}$ can support only Lamb waves with at most $Im(k) \approx 0.7 \cdot 10^2 \frac{rad}{m}$ in low frequencies (Fig. 3.12 (c)). Unusual behavior is visible in (Fig. 3.12 (d)), it is evident that the given damping matrix $\boldsymbol{C}$ is not sufficiently big to fully support the solutions within the whole interval of $Im(k)$. So far, the phase velocities obtained from the governing equation with the assumption of $k^* = k$ alone cannot distinguish the exact dispersion relations matching the damping matrix but they rather provide a region of physically feasible solutions.

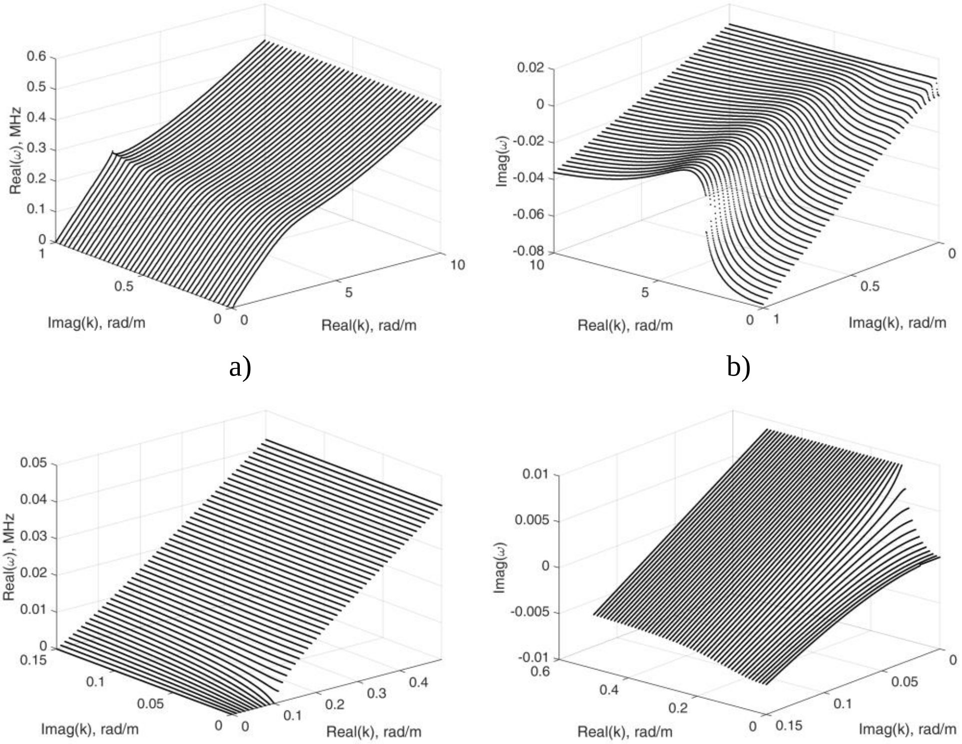

a) b)

c) d)

Fig. 3.13. (a) $Re(\omega)$ versus $Re(k)$ and $Im(k)$ under assumption $k^* = k$; (b) $Im(\omega)$ versus $Re(k)$ and $Im(k)$; (c) $Re(\omega)$ versus $Re(k)$ and $Im(k)$ at a zoomed fragment; (d) $Im(\omega)$ versus $Re(k)$ and $Im(k)$ at a zoomed fragment.

The increasing $Im(k)$ yields the dispersion curve to ‘fold’ at the wavelength of around $\lambda \approx 0.022\, m$ thus supporting our previous notes on the inadequacy of the model (Fig. 3.13 (a)). Moreover, an unfeasible area at a small $Im(k)$ in low frequencies, where a wave solution with $Re(k) > 0$ has zero frequency, is visible in (Fig. 3.13 (c)). The dispersion relations in the whole range of $Re(k)$ but linked with this area should also be excluded as non-physical. Moreover, (Fig. 3.13 (b)) reveals that the increasing $Im(k)$ results in the negative values of $Im(\omega)$, which corresponds to unattenuated waves in the time domain. However, only physically reasonable solutions of the damped wave should have $Im(\omega) > 0$. It can be seen in (Fig. 3.13 (d)) that the interval of feasible solutions gets narrower; only the waves at most up to

$Im(k) \approx 0.5 \cdot 10^2 \frac{rad}{m}$ can be considered, but the solutions at this value have $Im(\omega) \approx 0$, i.e., they are almost unattenuated-in-time waves. It is important to note that the observed variation $Im(\omega)$ of attenuation in the time domain makes mathematically possible another common assumption to set $Im(\omega) = 0$. It is widely accepted to plug in the pure real valued ω to acquire wavenumbers by using (Eq. 104), which is a direct consequence of the above mentioned assumption $k^* = k$, even when damping is present. Finally, additional assumption $Im(\omega) = 0$ allows determining the solution of only spatially damped Lamb wave. $Im(\omega) = 0$ is accepted in terms of the considered harmonic loading resulting in a nondecaying-in-time wave, which is often preferable in practical applications.

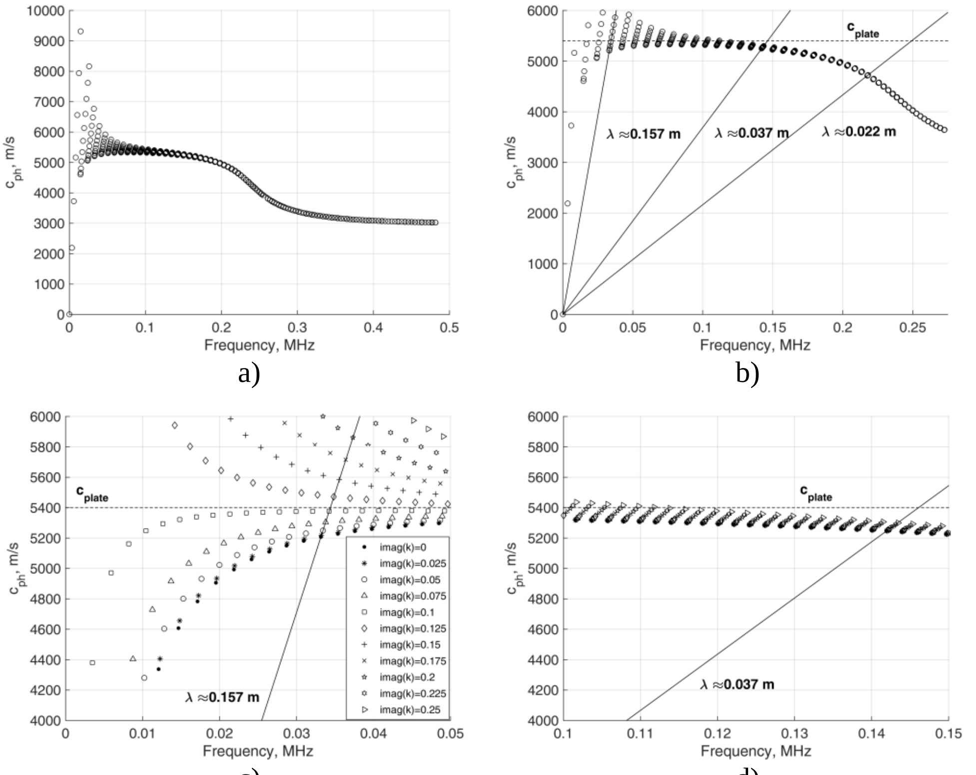

a) b)

c) d)

Fig. 3.14. (a) Phase velocities of mode L_0 due to varying $imag(k)$ of the wavenumber; (b) Phase velocities of L_0 in the approximate range defined by the wavelengths of $\lambda \approx 0.157\ m$ and $\lambda \approx 0.022\ m$; (c) Phase velocities of L_0 at a wavelength of $\lambda \approx 0.157\ m$; (d) Phase velocities of L_0 at a wavelength of $\lambda \approx 0.037\ m$.

In our further numerical exploration, the dispersion relations are calculated by discarding any of the assumptions in order to retain the accuracy of the model. $Im(k)$

is varied up to $0.25 \cdot 10^2 \frac{rad}{m}$ at a step of $0.025 \cdot 10^2$. The numerical results are expressed in a similar way in (Fig. 3.14) and (Fig. 3.15).

It can be seen in (Fig. 3.14 (a)) that the imaginary part of the wavenumber has a considerable effect to the phase velocity only in low frequencies. The phase velocities at the wave length of around $\lambda \approx 0.157\, m$ (Fig. 3.14 (b)) is inspected in detail. The solutions reach and overpass the bound c_{plate} more rapidly (Fig. 3.14 (c)). It can be seen that waves with at most $Im(k) \approx 0.1 \cdot 10^2 \frac{rad}{m}$ in low frequencies can be considered as feasible solutions. Already at a wave length of $\lambda \approx 0.037\, m$, the variation of $Im(k)$ has little effect in terms of the phase velocity (Fig. 3.14 (d)). Again, only an approximate interval for the solutions can be obtained from phase velocities.

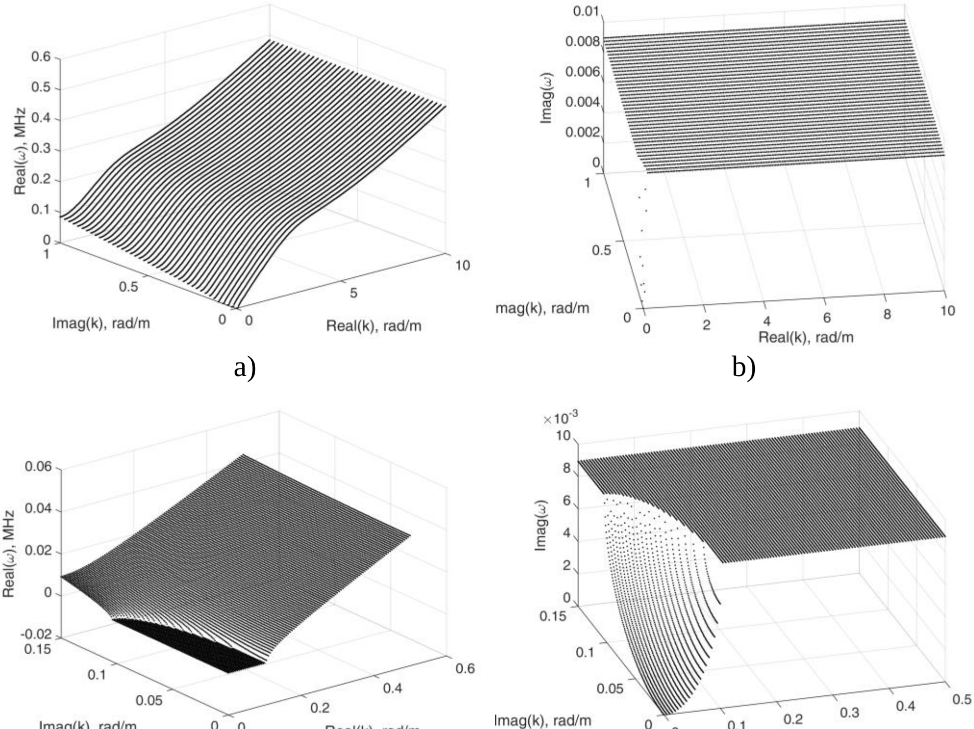

a)

b)

c)

d)

Fig. 3.15. (a) $Re(\omega)$ versus $Re(k)$ and $Im(k)$; (b) $Im(\omega)$ versus $Re(k)$ and $Im(k)$; (c) $Re(\omega)$ versus $Re(k)$ and $Im(k)$ at a zoomed fragment; (d) $Im(\omega)$ versus $Re(k)$ and $Im(k)$ at a zoomed fragment.

As $Im(k)$ increases, unphysical solutions at $Re(k) = 0$ with $Re(\omega) > 0$ appear (Fig. 3.15 (a)). An area with unfeasible solutions at $Im(\omega) = 0$ with $Re(k) > 0$ can be clearly seen in (Fig. 3.15 (c)). Dispersion curves, at least one of whose solutions is related with these regions, should not be considered. It can be seen in (Fig. 3.15 (b)) that we should expect a small region as the resulting time attenuation factor $Im(\omega)$ is constant across all the range of $Re(k)$ and $Im(k)$. The physically unfeasible area in

(Fig. 3.15 (d)) coincides with that of (Fig. 3.15 (b)). The observation of constant $Im(\omega)$ for a mode is a more intuitive consequence when compared to the previous results in (Fig. 3.13 (b)) as linear damping is considered in the model. It is therefore important to perform further investigation in terms of the use of complex ω with fixed $Im(\omega) > 0$ as an input in (Eq. 104) along with the assumption of $k^* = k$. It is observed that although $Im(\omega)$ is constant but it still differs for each mode. However, a more detailed exploration is beyond the scope of this study.

It can be observed on closer inspection in (Fig. 3.15 (c)) that on only one dispersion curve the wave does not propagate ($Re(\omega) = 0$) at only point $Re(k) = 0$ and $Im(k) \approx 0.104\ 10^2 \frac{rad}{m}$. Therefore, this curve can be considered as an exact solution $\omega(k)$ (Fig. 3.16 (a)); above this curve, nonphysical waves seem to propagate already at $Re(k) = 0$, whereas beneath this curve, nonphysical waves do not propagate even at $Re(k) > 0$. The phase velocity of the discovered solution does not exceed the upper bound c_{plate}, either (Fig. 3.16 (b)). However, more profound analysis is required to distinguish the solution in any given range of $Re(k)$ because the identification of the solution is performed in the area of only low $Re(k)$. It is important to note that the solution was identified by fixing spatial attenuation as a constant per length unit. However, for many low loss materials, bulk attenuation is approximately proportional to the frequency, therefore bulk attenuation per wavelength is constant [82] but with a different assumption $Im(\omega) = 0$.

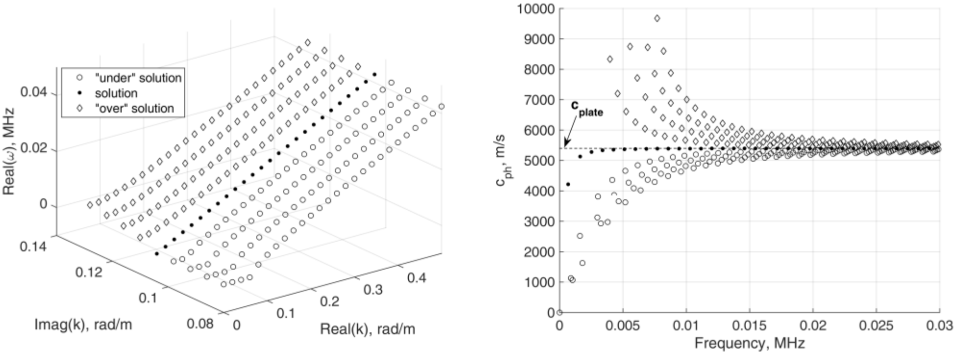

a) b)

Fig. 3.16. (a) Exact $\omega(k)$ solution of a damped plate; (b) Phase velocity of $\omega(k)$ solution.

A comparison of solutions for the longitudinal mode in the undamped waveguide, in the damped waveguide and in the damped waveguide under assumptions of $Im(\omega) = 0$ and with $k^* = k$ (when using (Eq. 104)) is provided in (Fig. 3.17). The phase velocities of the solutions significantly differ only in the low frequency range (Fig. 3.17 (a)); however, these differences diminish as the frequency increases. All the solutions asymptotically approach velocity c_R of the Rayleigh wave, which is an expected result for the Lamb waves in the high frequency range (Fig. 3.17 (b)).

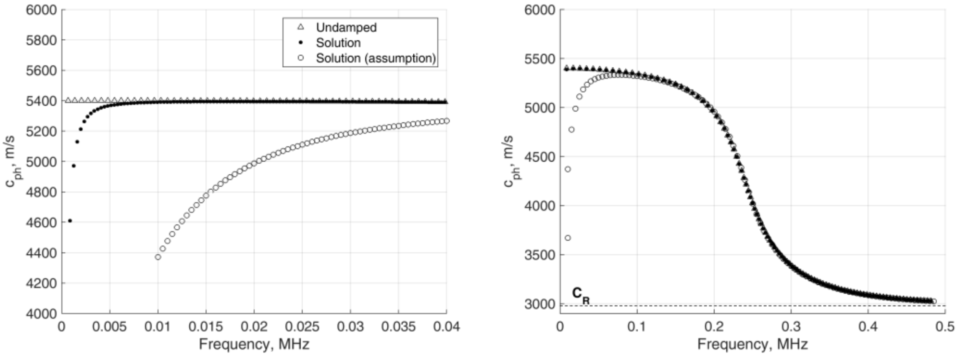

a) b)

Fig. 3.17. (a) A comparison of the phase velocities of L_0 mode in undamped waveguide, in damped waveguide and in damped waveguide under assumptions of $Im(\omega) = 0$ and with $k^* = k$; (b) Phase velocities of L_0 mode approach.

The phase velocity as the ratio $c_{ph} = \frac{Re(\omega)}{Re(k)}$ is not significantly affected by the damping in the range of high frequencies. Let us consider a decay factor to be defined as a scalar by which the wave's amplitude has dropped after traveling one length of the wave. A variation of the decay factor due to the frequency is visualized on the phase velocity of the damped L_0 mode (Fig. 3.18 (a)). A similar coefficient expressed in terms of Nepers per wavelength $\left[\frac{Np}{WaveLength}\right]$ turns out to be useful for those materials whose spatial attenuation per unit length is a linear function of the frequency while the bulk velocity is mainly constant with the frequency [82].

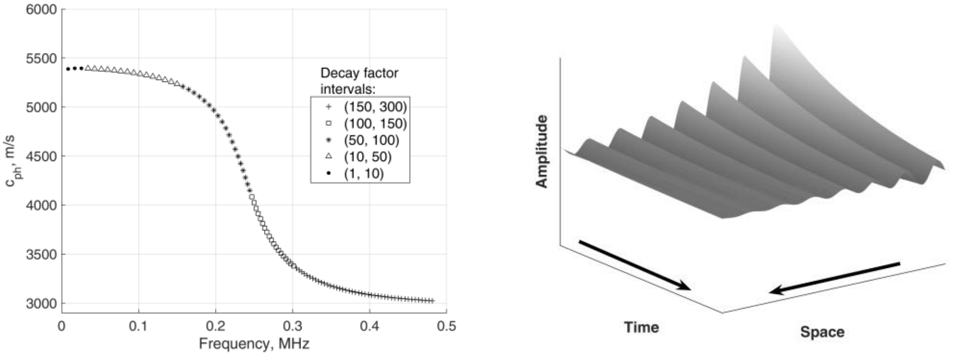

a) b)

Fig. 3.18. (a) Intervals of decay factors for the damped L_0 mode; (b) Decay of the wave in time and space.

For example, an amplitude of the mode solution at $0.3\,MHz$ would have dropped by a factor of around $\frac{1}{150}$ after the wave had traveled its own length $\lambda \approx 0.011\,m$.

In summary, $\omega(k)$ dispersion relations of the attenuated in time and space longitudinal Lamb wave were found. A solution among the possible alternatives was identified by fixing the imaginary part of the input wavenumber k in the governing Eigenvalue problem; as a consequence, the solution has constant attenuation per unit length. As a result, the attenuation in time seems to be constant for the major part of the possible solutions. Finding solution $k(\omega)$ to damped free vibrations requires further analysis. In contrast, finding $k(\omega)$ solutions to only spatially damped waves $(Im(\omega) = 0)$ seems to be only possible by setting $k^* = k$, and, in such a case, spatial attenuation is a function of frequency. Above all that, it would be useful to investigate the impact of varying damping to the dispersion solutions for more generality. A schematic representation of the wave decay in space and time domains is provided for clarity (Fig. 3.18 (b)).

3.4 Concluding Remarks

In this section, the mass-proportional Rayleigh damping of the waveguide material was introduced in SAFEM. The new aspect of this work is that the propagating wave solutions have been analyzed at a significant level of damping.

The influence of damping on the dispersion and phase-velocity curves was investigated. It was demonstrated that the approximate linearized Eigenvalue problem for the wave modes investigation is only extremely approximate in cases of severe damping. At higher values of Rayleigh damping, the dispersion relations show evident abnormalities. The erroneous results are caused by the assumption that only real wave numbers are considered, or that the complex parts of them are negligible. Physically, this means that the wave mode amplitude is not attenuated along the distance.

Therefore, the Eigenvalue problem was reformulated to include fully complex wavenumbers. As a result, all the modal solutions for the waveguide were obtained as evanescent. At a given wave frequency, the presence of the complex wavenumber leads to a non-linear Eigenvalue problem which can be solved only iteratively.

At a given wavenumber, the linearity of the Eigenproblem is retained, however, the dispersion relations have to be constructed by prescribing the values of the wavenumbers on the complex plane. So each mode is characterized by two complex exponents which characterize the behavior of the wave mode in space and time. The complex parts of the space exponent characterize the decay of the wave mode amplitude along the direction of propagation. The complex parts of the time exponent characterize the decay of the wave mode amplitude over time. The real parts of both constants represent the modal wave number and the modal wave frequency, correspondingly.

It is observed that the obtained solution of the longitudinal wave mode is less affected by the presence of mass damping applied to the waveguide when compared to the corresponding solution of the conventional approximate equation. However, further analysis would be necessary to calculate modal solutions in terms of complex wavenumbers at a given frequency.

Moreover, Rayleigh damping increases proportionally with frequency, therefore, attenuation is not bounded at high frequencies. On the other hand, more sophisticated rheological models for solids assume different material behavior over the range of frequency.

4 Leaky Guided Waves in Waveguide Immersed in Perfect Fluid

4.1 Open Waveguide

An embedded/immersed waveguide is considered to be open when the surrounding medium is unbounded. As mentioned previously, one of the main sources for attenuation is energy leakage from the waveguide to the surroundings. The modeling of the infinite surrounding leaky medium requires techniques that help to avoid unwanted reflections from the boundaries. These techniques include infinite elements, boundary integral methods, non-reflecting boundary conditions and absorbing layer techniques [46]. However, each technique is denoted by a varying efficiency of application depending on the modeling scenario. It has been demonstrated that the infinite element method only exhibits limited accuracy for elastic bulk waves (actually, as well as for guided waves) [46]. Non-reflecting boundary conditions applied in FE and the finite difference (FD) methods generally use extra variables in order to approximate the infinite surrounding media and require the development of specialist codes for FE/FD [46]. For example, the SAFEM coupled with boundary element yields a non-linear Eigenvalue problem and requires rather high computation resources [68]. The absorbing layer technique includes FE domains located at the boundaries of the investigated domain and designed to absorb the incident waves, and therefore it can be implemented in commercially available FE packages.

The two common absorbing layer techniques for the elastic bulk waves problems are the *perfectly matched layer* (PML) and the a*bsorbing layer with increasing damping* (ALID) techniques. The PML technique exploits the match of the impedances between the PML and the investigated domain. Therefore, an incident wave enters the PML without reflection and attenuates exponentially when inside the PML. Let us consider a 1D elastic wave $u(x,t) = Ue^{-i(kx-\omega t)}$ traveling towards the boundary of the investigated domain along the $0X$ axis (Fig. 4.1 (a)). The attenuation of the wave in the PML is achieved by the introduction of a complex coordinate: $x \rightarrow x(1 + i \cdot \alpha)$, where $\alpha = A \cdot x^p; (p \geq 2; A$ is constant) is an attenuation parameter varying at least quadratically with the distance within the PML. Therefore, the wave solution in the PML reads as:

$$u(x,t) = Ue^{-i(kx-ik\alpha x-\omega t)}. \qquad (105)$$

As it can be seen, the resulting wavenumber becomes a complex number and describes the evanescent wave. The layer thickness and α are the main parameters for the PML.

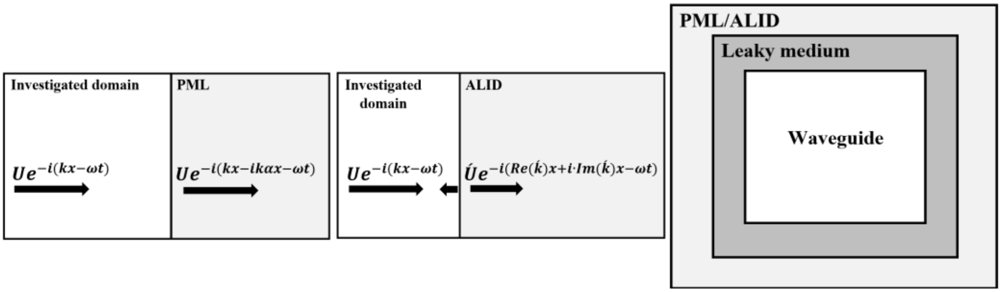

a) b) c)

Fig. 4.1. 1D elastic wave in the PML (a) and ALID (b); the cross-section of the domain consisting of the waveguide, the leaky medium and the absorbing layer (c).

The ALID has the same material properties as the adjacent medium in the investigated domain but with gradually increasing artificial damping. The viscoelasticity that accounts for material damping in the ALID can be introduced via the complex valued mass density and stiffness modulus. The resulting wavenumber is complex, and the wave solution in the ALID reads as:

$$u(x,t) = U'e^{-i(Re(k')x+i\cdot Im(k')x-\omega t)}, \tag{106}$$

$Re(k')$ describes the traveling wave within the ALID and varies with damping, however, it does not perfectly match wavenumber k in the adjacent medium in the investigated domain. This mismatch results in the reflection of the incident wave (Fig. 4.1 (b)). Additional calculations are necessary to determine the attenuation parameters for the ALID in order to minimize the reflections [46].

The main drawback of the absorbing layer techniques is that they require additional computational domain (Fig. 4.1 (d)). In cases of the perfect fluid, the infinite leaky medium surrounding the waveguide can be expressed via the exact boundary condition and is analyzed further in this study.

4.1.1 Boundary Condition for Immersed Waveguide

Let us consider a waveguide which is infinite in the OZ direction and is immersed in the infinite leaky medium as perfect non-viscous fluid which does not support shear waves (Fig. 4.2 (a)). The guided wave is assumed to be traveling in a waveguide along the OZ direction with wavenumber vector $\boldsymbol{k}_z$ (whose direction coincides with the OZ axis) at angular frequency ω. The SAFE approach represents the finite element domain Ω as a discretized cross-section of the waveguide, whereas Γ is the boundary perimeter of the cross-section (Fig. 4.2 (b)). The coordinate system of the structure is oriented in such a way that the directions of the nodal displacements – 1) u_τ tangential to the surface of the cross-section, 2) u_n normal to the surface of the cross-section, 3) u_z parallel to the waveguide axis – on the upper side of Γ respectively match the OX or OY and OZ global directions depending on the concerned side of the waveguide. Displacements u_τ and u_z would excite shear waves in the surrounding leaky medium. In case of the perfect fluid, only displacement u_n excites the longitudinal wave in the outer fluid.

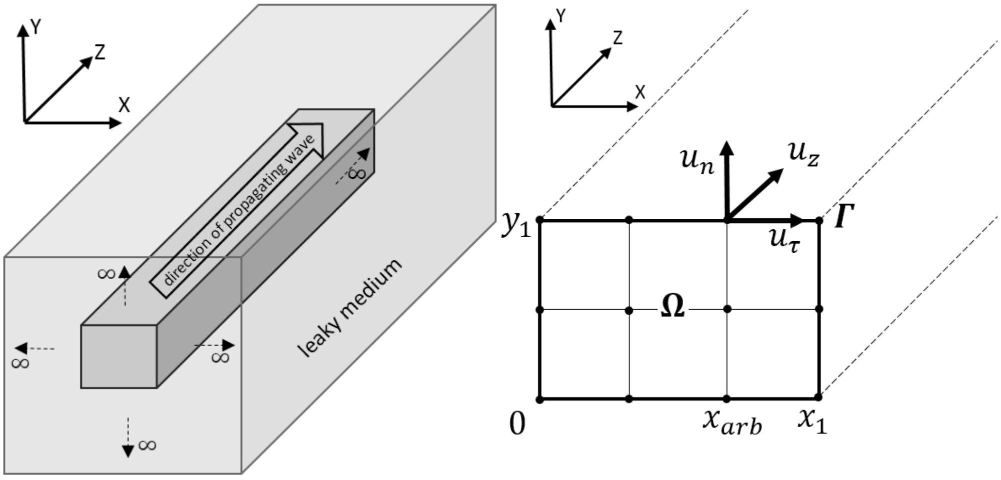

a) b)

Fig. 4.2. (a) A scheme of the immersed waveguide; (b) Discretization of the cross-section of the waveguide.

In this work, the analysis is restricted to convex cross-sections in order to avoid traveling the wavefield back to the waveguide surface.

4.1.2 One Dimensional Leaky Wave

Since the effect of the infinite surrounding medium is modeled via external traction forces acting upon the surface of the waveguide, the stress-strain relations can be retrieved from the leaky wave equation. When the wave propagation direction in the waveguide is not taken into account, it could be assumed that displacements u_n perpendicular to the cross-section change in accordance with the one-dimensional wave traveling in two adjoining infinite half spaces representing the waveguide and the fluid (Fig. 4.3 (a)). Helmholtz equation holds for both displacements in the waveguide and the fluid; particularly for a leaky medium, the displacements of the wave field are described via equation [31]:

$$\frac{\partial^2 \tilde{u}'}{\partial x'^2} + \tilde{k}'^2 \tilde{u}' = 0, \qquad (107)$$

where the tilde superscription ~ denotes the parameter correspondence to the leaky medium. The separation of variables leads to the general wave solution:

$$\tilde{u}'(\tilde{k}', x') = A(\tilde{k}')e^{i\tilde{k}'x'} + B(\tilde{k}')e^{-i\tilde{k}'x'}, \qquad (108)$$

where A and B denote the wavenumber dependable amplitudes of the backward and forward direction, respectively, with 1D waves traveling along the OX' axis. At the boundary $x' = 0$, the stresses in the waveguide and the fluid must match [69]:

$$\sigma' = \tilde{\sigma}' = \tilde{E}\frac{\partial \tilde{u}'(\tilde{k}', 0)}{\partial x'} = \tilde{E}\tilde{\varepsilon}', \qquad (109)$$

where $\tilde{E}$ denotes the elastic modulus of the leaky medium, and $\tilde{\varepsilon}$ is the strain. The elastic modulus for the longitudinal wave reads as [69]:

$$\tilde{E} = \tilde{\rho}\tilde{c}_L^2, \tag{110}$$

where $\tilde{\rho}$ denotes the mass density of the leaky medium, whereas $\tilde{c}_L$ denotes the phase velocity of the longitudinal wave in the leaky medium. The stress reads as [69]:

$$\begin{aligned}\tilde{\sigma}' = \tilde{\rho}\tilde{c}_L^2 \frac{\partial \tilde{u}'(\tilde{k}',x')}{\partial x'}\Big|_{x'=0} = i\tilde{\rho}\tilde{c}_L^2\tilde{k}'\left(A(\tilde{k}')e^{i\tilde{k}'x'} - B(\tilde{k}')e^{-i\tilde{k}'x'}\right)\Big|_{x'=0} = \\ = i\tilde{\rho}\tilde{c}_L^2\tilde{k}'\left(A(\tilde{k}') - B(\tilde{k}')\right).\end{aligned} \tag{111}$$

However, the displacements on the boundary also match [69]:

$$u'(k',0) = \tilde{u}'(\tilde{k}',0) = A(\tilde{k}') + B(\tilde{k}'). \tag{112}$$

The stress for the leaky medium can be rewritten by using (Eq. 109):

$$\begin{aligned}\tilde{\sigma}' = i\tilde{\rho}\tilde{c}_L^2\tilde{k}'\left(A(\tilde{k}') - B(\tilde{k}')\right) = i\tilde{\rho}\tilde{c}_L^2\tilde{k}'\left(2A(\tilde{k}') - \tilde{u}'(\tilde{k}',0)\right) = \\ = i\tilde{\rho}\tilde{c}_L^2\tilde{k}'\left(2A(\tilde{k}') - u'(k',0)\right)\end{aligned} \tag{113}$$

Since term $A(\tilde{k}')$ corresponds to a wave resulting from a reflection from the boundary, it can be omitted in the case of the infinite fluid. The stress on the boundary for the waveguide is finally obtained [69]:

$$\sigma' = \tilde{\sigma}' = -i\tilde{\rho}\tilde{c}_L^2\tilde{k}'u'(k',0) = -i\tilde{\rho}\tilde{c}_L\omega u'(k',0). \tag{114}$$

The assumption of continuity for the stresses at the boundary of the solid and the fluid will be applied in the three-dimensional immersed waveguide as well.

4.1.3 Traction Condition for Waveguide

When the wave propagation direction in the waveguide is taken into account, the traveling wave in the waveguide generates the pressure wave in the surrounding fluid. The wave is obtained as a superposition of two separate waves traveling in the directions of the waveguide axes OZ and u_n, respectively. The wave in the fluid is characterized by wavenumber vector $\tilde{\boldsymbol{k}}$. The norm of the wavenumber vector is related with the acoustic properties of the leaky medium as [99]:

$$\tilde{k} = \frac{\omega}{\tilde{c}_L}, \tag{115}$$

The direction of wavenumber vector $\tilde{\boldsymbol{k}}$ reads as [99]:

$$\tilde{k}^2 = \tilde{k}_L^2 + k_Z^2, \tag{116}$$

where $\tilde{k}_L$is the projection of $\tilde{\boldsymbol{k}}$ in the plane perpendicular to the cross-section of the waveguide, $\tilde{k}_Z$ is the projection of $\tilde{\boldsymbol{k}}$ on the axis OZ and coincides with the wavenumber of the traveling wave in the waveguide, i.e., $\tilde{k}_Z = k_Z$ (Fig. 4.3 (b)).

When the phase velocity of a guided wave is considerably higher than the longitudinal bulk wave in the fluid, the energy of the guided wave leaks into the leaky medium with angle θ (Fig. 4.3 (b)) determined by Snell's law [100]:

$$\sin(\theta) = \frac{c_{ph}}{\tilde{c}_{ph}}, \tag{117}$$

where c_{ph} and $\tilde{c}_{ph}$ are the phase velocities of the guided wave and the leaky wave, respectively.

When the phase velocity of the waveguide is many times larger than that of the leaky wave $c_{ph} \gg \tilde{c}_{ph}$, θ approaches zero, i.e., the leaky wave tends to travel along the OY axis. Under these circumstances, the surrounding medium can be regarded as a solid which does not support shear waves. A 1D dashpot boundary condition could be proposed to approximate the effect of this type of the surrounding solid, particularly in high frequencies [70]. Parameter R_c defined as the ratio of acoustic impedances of the embedded waveguide and the leaky medium can be used to estimate the effect of the surrounding medium [70]:

$$R_c = \frac{c_{ph}\,\rho}{\tilde{c}_{ph}\,\tilde{\rho}} = \sqrt{\frac{G\rho}{\tilde{G}\tilde{\rho}}}, \qquad (118)$$

where G is the shear modulus.

When $R_c \gg 1$, i.e., when the materials are very different, the major part of the energy of the guided wave reflects at the waveguide's interface, therefore, the damping effect due to the leaky wave is relatively small. When $R_c \approx 1$, the angle of reflection at the interface of the waveguide approaches zero, and the structure can no longer be considered as an embedded waveguide. It was demonstrated that, for $R_c \geq 4$, a technique of the FE absorbing region that accounts for the surrounding medium (as described in [64]) can be assumed to converge to more accurate results [70]. It was also shown, that, at the extreme case, when $R_c = 2$, both approaches of the dashpot boundary condition and the FE absorbing region fail to produce very reliable results. However, in order to overcome proximities, the boundary condition for the waveguide will account for the exact direction of the leaky waves.

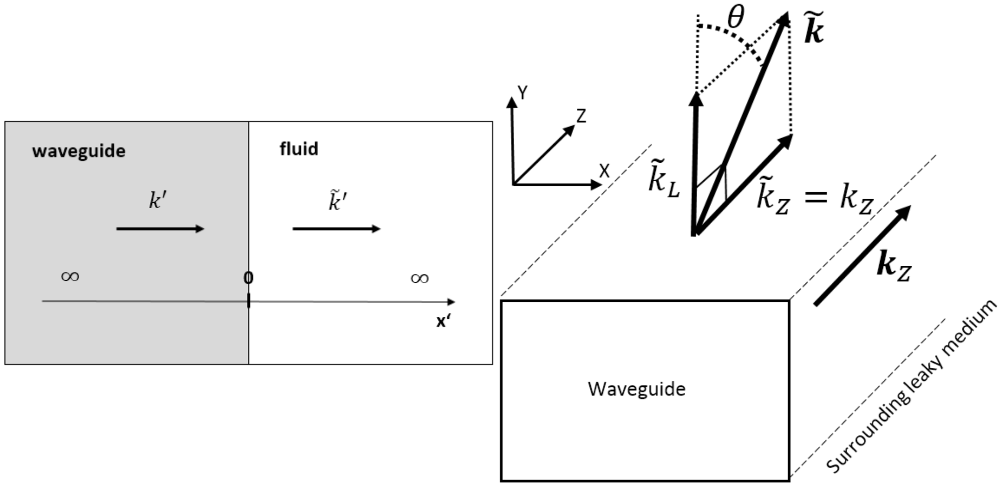

a) b)

Fig. 4.3. (a) A one-dimensional wave traveling in infinite half spaces; (b) Wavenumbers at the interface of the waveguide and the fluid.

Let $\Gamma 1$ be the segment of the cross-section perimeter determined between two points $(0, y1)$ and $(x1, y1)$ (Fig. 4.2 b). The displacement field in the fluid at arbitrary x_{arb} position $\Gamma 1$ after omitting the temporal term $e^{-i\omega t}$ is a two-dimensional wave [99]:

$$\tilde{\boldsymbol{u}}_{fluid1} = \begin{pmatrix} \tilde{u}_y \\ \tilde{u}_z \end{pmatrix} = \begin{pmatrix} \tilde{k}_L \\ k_z \end{pmatrix} a_L e^{i(\tilde{k}_L y + k_Z z)}, \tag{119}$$

where a_L is an arbitrary scalar. As in the case of a one-dimensional wave (Eq. 108), the amplitude depends on the wavenumbers of the added waves. Since an excited wave in the leaky medium is longitudinal and perpendicular to $\Gamma 1$, displacements equal to $\tilde{u}_x = 0$. The displacement field for the leaky wave on boundary $\Gamma 1$ at $z = 0$ and x_{arb} reads:

$$\boldsymbol{u}_{\Gamma 1} = \begin{pmatrix} u_n \\ u_z \end{pmatrix} = \begin{pmatrix} \tilde{u}_n \\ \tilde{u}_z \end{pmatrix} = \begin{pmatrix} \tilde{k}_L \\ k_z \end{pmatrix} a_L e^{i\tilde{k}_L y_1}. \tag{120}$$

The scalar a_L can be expressed as [99]:

$$a_L = \frac{u_n}{\tilde{k}_L} e^{-i\tilde{k}_L y_1}. \tag{121}$$

(Eq. 119) can be rewritten as [99]:

$$\tilde{\boldsymbol{u}}_{fluid1} = \begin{pmatrix} \tilde{u}_y \\ \tilde{u}_z \end{pmatrix} = \begin{pmatrix} 1 \\ \frac{k_z}{\tilde{k}_L} \end{pmatrix} u_n e^{i(\tilde{k}_L (y - y_1) + k_Z z)}. \tag{122}$$

The strain vector for the leaky wave in a fluid affected by boundary $\Gamma 1$ reads as:

$$\begin{aligned} \tilde{\boldsymbol{\varepsilon}}_{fluid1} &= \left(\mathbf{L}_y \frac{\partial}{\partial y} + \mathbf{L}_z \frac{\partial}{\partial z}\right) \tilde{\boldsymbol{u}}_{fluid1} = \\ &= \left(i\tilde{k}_L \mathbf{L}_y + ik_Z \mathbf{L}_z\right) \begin{pmatrix} 1 \\ \frac{k_Z}{\tilde{k}_L} \end{pmatrix} u_n e^{i(\tilde{k}_L (y - y_1) + k_Z z)}, \end{aligned} \tag{123}$$

where $\boldsymbol{L}_y = \begin{pmatrix} 1 & 0 \\ 0 & 0 \\ 0 & 1 \end{pmatrix}$ and $\boldsymbol{L}_z = \begin{pmatrix} 0 & 0 \\ 0 & 1 \\ 1 & 0 \end{pmatrix}$. The strain vector for the leaky wave on boundary $\Gamma 1$ is:

$$\tilde{\boldsymbol{\varepsilon}}_{\Gamma 1} = \begin{pmatrix} \tilde{\varepsilon}_{yy} \\ \tilde{\varepsilon}_{zz} \\ \tilde{\gamma}_{yz} \end{pmatrix} = \left(i\tilde{k}_L \mathbf{L}_y + ik_Z \mathbf{L}_z\right) \begin{pmatrix} 1 \\ \frac{k_Z}{\tilde{k}_L} \end{pmatrix} u_n e^{ik_Z z}. \tag{124}$$

However, the stress on boundary $\Gamma 1$ is present only in the direction of displacements u_n and can be expressed similarly to (Eq. 114), where $\tilde{k}'$ wavenumber is replaced with projection $\tilde{k}_L = \sqrt{\tilde{k}^2 - k_Z^2}$ of the wavenumber vector $\tilde{\boldsymbol{k}}$:

$$\tilde{\boldsymbol{\sigma}}_{\Gamma1} = \begin{pmatrix} \tilde{\sigma}_{yy\Gamma1} \\ \tilde{\sigma}_{zz\Gamma1} \\ \tilde{\tau}_{zy\Gamma1} \end{pmatrix} = \begin{pmatrix} \tilde{\sigma}_{yy\Gamma1} \\ 0 \\ 0 \end{pmatrix}, \tag{125}$$

where $\tilde{\sigma}_{yy\Gamma1} = -i\tilde{\rho}\tilde{c}_L\omega\tilde{u}\left(\tilde{k}_L, y = y1, z\right) = -i\tilde{\rho}\frac{\omega}{\sqrt{\tilde{k}^2-k_Z^2}}\omega\tilde{u}_y = -i\tilde{\rho}\frac{\omega^2}{\tilde{k}_L}\tilde{u}_y$. By using (Eq. 70), $\tilde{\sigma}_{yy\Gamma1}$ can be rewritten as:

$$\tilde{\sigma}_{yy\Gamma1} = -i\tilde{\rho}\frac{\omega^2}{\tilde{k}_L}\tilde{u}_y = -i\tilde{\rho}\frac{\omega^2}{\tilde{k}_L}\tilde{u}_{\mathrm{n}}e^{ik_Z z} = -i\tilde{\rho}\frac{\omega^2}{\tilde{k}_L}u_n e^{ik_Z z}. \tag{126}$$

The stress on boundary Γ1 in the fluid corresponds to the surface traction condition for the waveguide:

$$\boldsymbol{t}_{\Gamma1} = \begin{pmatrix} t_n \\ t_\tau \\ t_z \end{pmatrix} = \begin{pmatrix} \tilde{\sigma}_{yy\Gamma1} \\ 0 \\ 0 \end{pmatrix}. \tag{127}$$

It can be noted that traction, as well as stress, in the fluid along the OZ direction is governed by the harmonic wave. If we let x_{arb} coincide with the FE nodes in respect of the OX axis, it yields us the waveguide surface traction caused by a fluid:

$$\boldsymbol{t}_{\Gamma1} = \begin{pmatrix} t_n \\ t_\tau \\ t_z \end{pmatrix} = \boldsymbol{N}\boldsymbol{T}_j e^{ik_Z z}, \tag{128}$$

where $\boldsymbol{N}$ is a shape function with constraint $y = y1, j = \overline{1,m}$, $(m-1)$ is the number of FE along boundary Γ1, $\boldsymbol{T}_j$ is the nodal external traction vector at the waveguide boundary as:

$$\boldsymbol{T}_j = \begin{pmatrix} T_n \\ 0 \\ 0 \end{pmatrix}_j = -i\frac{\omega^2}{\tilde{k}_L}\begin{pmatrix} \tilde{\rho} & 0 & 0 \\ 0 & 0 & 0 \\ 0 & 0 & 0 \end{pmatrix}\begin{pmatrix} u_n \\ u_\tau \\ u_z \end{pmatrix}_j = -i\frac{\omega^2}{\tilde{k}_L}\boldsymbol{C}\begin{pmatrix} u_n \\ u_\tau \\ u_z \end{pmatrix}_j. \tag{129}$$

Similarly to the one-dimensional case (as shown in Eq. 114), the surface traction for the waveguide (Eq. 129) is a function of acoustic properties of the surrounding leaky medium, the angular frequency of the traveling wave and the displacements at the boundary of the solid and the fluid.

4.2 Obtaining Dispersion Solutions

4.2.1 Nonlinear Eigenvalue Problem

The external boundary condition must be included into the general Eigenvalue problem as [99]:

$$(\boldsymbol{K}_1 + ik_Z\boldsymbol{K}_2 + k_Z^2\boldsymbol{K}_3 - \omega^2\boldsymbol{M})\boldsymbol{u} = \boldsymbol{F}_{fluid} + \boldsymbol{F}_{loading}, \tag{130}$$

where $\boldsymbol{F}_{fluid}$ is the nodal force vector due to the fluid traction condition. $\boldsymbol{F}_{loading}$ is the nodal force vector due to the external dynamic loading as long as the forced wave response is concerned. If our case is $\boldsymbol{F}_{loading} = \boldsymbol{0}$, (Eq. 130) is treated as an

Eigenvalue problem whose solution provides us with the dispersion relations for a waveguide immersed in the fluid.

$\boldsymbol{F}_{fluid}$ summarizes the external traction caused by fluid loading:

$$\boldsymbol{F}_{fluid} = i\frac{\omega^2}{\tilde{k}_L}\boldsymbol{Q}\boldsymbol{u} = i\frac{\omega^2}{\tilde{k}_L}\boldsymbol{Q}\bar{\mathbf{U}}e^{ik_Z z}, \qquad (131)$$

where coefficient matrix $\boldsymbol{Q}$ characterizes the distribution of fluid tractions among the nodes on surface perimeter Γ as [70]:

$$\boldsymbol{Q} = \int_{s\in\Gamma}(\boldsymbol{N}(s))^T\boldsymbol{C}\boldsymbol{N}(s)ds, \qquad (132)$$

where $\boldsymbol{N}(s)$ is a one-dimensional shape function used to interpolate the x and y coordinates on Γ, s is a circumferential integral coordinate running along Γ.

Finally, the governing equation for the immersed waveguides is obtained as a nonlinear Eigenvalue problem:

$$\left(\boldsymbol{K}_1 + ik_Z\boldsymbol{K}_2 + k_Z^2\boldsymbol{K}_3 - \omega^2\boldsymbol{M} - i\frac{\omega^2}{\tilde{k}_L}\boldsymbol{Q}\right)\bar{\boldsymbol{U}} = \boldsymbol{0}. \qquad (133)$$

4.2.2 Solving Eigenvalue Problem

In this study, (eq. 133) is solved by extending the technique proposed in paper [99] to a three-dimensional waveguide. A two-stage procedure of the algebraic transformation and linearization of (Eq. 133) is employed. The m-th wavemode $(k_{Zm}, \tilde{k}_{Lm}, \boldsymbol{\varphi}_m)$ must satisfy the following equation:

$$\left(\boldsymbol{K}_1 + ik_{Zm}\boldsymbol{K}_2 + k_{Zm}^2\boldsymbol{K}_3 - \omega^2\boldsymbol{M} - i\frac{\omega^2}{\tilde{k}_{Lm}}\boldsymbol{Q}\right)\boldsymbol{\varphi}_m = \boldsymbol{0}. \qquad (134)$$

The further transformation is based on the symmetry of wave solutions with respect to the XOY plane. Identical waves propagating in the positive and negative OZ directions are described by (Eq. 134). In order to exploit this feature, we shall split natural vector $\boldsymbol{\varphi}_m$ with respect to displacements in the directions of OZ and others than OZ:

$$\boldsymbol{\varphi}_m = \begin{pmatrix}\boldsymbol{\varphi}_{om}\\ \boldsymbol{\varphi}_{zm}\end{pmatrix}. \qquad (135)$$

For the convenience of the post-processing of modal results, natural vector $\boldsymbol{\varphi}_m$ is split by separating the nodal degrees of freedom (*dof*) with respect to displacements u_n on Γ that correspond to the longitudinal wave in the fluid (denoted as L), displacements u_τ on Γ that would excite the shear wave (represented by S), displacements u_z along the OZ axis on the entire cross-section (written as z) and introduced displacements u_C in the core of the cross-section (marked by C) (Fig. 4.4).

The preferable reordering of *dof* could be summarized as:

$$\boldsymbol{\varphi}_m = \begin{pmatrix}\boldsymbol{\varphi}_{om}\\ \boldsymbol{\varphi}_{zm}\end{pmatrix} = \begin{pmatrix}\boldsymbol{\varphi}_{Lm}\\ \boldsymbol{\varphi}_{Sm}\\ \boldsymbol{\varphi}_{Cm}\\ \boldsymbol{\varphi}_{zm}\end{pmatrix}. \qquad (136)$$

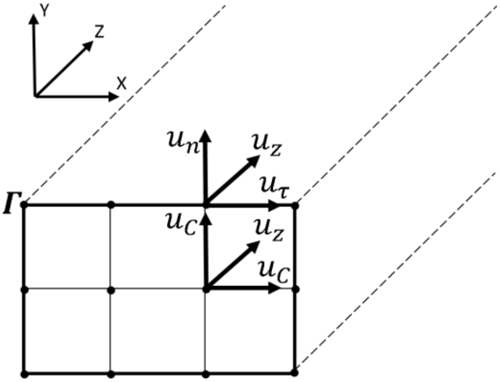

Fig. 4.4. A schematic classification of nodal displacements in the cross-section.

The matrices in (Eq. 134) are divided into block components in accordance with (Eq. 136) as

$$\begin{aligned}&((\boldsymbol{K}_{1L}\quad \boldsymbol{K}_{1S}\quad \boldsymbol{K}_{1C}\quad \boldsymbol{K}_{1Z})+ik_{Zm}(\mathbf{K}_{2L}\quad \boldsymbol{K}_{2S}\quad \boldsymbol{K}_{2C}\quad \boldsymbol{K}_{2Z})+\\&+k_{Zm}^2(\boldsymbol{K}_{3L}\quad \boldsymbol{K}_{3S}\quad \boldsymbol{K}_{3C}\quad \boldsymbol{K}_{3Z})-\omega^2(\boldsymbol{M}_L\quad \boldsymbol{M}_S\quad \boldsymbol{M}_C\quad \boldsymbol{M}_Z)-\\&-i\frac{\omega^2}{\tilde{k}_{Lm}}\big((\boldsymbol{Q}_L\quad \boldsymbol{Q}_S\quad \boldsymbol{Q}_C\quad \boldsymbol{Q}_Z)\big))\begin{pmatrix}\boldsymbol{\varphi}_{Lm}\\ \boldsymbol{\varphi}_{Sm}\\ \boldsymbol{\varphi}_{Cm}\\ \boldsymbol{\varphi}_{zm}\end{pmatrix}=0.\end{aligned}\tag{137}$$

A symmetrical solution with respect to the OZ direction means that the displacement distribution with the $-k_{zm}$ wavenumber and the corresponding natural vector $\begin{pmatrix}\boldsymbol{\varphi}_{om}\\ -\boldsymbol{\varphi}_{zm}\end{pmatrix}$ also satisfies the following equation:

$$\begin{aligned}&((\boldsymbol{K}_{1L}\quad \mathbf{K}_{1S}\quad \boldsymbol{K}_{1C}\quad \boldsymbol{K}_{1Z})-ik_{Zm}(\boldsymbol{K}_{2L}\quad \boldsymbol{K}_{2S}\quad \boldsymbol{K}_{2C}\quad \boldsymbol{K}_{2Z})+\\&+k_{Zm}^2(\boldsymbol{K}_{3L}\quad \boldsymbol{K}_{3S}\quad \boldsymbol{K}_{3C}\quad \boldsymbol{K}_{3Z})-\omega^2(\boldsymbol{M}_L\quad \boldsymbol{M}_S\quad \boldsymbol{M}_C\quad \boldsymbol{M}_Z)-\\&-i\frac{\omega^2}{\tilde{k}_{Lm}}\big((\boldsymbol{Q}_L\quad \boldsymbol{Q}_S\quad \boldsymbol{Q}_C\quad \boldsymbol{Q}_Z)\big))\begin{pmatrix}\boldsymbol{\varphi}_{Lm}\\ \boldsymbol{\varphi}_{Sm}\\ \boldsymbol{\varphi}_{Cm}\\ -\boldsymbol{\varphi}_{zm}\end{pmatrix}=\mathbf{0}.\end{aligned}\tag{138}$$

The linear combination $\frac{\left((Eq.137)+(Eq.138)\right)}{2}+k_{Zm}\frac{\left((Eq.137)-(Eq.138\,)\right)}{2}$ [99] provides the Eigenvalue problem as:

$$\begin{aligned}&((\boldsymbol{K}_{1L}\quad \boldsymbol{K}_{1S}\quad \boldsymbol{K}_{1C}\quad \boldsymbol{K}_{1Z})+i(\mathbf{0}\quad \mathbf{0}\quad \mathbf{0}\quad \boldsymbol{K}_{2Z})-\omega^2(\boldsymbol{M}_L\quad \mathbf{M}_S\quad \boldsymbol{M}_C\quad \boldsymbol{M}_Z)\\&+ik_{Zm}^2(\boldsymbol{K}_{2L}\quad \boldsymbol{K}_{2S}\quad \boldsymbol{K}_{2C}\quad \mathbf{0})+k_{Zm}^2(\boldsymbol{K}_{3L}\quad \boldsymbol{K}_{3S}\quad \boldsymbol{K}_{3C}\quad \boldsymbol{K}_{3Z})\\&-i\frac{\omega^2}{\tilde{k}_{Lm}}\big((\boldsymbol{Q}_L\quad \boldsymbol{Q}_S\quad \boldsymbol{Q}_C\quad \boldsymbol{Q}_Z)\big)\begin{pmatrix}\boldsymbol{\varphi}_{Lm}\\ \boldsymbol{\varphi}_{Sm}\\ \boldsymbol{\varphi}_{Cm}\\ k_{Zm}\boldsymbol{\varphi}_{zm}\end{pmatrix}=\mathbf{0}.\end{aligned}\tag{139}$$

(Eq. 139) then can be further simplified as:

$$\left(\boldsymbol{H}_{11}+k_{Zm}^{2}\boldsymbol{H}_{12}+\frac{\boldsymbol{H}_0}{\tilde{k}_{Lm}}\right)\begin{pmatrix}\boldsymbol{\varphi}_{Lm}\\ \boldsymbol{\varphi}_{Sm}\\ \boldsymbol{\varphi}_{Cm}\\ k_{Zm}\boldsymbol{\varphi}_{zm}\end{pmatrix}=\mathbf{0}, \tag{140}$$

where

$$\boldsymbol{H}_{11}=(\boldsymbol{K}_{1L}\quad \boldsymbol{K}_{1S}\quad \boldsymbol{K}_{1C}\quad \boldsymbol{K}_{1Z}+i\boldsymbol{K}_{2Z})-\omega^2(\boldsymbol{M}_L\quad \boldsymbol{M}_S\quad \boldsymbol{M}_C\quad \boldsymbol{M}_Z),$$

$$\boldsymbol{H}_{12}=\ (\boldsymbol{K}_{3L}+i\boldsymbol{K}_{2L}\quad \boldsymbol{K}_{3S}+i\boldsymbol{K}_{2S}\quad \boldsymbol{K}_{3C}+i\boldsymbol{K}_{2C}\quad \boldsymbol{K}_{3Z}),$$

$$\boldsymbol{H}_0=\ -i\omega^2\big((\boldsymbol{Q}_L\quad \boldsymbol{Q}_S\quad \boldsymbol{Q}_C\quad \boldsymbol{Q}_Z)\big).$$

The matrix block H_0 in (Eq. 140) can be simplified to the form of:

$\boldsymbol{H}_0=-i\omega^2\big((\boldsymbol{Q}_L\quad \mathbf{0}\quad \mathbf{0}\quad \mathbf{0})\big)$ as the mechanical energy of the waveguide is transferred to the fluid in the normal direction only. By substituting (Eq. 116) to (Eq. 140), we obtain:

$$\left(\boldsymbol{H}_1+\tilde{k}_{Lm}^{2}\boldsymbol{H}_3+\frac{\boldsymbol{H}_0}{\tilde{k}_{Lm}}\right)\begin{pmatrix}\boldsymbol{\varphi}_{Lm}\\ \boldsymbol{\varphi}_{Sm}\\ \boldsymbol{\varphi}_{Cm}\\ k_{Zm}\boldsymbol{\varphi}_{zm}\end{pmatrix}=\mathbf{0}, \tag{141}$$

where $\boldsymbol{H}_1=\boldsymbol{H}_{11}+\tilde{k}^2\boldsymbol{H}_{12}\ ,\boldsymbol{H}_3=-\boldsymbol{H}_{12}$. Finally, (Eq. 141) can be rewritten as a 3rd polynomial Eigenvalue problem as:

$$\begin{aligned}\left(\tilde{k}_{Lm}\boldsymbol{H}_1+\tilde{k}_{Lm}^{3}\boldsymbol{H}_3+\boldsymbol{H}_0\right)\begin{pmatrix}\boldsymbol{\varphi}_{Lm}\\ \boldsymbol{\varphi}_{Sm}\\ \boldsymbol{\varphi}_{Cm}\\ k_{Zm}\boldsymbol{\varphi}_{zm}\end{pmatrix}' &= \\ =\left(\tilde{k}_{Lm}\boldsymbol{H}_1+\tilde{k}_{Lm}^{3}\boldsymbol{H}_3+\boldsymbol{H}_0\right)\boldsymbol{\varphi}'_m&=\mathbf{0}.\end{aligned} \tag{142}$$

(Eq. 142) now can be recast to a linear Eigenvalue problem as:

$$\begin{aligned}\left(\begin{pmatrix}\mathbf{0} & \boldsymbol{H}_1 & \boldsymbol{H}_0\\ \boldsymbol{I} & \mathbf{0} & \mathbf{0}\\ \mathbf{0} & \boldsymbol{I} & \mathbf{0}\end{pmatrix}-\tilde{k}_{Lm}\begin{pmatrix}-\boldsymbol{H}_3 & \mathbf{0} & \mathbf{0}\\ \mathbf{0} & \boldsymbol{I} & \mathbf{0}\\ \mathbf{0} & \mathbf{0} & \boldsymbol{I}\end{pmatrix}\right)\begin{pmatrix}\tilde{k}_{Lm}^{2}\boldsymbol{\varphi}'_m\\ \tilde{k}_{Lm}\boldsymbol{\varphi}'_m\\ \boldsymbol{\varphi}'_m\end{pmatrix} &= \\ =\left(\boldsymbol{A}-\tilde{k}_{Lm}\boldsymbol{B}\right)\begin{pmatrix}\tilde{k}_{Lm}^{2}\boldsymbol{\varphi}'_m\\ \tilde{k}_{\mathrm{Lm}}\boldsymbol{\varphi}'_m\\ \boldsymbol{\varphi}'_m\end{pmatrix}&=\mathbf{0},\end{aligned} \tag{143}$$

where $\boldsymbol{I}$ is the identity matrix of dimensions $N\times N$, where N is the number of *dof* over the cross-section of the waveguide. (Eq. 143) can be reduced by omitting zero members as:

$$\begin{aligned}\left(\begin{pmatrix}\mathbf{0} & \boldsymbol{H}_1 & \boldsymbol{H'}_0\\ \boldsymbol{I} & \mathbf{0} & \mathbf{0}\\ \mathbf{0} & \boldsymbol{I'} & \mathbf{0}\end{pmatrix} - \tilde{k}_{Lm}\begin{pmatrix}-\boldsymbol{H}_3 & \mathbf{0} & \mathbf{0}\\ \mathbf{0} & \boldsymbol{I} & \mathbf{0}\\ \mathbf{0} & \mathbf{0} & \boldsymbol{I''}\end{pmatrix}\right)\begin{pmatrix}\tilde{k}_{Lm}^2\boldsymbol{\varphi'}_m\\ \tilde{k}_{Lm}\boldsymbol{\varphi'}_m\\ \boldsymbol{\varphi''}_m\end{pmatrix} &= \\ = \left(\boldsymbol{A'} - \tilde{k}_{Lm}\boldsymbol{B'}\right)\begin{pmatrix}\tilde{k}_{Lm}^2\boldsymbol{\varphi'}_m\\ \tilde{k}_{Lm}\boldsymbol{\varphi'}_m\\ \boldsymbol{\varphi''}_m\end{pmatrix} &= \mathbf{0},\end{aligned} \tag{144}$$

where the number of columns in the $\boldsymbol{H'}_0$ matrix, the number of rows in matrix $\boldsymbol{I'}$ are the same as the number of both rows and columns in matrix $\boldsymbol{I''}$. The number of rows in vector $\boldsymbol{\varphi''}_m$ coincides with the number of columns M in matrix $\boldsymbol{Q}_L$, where M is the number of nodes in contact with the fluid.

It is convenient to present (Eq. 144) as the standard Eigenvalue problem:

$$\left((\boldsymbol{B'})^{-1}\boldsymbol{A'} - \tilde{k}_{Lm}\boldsymbol{I}\right)\begin{pmatrix}\tilde{k}_{Lm}^2\boldsymbol{\varphi'}_m\\ \tilde{k}_{Lm}\boldsymbol{\varphi'}_m\\ \boldsymbol{\varphi''}_m\end{pmatrix} = \left((\boldsymbol{B'})^{-1}\boldsymbol{A'} - \tilde{k}_{Lm}\boldsymbol{I}\right)\boldsymbol{Y}, \tag{145}$$

The fluid load can be taken into account in cases of both elastic and viscoelastic waveguide materials. The rheological model of linear viscoelasticity is formulated by using complex Young's modulus and is an individual case of the generalized Maxwell's model. This study considers Rayleigh damping in order to account for the linear viscoelasticity of the waveguide under harmonic excitation.

A substitution of Rayleigh damping matrix $\boldsymbol{C} = a\boldsymbol{M} + b\boldsymbol{K}$ into (Eq. 133) yields:

$$\left(\widehat{\boldsymbol{K}}_1 + ik_Z\widehat{\boldsymbol{K}}_2 + k_Z^2\widehat{\boldsymbol{K}}_3 - \omega^2\widehat{\boldsymbol{M}} - i\frac{\omega^2}{\tilde{k}_L}\boldsymbol{Q}\right)\overline{\boldsymbol{U}} = \mathbf{0}, \tag{146}$$

where $\widehat{\boldsymbol{K}}_j = (1 - i\omega b)\boldsymbol{K}_j, j = 1,2,3$ and $\widehat{\boldsymbol{M}} = (1 - i\omega^{-1}a)\boldsymbol{M}$. It can be noted that the Rayleigh damping term presents attenuation dependent on frequency. It is important to note that (Eq. 146) is derived from (Eq. 58) by assuming $k_Z^* \approx k_Z$. Therefore, the Rayleigh damping model supports just low damping for modes, where $(Re(k_Z) \gg Im(k_Z))$.

(Eq. 146) can be linearized and solved as explained by formulas (Eqs. 134–145). As (Eq. 145) provides $2N + 2M$ solutions of $\tilde{k}_{Lm}$, therefore $2(2N + 2M)$ solutions for k_Z are acquired as [99]:

$$k_Z = \pm\sqrt{\tilde{k}^2 - \tilde{k}_L^2}. \tag{147}$$

The $2N$ wavenumbers as $(Re(k_Z) + Im(k_Z))$ and $2N$ wavenumbers as $(-Re(k_Z) - Im(k_Z))$ represent the outgoing forward and backward wavemodes, respectively. The outgoing modes radiate mechanical energy to the surrounding medium while traveling. This energy dissipation causes the decrease of amplitudes characterized by the magnitudes of the imaginary part ($Im(k_Z) \neq 0$). $2N$ wavenumbers as $(Re(k_Z) - Im(k_Z))$ and $2N$ wavenumbers as $(-Re(k_Z) + Im(k_Z))$ represent the forward and backward incoming modes, respectively. The incoming modes represent the inward wave from the surrounding medium into the waveguide which amplifies the amplitude of the wave within the waveguide.

$2M$ wavenumbers as $(Re(k_Z) + 0)$ and $2M$ wavenumbers as $(-Re(k_Z) + 0)$ represent the forward and backward quasi-Scholte wavemodes. They propagate at the interface of the waveguide and the fluid. Their energy distribution is concentrated along the interface as they travel. Quasi-Scholte waves do not attenuate and disperse to a significant extent [74, 75, 101].

If the Rayleigh damping of the immersed waveguide is considered in (Eq. 146), the imaginary parts of the resulting wavenumbers account for energy losses due to the geometrical energy spread and the internal friction.

4.3 Mode Tracking

SAFE models with refined discretization of the waveguide cross-section provide a large number of wavemode solutions to (Eq. 146) due to the multi-modal nature of the waves. Different modes with numerically similar wavenumbers for the same angular frequency may appear. Therefore, it is difficult to distinguish among the dispersion curves of different relaying just on the grounds of the graphical appearance of the dispersion curves. At different angular frequencies, tracking a mode of an individual modal shape is of interest as dispersion curves are generated. The approach described in [34] is adopted in this study for tracking the wavenumbers obtained from (Eq. 146) and assigning them to the same mode characterized by its individual modal shape.

Tracking wavenumber $\tilde{k}_{Lm}$ at given value ω is based on finding increment $\Delta\tilde{k}_{Lm}$ at which the updated wavenumber $\tilde{k}_{Lm} + \Delta\tilde{k}_{Lm}$ at $\omega + \Delta\omega$ would belong to the m-th mode. The right $\boldsymbol{u}_m$ and left $\boldsymbol{v}_m$ natural vectors of the m-th mode in (Eq. 144) at frequency ω satisfy such equations as [34]:

$$\left(\boldsymbol{A}' - \tilde{k}_{Lm}\boldsymbol{B}'\right)\boldsymbol{u}_m = \boldsymbol{0}, \tag{148}$$

$$\boldsymbol{v}_m\left(\boldsymbol{A}' - \tilde{k}_{Lm}\boldsymbol{B}'\right) = \boldsymbol{0}. \tag{149}$$

At frequency $\omega + \Delta\omega$ (Eq. 148) can be rewritten as [34]:

$$\Big((\boldsymbol{A}' + \Delta\boldsymbol{A}') - \left(\tilde{k}_{Lm} + \Delta\tilde{k}_{Lm}\right)(\boldsymbol{B}' + \Delta\boldsymbol{B}')\Big)\,(\boldsymbol{u}_m + \Delta\boldsymbol{u}_m) = \boldsymbol{0}, \tag{150}$$

where matrices $\Delta\boldsymbol{A}'$ and $\Delta\boldsymbol{B}'$ are calculated at frequency $\Delta\omega$. After expending the terms in (Eq. 150), the second order differential terms are omitted for simplicity, therefore, $\Delta\omega$ must be selected and varied along ω with caution.

While more sophisticated estimation methods exist (for example, with the employment of Pade expansion [29]), in this case, just a linear estimation is found to be sufficient. (Eq. 150) can be simplified as [34]:

$$\left(\boldsymbol{A}' - \tilde{k}_{Lm}\boldsymbol{B}'\right)\Delta\boldsymbol{u}_m = \left(\tilde{k}_{Lm}\Delta\boldsymbol{B}' + \Delta\tilde{k}_{Lm}\boldsymbol{B}' - \Delta\boldsymbol{A}'\right)\ \boldsymbol{u}_m. \tag{151}$$

Vector $\Delta\boldsymbol{u}_m$ can be expanded in the base of independent right natural vectors $\boldsymbol{u}_l$ $(l = \overline{1, 2N + 2M})$ as [34]:

$$\Delta\boldsymbol{u}_m = \textstyle\sum_{l=1}^{2N+2M} \alpha_{lm}\boldsymbol{u}_l, \tag{152}$$

where α_{lm} is the superposition weight of the l-th mode for vector $\Delta\boldsymbol{u}_m$ of the tracked m-th mode, and $2N + 2M$ is the number of solutions $\tilde{k}_{Lm}$.

The application of the orthogonality condition is written as:

$$\begin{gathered}\boldsymbol{v}_m\boldsymbol{A}'\boldsymbol{u}_l = \begin{cases}\boldsymbol{v}_m\boldsymbol{A}'\boldsymbol{u}_m; & m = l\\ 0 & m \neq l\end{cases}\\ \boldsymbol{v}_m\boldsymbol{B}'\boldsymbol{u}_l = \begin{cases}\boldsymbol{v}_m\boldsymbol{B}'\boldsymbol{u}_m; & m = l\\ 0 & m \neq l\end{cases}.\\ \tilde{k}_{Lm} = \frac{\boldsymbol{v}_m\boldsymbol{A}'\boldsymbol{u}_m}{\boldsymbol{v}_m\boldsymbol{B}'\boldsymbol{u}_m}\end{gathered} \tag{153}$$

It leads to the extraction of the wave number increment from (Eq. 151) [34]:

$$\Delta\tilde{k}_{Lm} \approx \frac{\boldsymbol{v}_m\left(\Delta\boldsymbol{A}' - \tilde{k}_{Lm}\Delta\boldsymbol{B}'\right)\boldsymbol{u}_m}{\boldsymbol{v}_m\boldsymbol{B}'\boldsymbol{u}_m}. \tag{154}$$

This estimate can be used for identifying the natural wavenumber value which should be chosen for the m-th dispersion curve at the next angular frequency value.

4.4 Dispersion Relations for Immersed Waveguide

4.4.1 Phase Velocity

The dispersion relations can be presented by phase velocity $c_{ph} = \frac{\omega}{Re(k_Z)}$ which is a ratio between the given ω and the real part of the calculated wavenumbers k_Z when using (Eq. 145). The phase velocities of the modes of the immersed waveguide SAFE model with 3×3 FE over the rectangular cross-section is presented in (Fig. 4.5 (a)). The material properties of the aluminum waveguide are as follows: mass density $\rho = 2780\frac{kg}{m^3}$, Young's modulus $E = 7.24 \cdot 10^{10}\ Pa$, Poisson's ratio $\nu = 0.34$, and cross-section $0.001\,m \times 0.001\,m$. The material properties of the perfect fluid (water) are as follows: mass density$\rho = 1000\frac{kg}{m^3}$, the velocity of the pressure (longitudinal) wave $\tilde{c}_L = 1500\ \frac{m}{s}$. The results of tracking only the fundamental and quasi-Scholte modes while using (Eq. 154) are shown in (Fig. 4.5 (b)).

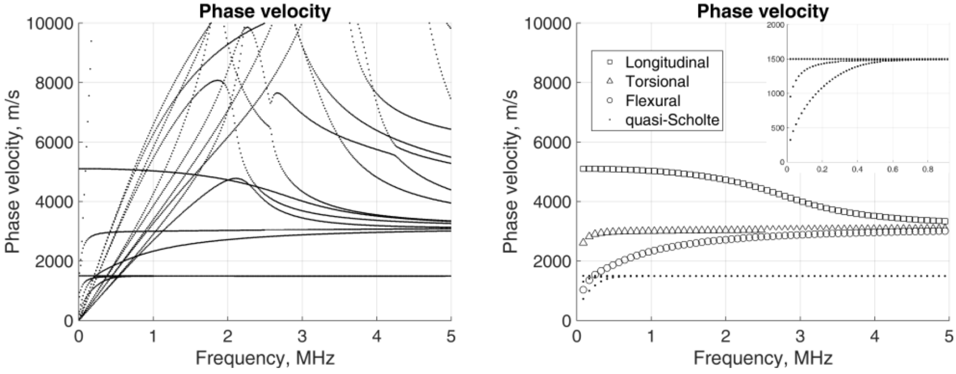

a) b)

Fig. 4.5. (a) Phase velocities of modes in the immersed waveguide; (b) Phase velocities of fundamental and quasi-Scholte modes in the immersed waveguide.

It can be noted that the fluid load mostly affects the torsional and flexural modes in the low frequency range. However, the longitudinal mode in the immersed waveguide does not exhibit evident influence of attenuation at low frequencies, since the displacement field is predominant in the OZ direction. The interaction of this mode with the fluid at low frequencies is insignificant. Our analysis demonstrated that the immersed waveguide of the square cross-section supported three distinct groups of Scholte waves (the zoomed part in (Fig. 4.5 (b))). The threshold of velocity of these types of modes is $\tilde{c}_L = 1500 \frac{m}{s}$ (that is slightly higher than the Scholte wave velocity in water [101]), which determines them as subsonic waves with respect to the sound velocity in the leaky medium.

Attention must be drawn to the quasi-Scholte modes because such techniques as SAFE coupled with 2.5 D boundary elements [102], SAFE with PML [61] and SAFE with absorbing region [103], dashpot boundary condition coupled to SAFE [70] that deal with the leaky modes do not seem to be able to provide us with dispersion results for 3D quasi-Scholte waves.

The obtained attenuation curves are presented in (Fig. 4.6 (a)). The attenuation of the fundamental modes is relatively small when compared with the attenuation of the higher modes (Fig. 4.6 (b)).

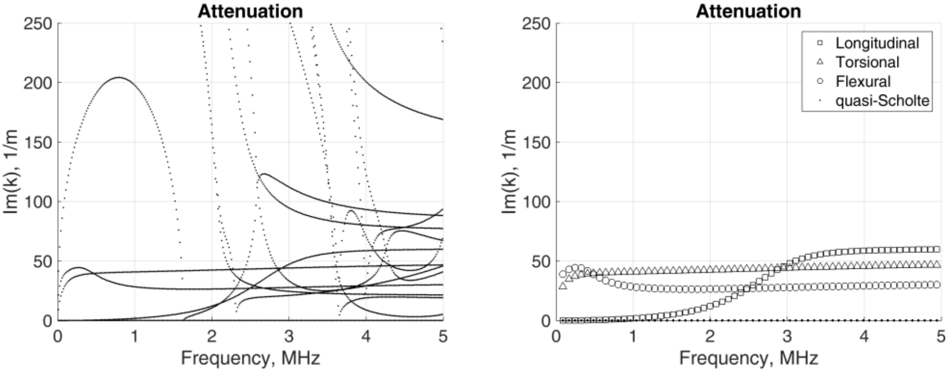

a) b)

Fig. 4.6. (a) Attenuation of modes in the immersed waveguide; (b) Attenuation of the fundamental and quasi-Scholte modes in the immersed waveguide.

However, quasi-Scholte modes exhibited a low attenuation constant over the frequency range. Therefore, quasi-Scholte modes were almost non-dispersive. They tend to retain their wave shape while travelling, which is a useful feature in many practical applications.

For comparing the results of the obtained dispersion curves against the dispersion curves exhibited by the lossless waveguide surrounded by vacuum, the waveguide with Rayleigh damping and the immersed waveguide was analyzed. Initially, the analysis was carried out by examining a single FE over the cross-section model in order to reveal the main properties of the solutions, which are inherent for the analyzed waveguide. The results are summarized in (Fig. 4.7). For obtaining better precision solutions, we further employ the finer mesh over the cross-section of the waveguide.

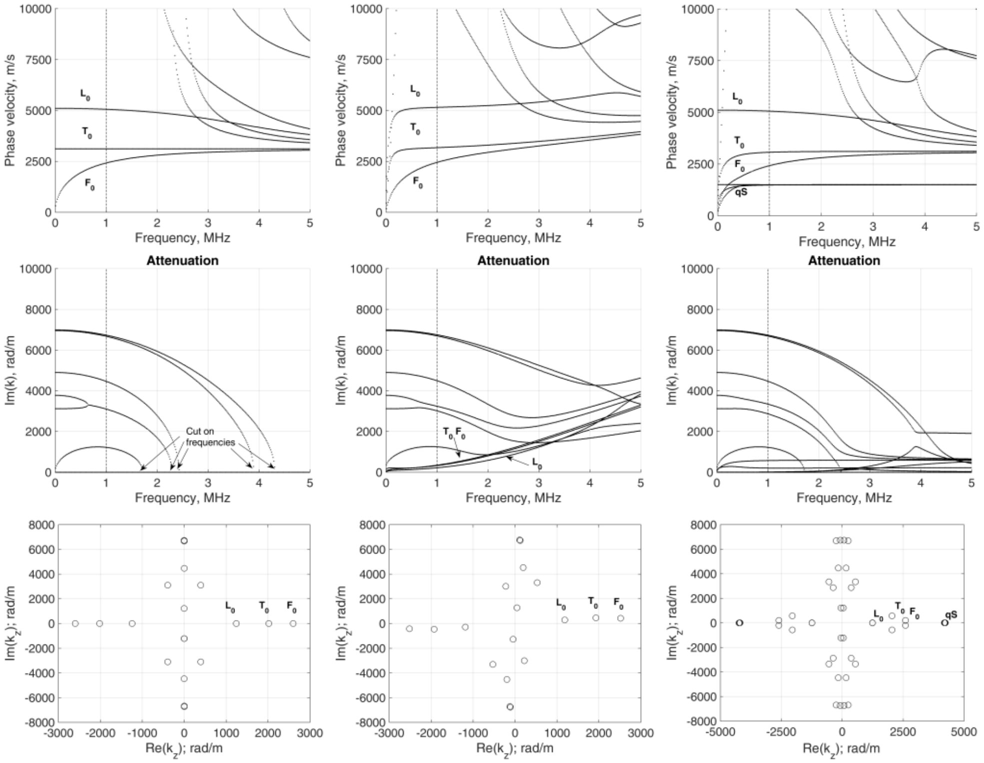

a) b) c)

Fig. 4.7. Phase velocity, attenuation and wavenumbers (at 1 MHz (the dashed line)) of the waveguide (a) in the vacuum; (b) with Rayleigh damping $a = 1e6; b = 3e - 8$; (c) immersed in the perfect fluid.

(Fig. 4.7 (a)) demonstrates that, in the case of the surrounding vacuum, three fundamental modes exist at the zero frequency. The higher modes appear at the cut-on frequency where attenuation $Im(k_Z)$ approaches zero. Thus evanescent modes become propagative. The wavenumbers at a frequency of $1MHz$ (represented by the dashed line) on the complex plane come out as symmetric with respect to the axes of the complex plane. The propagative modes correspond to the wavenumbers with $Im(k_Z) = 0$, while the end modes (the local vibrations not capable of transferring energy) correspond to $Re(k_Z) = 0$, and the remaining modes are evanescent modes with the rapidly decaying amplitude. Such wavenumbers as $\pm(Re(k_Z) - Im(k_Z))$ have no physical meaning as they represent fictitious wavemodes with the increasing amplitude as they travel.

In those cases when damping is present (Fig. 4.7 (b)), all the modes are evanescent. Their wavenumbers do not retain symmetry on the complex plane, and the cut-on frequencies do not apply anymore. At higher frequencies in the case of severe damping (say, $a = 1e6; b = 3e - 8$), the phase velocity curve does not converge to the phase velocity of Rayleigh's surface wave. This indicates the appearance of certain errors of the wave solutions which are caused by the commonly used assumption $k_Z^* = k_Z$ as far as some more damped waveguides are concerned.

In the case of the immersed waveguide (Fig. 4.7 (c)), all the modes (with the exception of quasi-Scholte modes) are evanescent. Some modes cut on frequencies as, in the case of vacuum surrounding, the wavenumbers demonstrate symmetry with respect to the axes of the complex plane.

The verification of the model was performed by using the numerical experiments where the waveguide of the cross-section of $0.006\,m \times 0.012\,m$, FE mesh 3×6 was considered. Initially, the ratio between the height and the length of the cross-section was $1:2$. As this ratio increased, the obtained dispersion curves converged to those of the plate (Fig. 4.8).

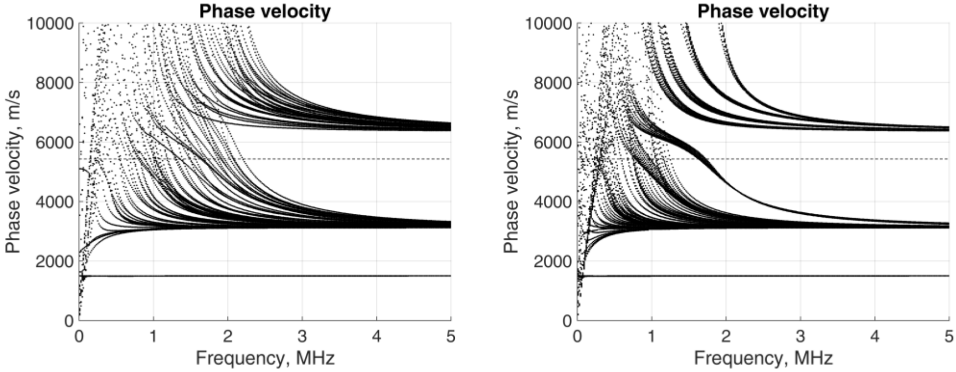

FE domain: 3×6; ratio $1:2$ FE domain: 3×10; ratio $1:10$

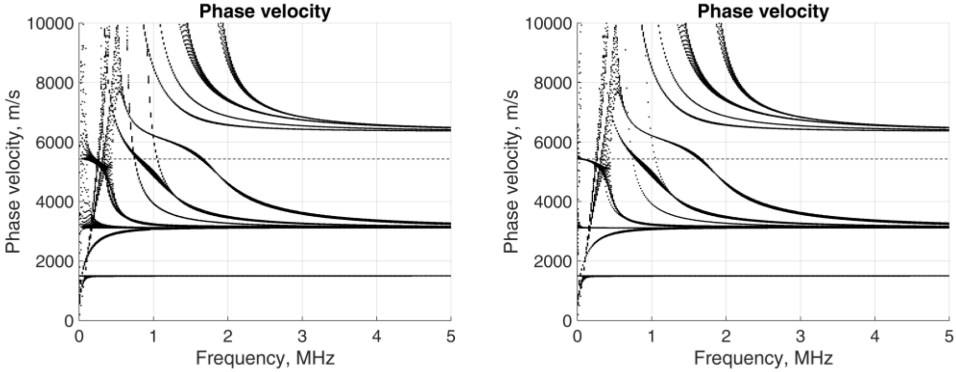

FE domain: 3×15; ratio $1:100$ FE domain: 3×15; ratio $1:1000$

Fig. 4.8. The convergence of the model.

As the longitudinal mode at the close to zero frequency approached the threshold of wave velocity in the plate as $c_{plate} = \frac{\sqrt{E}}{\sqrt{\rho(1-\nu^2)}}$ (the dashed line in Fig. 4.8), it can be assumed that the obtained fundamental modes of the analyzed waveguide match those of the plate of the same height as the height of the cross-section of the waveguide. The results show evident convergence and agree reasonably well with the results published in [99] for the plate.

4.4.2 Group Velocity

In the case of attenuation, due to the damped medium, group velocity c_{gr} no longer expresses the velocity at which mechanical energy is being transferred since direct differentiation $c_{gr} = \frac{\partial \omega}{\partial k}$ is performed in respect to the real part of the complex wavenumber. These calculations might lead to infinite velocities at some locations of dispersion curves, then the energy velocity is used instead [104], the wave carries its potential and kinetic energy along the structure at the energy velocity, and a single FE is defined [66] as:

$$c_{en} = \frac{\int_{S_e} \boldsymbol{P} dS_e}{\int_{S_e} (E_p + E_k) dS_e}, \tag{155}$$

where $\boldsymbol{P}$ is the time-averaged $0Z$ axial component of the Poynting vector, E_p and E_k are the time-averaged potential and the kinetic energy, respectively, S_e is the area of the cross-section in the FE. The natural solutions from (Eq. 145) can be straightforwardly used to calculate the terms [66]:

$$\begin{gathered} \int_{S_e} \boldsymbol{P} dS_e = \frac{\omega}{2} Im\left(\overline{\boldsymbol{U}}_e{}^{*} (\boldsymbol{K}'_2 + ik\boldsymbol{K}_3) \overline{\boldsymbol{U}}_e\right) \\ \int_{S_e} E_k dS_e = \frac{\omega^2}{4} Re\left(\overline{\boldsymbol{U}}_e{}^{*} \boldsymbol{M} \overline{\boldsymbol{U}}_e\right) \\ \int_{S_e} E_p dS_e \ = \ \frac{1}{4} Re\left(\overline{\boldsymbol{U}}_e{}^{*} (\boldsymbol{K}_1 + ik\boldsymbol{K}'_2 - ik^{*} \boldsymbol{K}'^{T}_2 + k^{*} k \boldsymbol{K}_3) \overline{\boldsymbol{U}}_e\right). \end{gathered} \tag{156}$$

Still, the group velocity for modes with only minor attenuation could be used for eluding direct differentiation in respect to the wavenumber. A proposed approach [105] is used to obtain the group velocity for the immersed three-dimensional waveguide. The right $\boldsymbol{V}_m$ and left $\boldsymbol{W}_m$ natural vectors of the m-th mode satisfy the following equations:

$$\left(\boldsymbol{A}' - \tilde{k}_{Lm} \boldsymbol{B}'\right) \boldsymbol{V}_m = \boldsymbol{0}, \boldsymbol{W}_m \left(\boldsymbol{A}' - \tilde{k}_{Lm} \boldsymbol{B}'\right) = \boldsymbol{0}. \tag{157}$$

The derivatives of matrices $\boldsymbol{A}'$ and $\boldsymbol{B}'$ in respect to angular frequency ω are obtained [105]:

$$\begin{gathered} \frac{\partial \boldsymbol{A}'}{\partial \omega} = \begin{pmatrix} \boldsymbol{0} & \frac{\partial \boldsymbol{H}_1}{\partial \omega} & \frac{\partial \boldsymbol{H}'_0}{\partial \omega} \\ \boldsymbol{0} & \boldsymbol{0} & \boldsymbol{0} \\ \boldsymbol{0} & \boldsymbol{0} & \boldsymbol{0} \end{pmatrix} = \begin{pmatrix} \boldsymbol{0} & \frac{\partial \left(\boldsymbol{H}_{11} + \left(\frac{\omega}{\tilde{c}_L}\right)^2 \boldsymbol{H}_{12} \right)}{\partial \omega} & \frac{\partial (-i\omega^2 \boldsymbol{Q}_L)}{\partial \omega} \\ \boldsymbol{0} & \boldsymbol{0} & \boldsymbol{0} \\ \boldsymbol{0} & \boldsymbol{0} & \boldsymbol{0} \end{pmatrix} = \\ \begin{pmatrix} \boldsymbol{0} & -2\omega \boldsymbol{M} + 2\frac{\tilde{k}^2}{\omega} \boldsymbol{H}_{12} & -2i\omega \boldsymbol{Q}_L \\ \boldsymbol{0} & \boldsymbol{0} & \boldsymbol{0} \\ \boldsymbol{0} & \boldsymbol{0} & \boldsymbol{0} \end{pmatrix} \text{ and } \frac{\partial \boldsymbol{B}'}{\partial \omega} = \boldsymbol{0}. \end{gathered} \tag{158}$$

Differentiating (Eq. 157) with the right vector in respect to ω yields [105]:

$$\left(\frac{\partial \boldsymbol{A}'}{\partial \omega} - \frac{\partial \tilde{k}_{Lm}}{\partial \omega} \boldsymbol{B}'\right) \boldsymbol{V}_m + \left(\boldsymbol{A}' - \tilde{k}_{Lm} \boldsymbol{B}'\right) \frac{\partial \boldsymbol{V}_m}{\partial \omega} = \boldsymbol{0}. \tag{159}$$

Pre-multiplying (Eq. 159) with the left natural vector $\boldsymbol{W}_m$ from the left hand side yields the second summand to disappear according to (Eq. 157). A relation is then obtained [105]:

$$\boldsymbol{W}_m\left(\frac{\partial \boldsymbol{A}'}{\partial\omega}-\frac{\partial\tilde{k}_{Lm}}{\partial\omega}\boldsymbol{B}'\right)\boldsymbol{V}_m=\boldsymbol{0}. \tag{160}$$

Then, a derivative of the wavenumber in respect to ω from (Eq. 159) is acquired [105]:

$$\frac{\partial\tilde{k}_{Lm}}{\partial\omega}=\frac{\boldsymbol{W}_m\frac{\partial \boldsymbol{A}'}{\partial\omega}\boldsymbol{V}_m}{\boldsymbol{W}_m\boldsymbol{B}\boldsymbol{V}_m}. \tag{161}$$

Further, differentiating (Eq. 116) in terms of ω yields:

$$2\tilde{k}\frac{\partial\tilde{k}}{\partial\omega}=2\frac{\tilde{k}^2}{\omega}=2\tilde{k}_L\frac{\partial\tilde{k}_L}{\partial\omega}+2\tilde{k}_Z\frac{\partial\tilde{k}_Z}{\partial\omega}. \tag{162}$$

(Eq. 159) can be rewritten as:

$$\frac{\partial\tilde{k}_Z}{\partial\omega}=\frac{\frac{\tilde{k}^2}{\omega}-\tilde{k}_L\frac{\partial\tilde{k}_L}{\partial\omega}}{\tilde{k}_Z}. \tag{163}$$

Finally, the group velocity c_{grm} of the m-th mode reads as [105]:

$$c_{grm}=\frac{\partial\omega}{\partial\tilde{k}_Z}=\frac{\tilde{k}_Z}{\frac{\tilde{k}^2}{\omega}-\tilde{k}_L\frac{\partial\tilde{k}_L}{\partial\omega}}. \tag{164}$$

Running the computations of the group velocity at each given angular frequency provides us with dispersion relations. The group velocity results for the same immersed waveguide with 3 × 3 FE over the cross-section described in the previous section are presented in (Fig. 4.9 (a)). The results of tracking only the fundamental and one of the quasi-Scholte modes using (Eq. 154) are shown in (Fig. 4.9 (b)), and they share many similarities with those of the immersed plate [106], [71].

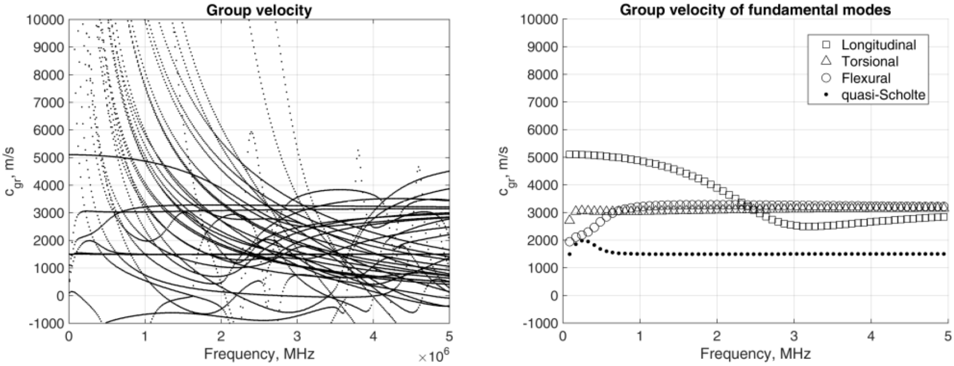

a) b)

Fig. 4.9. (a) Group velocity for the immersed waveguide; (b) Group velocity for the fundamental modes in the immersed waveguide.

It is evident that numerous modes which, within a specific frequency range, exhibit a negative group velocity at the positive wavenumber do exist. A considerably lower number of these occurrences can be observed in the case of an undamped waveguide.

4.5 Dispersion Relations for Immersed Waveguide with Rayleigh Damping

The fluid load affects the waveguide of both elastic and viscoelastic material. Rayleigh damping is considered for immersed waveguide to account for linear viscoelasticity as in the previous section. The introduction of matrix $\boldsymbol{C}$ for Rayleigh damping in (Eq. 133) yields:

$$\left(\widehat{\boldsymbol{K}}_1 + ik_Z\widehat{\boldsymbol{K}}_2 + k_Z^2\widehat{\boldsymbol{K}}_3 - \omega^2\widehat{\boldsymbol{M}} - i\frac{\omega^2}{\tilde{k}_L}\boldsymbol{Q}\right)\overline{\boldsymbol{U}} = \boldsymbol{0},$$

where $\widehat{\boldsymbol{K}}_j = (1 - i\omega b)\boldsymbol{K}_j, j = 1,2,3$ and $\widehat{\boldsymbol{M}} = (1 - i\omega^{-1}a)\boldsymbol{M}$.

The algorithm to acquire dispersion relations for evanescent waves in the immersed and in the immersed damped waveguide using SAFEM is summarized in (Fig. 4.10).

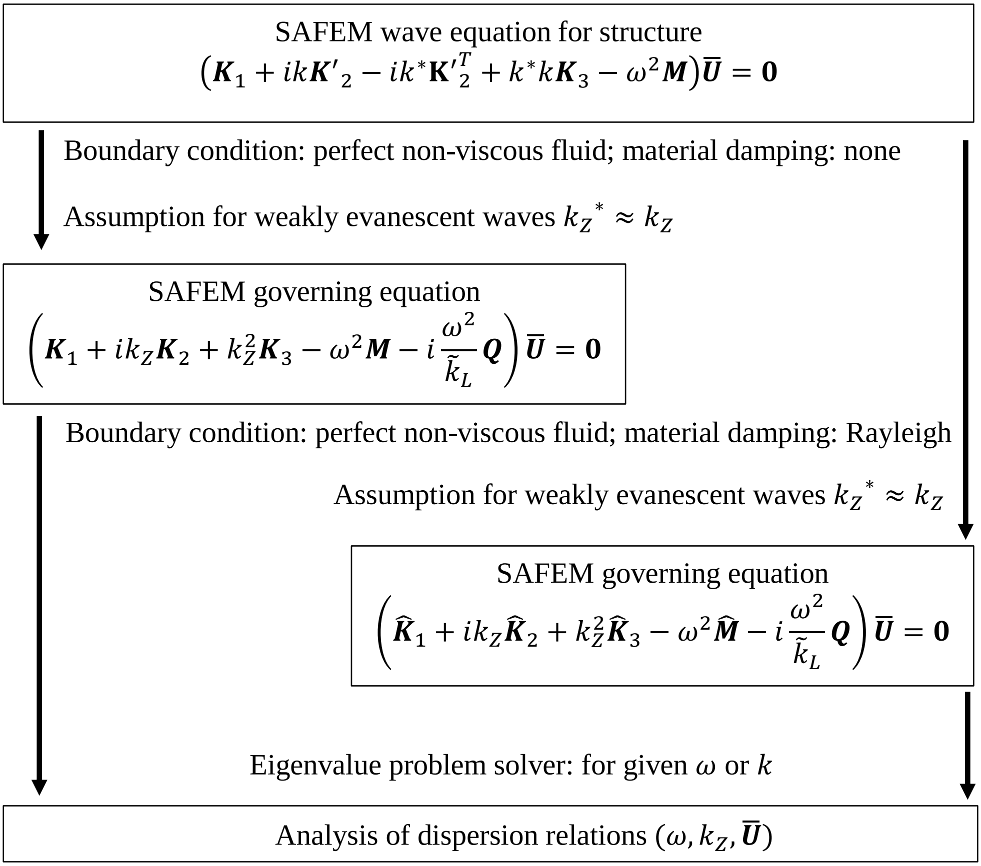

Fig. 4.10. A flowchart of the algorithm to obtain the dispersion relations for evanescent waves in the immersed and in the immersed and damped waveguide using SAFEM.

The dispersion results for the fundamental modes of the immersed waveguide with Rayleigh damping, where coefficients a and b were varied, are shown in (Fig. 4.11). As damping was increased, the quasi-Scholte wavemode remained unattenuated and merged to the common group of wavemodes with the constant phase velocity. In case of severe damping (Fig. 4.11 c), the phase velocity curves of the fundamental modes at higher frequencies tended to bend away from the dispersion curves of quasi-Scholte modes. This clearly indicates non-feasible results, and the symmetry of the wavenumbers on the complex plane is destroyed. The cause of the inadequacy of the damped immersed waveguide model is likely due to the fact that the assumption about the complex conjugate of the wavenumbers was no longer met. In this analysis, the model is considered to be adequate as long phase velocities asymptotically and monotonically approach the Rayleigh surface wave phase velocity value. This is valid for isotropic waveguides [107].

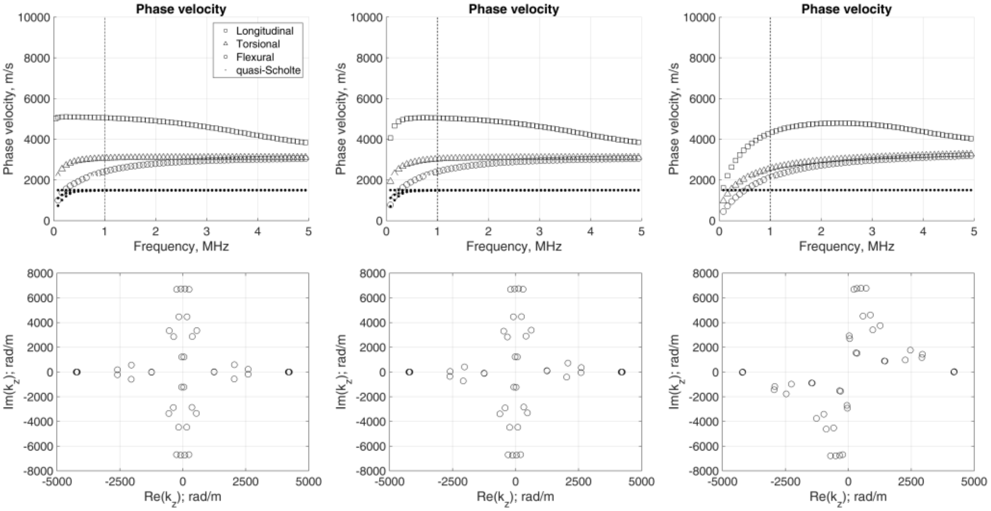

a) b) c)

Fig. 4.11. Phase velocity and wavenumbers (at 1 MHz (the dashed line)) of the immersed waveguide with Rayleigh damping; $a = 1e5; b = 1e-10$ (a); $a = 1e6; b = 1e-9$ (b); $a = 1e7; b = 1e-8$ (c).

It was observed [108] that viscous fluid loading on the plate reduces the phase velocity of Love waves. By modeling the soft tissue as a transverse isotropic viscoelastic plate immersed in a fluid, it was also observed that the phase velocity of the shear wave that travels in a direction perpendicular to the fibres is reduced due to the increasing viscosity [109]. The reduction of the phase velocity due to the increasing material damping, especially in a low frequency, is visible in (Fig. 4.11).

As shown in the previous section (Fig. 3.17) and (Fig. 3.2), mass damping in the plate and the waveguide significantly modifies the phase velocity in the low frequency range. A similar pattern of the longitudinal mode bending is demonstrated in [63], where guided modes in the aluminum plate and radiating into an elastomer were simulated. In case of the immersed waveguide as shown in (Eq. 129), the effect of fluid loading is defined by matrix $\boldsymbol{C}$ which stores the mass density of the fluid. As seen in (Eq. 140), the fluid load results in a complex valued mass matrix in the Eigenvalue problem; therefore, mass damping can also be related with the energy dissipation to the surrounding media. On the other hand, viscoelasticity, introduced by the complex stiffness matrix, has little effect on the phase velocity in plates [110], [111].

4.6 Force Response

The two-dimensional force response [106] can be extended to the three-dimensional one. The theoretical assumptions to achieve this possibility shall be discussed in this section. Calculated modal solutions $(k_Z, \tilde{k}_L, c_{ph}, c_{gr})$ for a given frequency ω can be exploited to construct the time-transient response to the external loading varied in time and space. A dynamic nodal loading reads as:

$$\boldsymbol{F}_{loading}(z,t) = \boldsymbol{F}(z)e^{-i\omega t} = \overline{\boldsymbol{F}}e^{i(k_Z z-\omega t)}, \tag{165}$$

where $\boldsymbol{F}(z) = \int_{-\infty}^{+\infty} \boldsymbol{F}_{loading}(z,t)e^{i\omega t}dt$ is the time Fourier transform, whereas $\overline{\boldsymbol{F}} = \int_{-\infty}^{+\infty} \boldsymbol{F}(z)e^{-ik_Z z}dz$ is the spatial Fourier transform. When concentrated at arbitrary source location z_0, the loading can be expressed via the Dirac delta as $\boldsymbol{F}(z) = \boldsymbol{F}\delta(z - z_0)$. A schematic line loading on the immersed waveguide and the normal to the boundary of the cross-section is shown in (Fig. 4.12).

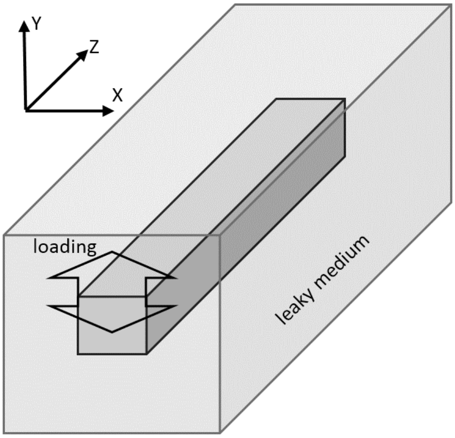

Fig. 4.12. A schematic representation of line loading in an immersed waveguide.

The nodal vector $(1 \times N)$ of line forcing reads as:

$$\overline{\boldsymbol{F}} = \int_{-\infty}^{+\infty} \boldsymbol{F}\delta(z - z_0)e^{-ik_Z z}dz = \boldsymbol{F}e^{-ik_Z z_0}. \tag{166}$$

(Eq. 130) can be rewritten as [106]:

$$\left(\boldsymbol{K}_1 + ik_Z\boldsymbol{K}_2 + k_Z^2\boldsymbol{K}_3 - \omega^2\boldsymbol{M} - i\frac{\omega^2}{\tilde{k}_L}\boldsymbol{Q}\right)\overline{\boldsymbol{U}} = \overline{\boldsymbol{F}}. \tag{167}$$

(Eq. 167) for the Eigenvalue problem reads as [106]:

$$\left(\boldsymbol{A}' - \tilde{k}_L\boldsymbol{B}'\right)\boldsymbol{Y} = \overline{\boldsymbol{F}}', \tag{168}$$

where dimensions of $\overline{\boldsymbol{F}}' = \begin{pmatrix}\overline{\boldsymbol{F}} \\ \boldsymbol{0}\end{pmatrix}$ are in accordance to matrices $\boldsymbol{A}'$ and $\boldsymbol{B}'$. The solution of homogenous (Eq. 168) for the m-th mode while using (Eq. 144) is the right natural vector, and it reads as:

$$\boldsymbol{V}_m = \begin{pmatrix}\tilde{k}_{Lm}^2\boldsymbol{\varphi}'_m \\ \tilde{k}_{Lm}\boldsymbol{\varphi}'_m \\ \boldsymbol{\varphi}''_m\end{pmatrix} = \begin{pmatrix}\tilde{k}_{Lm}^2\boldsymbol{\varphi}'_{om} \\ \tilde{k}_{Lm}^2 k_{Zm}\boldsymbol{\varphi}'_{zm} \\ \tilde{k}_{Lm}\boldsymbol{\varphi}'_{om} \\ \tilde{k}_{Lm}k_{Zm}\boldsymbol{\varphi}'_{zm} \\ \boldsymbol{\varphi}''_m\end{pmatrix}, \tag{169}$$

where, according to (Eq. 136),

$$\boldsymbol{\varphi}'_{m} = \begin{pmatrix} \boldsymbol{\varphi}'_{om} \\ k_{Zm}\boldsymbol{\varphi}'_{zm} \end{pmatrix}. \tag{170}$$

The solution of (Eq. 168) can be cast in the base of linearly independent right natural vectors:

$$\boldsymbol{Y} = \sum_{m=1}^{2(N+M)} \alpha_m \boldsymbol{V}_m, \qquad (171),$$

where $\alpha_m$is a scalar. The pre-multiplication of (Eq. 168) by the left natural $\boldsymbol{W}_l$vector and the application of orthogonality relations (Eq. 153) leads to:

$$\begin{gathered} \boldsymbol{W}_l\left(\boldsymbol{A}' - \tilde{k}_L\boldsymbol{B}'\right)\boldsymbol{Y} = \boldsymbol{W}_l\left(\boldsymbol{A}' - \tilde{k}_L\boldsymbol{B}'\right)\sum_{m=1}^{2(N+M)} \alpha_m \boldsymbol{V}_m = \\ = \sum_{m=1}^{2(N+M)} \alpha_m\left(\boldsymbol{W}_l\boldsymbol{A}'\boldsymbol{V}_m - \tilde{k}_L\boldsymbol{W}_l\boldsymbol{B}'\boldsymbol{V}_m\right) = \\ \alpha_l\left(\boldsymbol{W}_l\boldsymbol{A}'\boldsymbol{V}_l - \tilde{k}_L\boldsymbol{W}_l\boldsymbol{B}'\boldsymbol{V}_l\right) = \alpha_l\left(\tilde{k}_{Ll} - \tilde{k}_L\right)\boldsymbol{W}_l\boldsymbol{B}'\boldsymbol{V}_l. \end{gathered} \tag{172}$$

(Eq. 168) can be written as:

$$\alpha_l\left(\tilde{k}_{Ll} - \tilde{k}_L\right)\boldsymbol{W}_l\boldsymbol{B}'\boldsymbol{V}_l = \boldsymbol{W}_l\overline{\boldsymbol{F}}'. \tag{173}$$

The weight of the l-th mode in the force response can be expressed as:

$$\alpha_l = \frac{\boldsymbol{W}_l\overline{\boldsymbol{F}}'}{-\left(\tilde{k}_L - \tilde{k}_{Ll}\right)\boldsymbol{W}_l\boldsymbol{B}'\boldsymbol{V}_l} = \frac{\alpha_l{}'}{\left(\tilde{k}_L - \tilde{k}_{Ll}\right)}. \tag{174}$$

The solution (Eq. 171) can be expressed as:

$$\boldsymbol{Y} = \begin{pmatrix} \tilde{k}_L^2\overline{\boldsymbol{U}}_o \\ \tilde{k}_L^2 k_Z\overline{\boldsymbol{U}}_z \\ \tilde{k}_L\overline{\boldsymbol{U}}_o \\ \tilde{k}_L k_Z\overline{\boldsymbol{U}}_z \\ \overline{\boldsymbol{U}}' \end{pmatrix} = \sum_{m=1}^{2(N+M)} \alpha_m \begin{pmatrix} \tilde{k}_{Lm}^2\boldsymbol{\varphi}'_{\mathrm{om}} \\ \tilde{k}_{Lm}^2 k_{Zm}\boldsymbol{\varphi}'_{zm} \\ \tilde{k}_{Lm}\boldsymbol{\varphi}'_{om} \\ \tilde{k}_{Lm}k_{Zm}\boldsymbol{\varphi}'_{zm} \\ \boldsymbol{\varphi}''_{m} \end{pmatrix}, \tag{175}$$

where $\overline{\boldsymbol{U}}_o$is a vector of the nodal in the non-OZ direction displacements, $\overline{\boldsymbol{U}}'$ is a vector of displacements only for the nodes in contact with a fluid in the normal to the cross-section of the waveguide direction. The nodal vector of displacements can be extracted from (Eq. 175), either from the upper or the middle part of the vector. As the terms in the upper part provide with a more general solution, the displacement vector reads as:

$$\begin{pmatrix} \overline{\boldsymbol{U}}_o \\ \overline{\boldsymbol{U}}_z \end{pmatrix} = \sum_{m=1}^{2(N+M)} \alpha_m \begin{pmatrix} \dfrac{\tilde{k}_{Lm}^2\boldsymbol{\varphi}'_{om}}{\tilde{k}_L^2} \\ \dfrac{\tilde{k}_{Lm}^2 k_{Zm}\boldsymbol{\varphi}'_{zm}}{\tilde{k}_L^2 k_Z} \end{pmatrix} = \sum_{m=1}^{2(N+M)} \alpha_m{}' \begin{pmatrix} \dfrac{\tilde{k}_{Lm}^2\boldsymbol{\varphi}'_{om}}{\left(\tilde{k}_L - \tilde{k}_{Lm}\right)\tilde{k}_L^2} \\ \dfrac{\tilde{k}_{Lm}^2 k_{Zm}\boldsymbol{\varphi}'_{zm}}{\left(\tilde{k}_L - \tilde{k}_{Lm}\right)\tilde{k}_L^2 k_Z} \end{pmatrix}. \tag{176}$$

When applying relations $\tilde{k}_L^2 + k_Z^2 = \tilde{k}^2$ and $\tilde{k}_{Lm}^2 + k_{Zm}^2 = \tilde{k}^2$, the term in (Eq. 176) can be rewritten as:

$$\begin{pmatrix} \frac{\tilde{k}_{Lm}^2 \boldsymbol{\varphi}'_{om}(\tilde{k}_L+\tilde{k}_{Lm})}{(\tilde{k}_L-\tilde{k}_{Lm})\tilde{k}_L^2(\tilde{k}_L+\tilde{k}_{Lm})} \\ \frac{\tilde{k}_{Lm}^2 k_{Z\mathrm{m}} \boldsymbol{\varphi}'_{zm}(\tilde{k}_L+\tilde{k}_{Lm})}{(\tilde{k}_L-\tilde{k}_{Lm})\tilde{k}_L^2 k_Z(\tilde{k}_L+\tilde{k}_{Lm})} \end{pmatrix} = \begin{pmatrix} \frac{\tilde{k}_{Lm}^2 \boldsymbol{\varphi}'_{om}(\tilde{k}_L+\tilde{k}_{Lm})}{(\tilde{k}_L^2-\tilde{k}_{Lm}^2)\tilde{k}_L^2} \\ \frac{\tilde{k}_{Lm}^2 k_{Zm} \boldsymbol{\varphi}'_{zm}(\tilde{k}_L+\tilde{k}_{Lm})}{(\tilde{k}_L^2-\tilde{k}_{Lm}^2)\tilde{k}_L^2 k_Z} \end{pmatrix} =$$

$$= \begin{pmatrix} \frac{\tilde{k}_{Lm}^2 \boldsymbol{\varphi}'_{om}(\tilde{k}_L+\tilde{k}_{Lm})}{(\tilde{k}_L^2-\tilde{k}_{Lm}^2)\tilde{k}_L^2} \\ \frac{\tilde{k}_{Lm}^2 k_{Zm} \boldsymbol{\varphi}'_{zm}(\tilde{k}_L+\tilde{k}_{Lm})}{(\tilde{k}^2-\mathrm{k}_Z^2-\tilde{k}^2+k_{Zm}^2)\tilde{k}_L^2 k_Z} \end{pmatrix} = \begin{pmatrix} \frac{\tilde{k}_{Lm}^2 \boldsymbol{\varphi}'_{om}(\tilde{k}_L+\tilde{k}_{Lm})}{(\tilde{k}_L^2-\tilde{k}_{Lm}^2)\tilde{k}_L^2} \\ \frac{\tilde{k}_{Lm}^2 k_{Zm} \boldsymbol{\varphi}'_{zm}(\tilde{k}_L+\tilde{k}_{Lm})}{(\tilde{k}^2-k_Z^2-\tilde{k}^2+k_{Zm}^2)\tilde{k}_L^2 k_Z} \end{pmatrix} = \tag{177}$$

$$= \begin{pmatrix} \frac{\tilde{k}_{Lm}^2 \boldsymbol{\varphi}'_{om}(\tilde{k}_L+\tilde{k}_{Lm})}{(\tilde{k}_L^2-\tilde{k}_{Lm}^2)(\tilde{k}^2-k_Z^2)} \\ \frac{\tilde{k}_{Lm}^2 k_{Zm} \boldsymbol{\varphi}'_{zm}(\tilde{k}_L+\tilde{k}_{Lm})}{(k_{Zm}^2-k_Z^2)(\tilde{k}^2-k_Z^2)k_Z} \end{pmatrix}.$$

The nodal vector can be expressed as:

$$\begin{pmatrix} \overline{\boldsymbol{U}}_o \\ \overline{\boldsymbol{U}}_z \end{pmatrix} = \sum_{m=1}^{2(N+M)} \alpha_m{}' \begin{pmatrix} \frac{\tilde{k}_{Lm}^2(\tilde{k}_L+\tilde{k}_{Lm})\boldsymbol{\varphi}'_{om}}{(k_Z-k_{Zm})(k_Z+k_{Zm})(k_Z-\tilde{k})(k_Z+\tilde{k})} \\ \frac{\tilde{k}_{Lm}^2 k_{Zm}(\tilde{k}_L+\tilde{k}_{Lm})\boldsymbol{\varphi}'_{zm}}{(k_Z-k_{Zm})(k_Z+k_{Zm})(k_Z-\tilde{k})(k_Z+\tilde{k})k_Z} \end{pmatrix}. \tag{178}$$

Since the nodal vector in (Eq. 178) is expressed in the wavenumber domain, the nodal displacement vector in the space domain is the inverse Fourier transform of (Eq. 45):

$$\boldsymbol{U}(z)_o = \int_{-\infty}^{\infty} \overline{\boldsymbol{U}}_o \, e^{kz} dk_Z, \tag{179}$$

$$\boldsymbol{U}(z)_z = \int_{-\infty}^{\infty} \overline{\boldsymbol{U}}_z \, e^{kz} dk_Z. \tag{180}$$

Infinite integrals can be calculated as the limits of contour integrals applying Cauchy’s residue theorem [112]. By applying Cauchy’s theorem, we have:

$$\begin{gathered} \int_{-\infty}^{\infty} f(x)dx = \int_{-R}^{R} f(x)dx + \int_{C_R} f(z)dz = \oint_C f(z)dz = \\ = 2\pi i \sum\nolimits_{z_i \; inside \; C} res(f, z_i), \end{gathered} \tag{181}$$

where $R > 0$ and $C_R$is the semicircular arc given by $z = Re^{it}$, where $t \in [0, \pi]$ and $C = [-R, R] \cup C_R$ is a closed contour, in which a summation of the residues is taken over all the poles of f in the upper half plane.

The integrands (Eqs. 179, 180) are analytical functions of a complex variable except at poles $\pm k_{Zm}$, $\pm\tilde{k}$ and additionally at 0 for (Eq. 180) for each m-th mode. The contour which lies in the complex plain should encircle just the physically meaningful poles; thus poles $k_Z = \pm\tilde{k}$ and $k_Z = 0$ are discarded. For real valued poles $\pm k_{Zm}$ (when an elastic medium without energy dissipation is considered in the model) and for complex valued poles $\pm k_{Zm}$ (when a viscoelastic medium and/or energy dissipation is considered in the model), the integration paths are represented in (Fig. 4.13). In a case of real valued poles $\pm k_{Zm}$, m-th positive forward propagative mode should be included in the upper half-plane $(z > 0)$ with the positive $c_{grm} > 0$

group velocity whereas a negative backward propagative m-th mode should be included in the lower half-plane ($z < 0$) with negative $c_{grm} < 0$. The positive forward propagative mode propagates from the origin z_0 in positive direction, the negative backward propagative m-th mode propagates from the origin z_0 in negative direction.

Modes with the positive group velocity cause the mechanical energy to be transported in the positive $0Z$ direction. For most cases, the natural wavenumber and the group velocity of a propagating mode have the same sign as it is evident in (Fig. 2.8) and (Fig. 4.9). However, some modes can have wavenumbers and group velocities of the opposite sign within small frequency ranges. Selecting natural wavenumbers of the same sign as the corresponding group velocity will ensure that energy flows out from the excited region in the waveguide.

For complex poles $\pm k_{Zm}$, the m-th positive forward evanescing mode should be included in the upper half-plane ($z > 0$) with the positive $c_{enm} > 0$ energy velocity, and the m-th negative backward evanescing mode should be included in the lower half-plane ($z < 0$) with the negative $c_{enm} < 0$ energy velocity. For the positive propagating and evanescing modes in the closed integration path C for $z > 0$ (the negative propagating (evanescing) and unphysical modes lie outside the contour), Cauchy residue theorem (Eq. 181) yields:

$$\boldsymbol{U}(z)_o = \int_{-\infty}^{\infty} \overline{\boldsymbol{U}}_o\, e^{ik_{Zm}} dk_Z = \oint_C \overline{\boldsymbol{U}}_o e^{ik_{Zm}} dk_Z = 2\pi i \sum_{m=1}^{P} Res_{\overline{\boldsymbol{U}}_o}(k_{Zm}), \quad (182)$$

where P is the number of the positive going modes ($c_{grm} > 0$ or $c_{enm} > 0$). Since (Eq. 179) has a single singularity at $k_z = k_{zm}$, the m-th residue reads as:

$$Res_{\overline{\boldsymbol{U}}_o}(k_{zm}) = \lim_{k_z \to k_{zm}} (k_z - k_{zm})\, \overline{\boldsymbol{U}}_o e^{ik_z}, \quad (183)$$

(Eq. 179) can be rewritten as:

$$\begin{aligned}
\boldsymbol{U}(z)_o &= 2\pi i \sum_{m=1}^{P} \lim_{\substack{k_z \to k_{zm} \\ (\tilde{k}_L \to \tilde{k}_{Lm})}} (k_z - k_{zm})\, \overline{\boldsymbol{U}}_o e^{ik_{Zm}} = \\
&= 2\pi i \lim_{\substack{k_z \to k_{zm} \\ (\tilde{k}_L \to \tilde{k}_{Lm})}} \sum_{m=1}^{P} \alpha_m{}' \frac{(k_z - k_{zm})\tilde{k}_{Lm}^2(\tilde{k}_L + \tilde{k}_{Lm})\boldsymbol{\varphi'}_{om}}{(k_Z - k_{Zm})(k_Z + k_{Zm})(k_Z - \tilde{k})(k_Z + \tilde{k})} e^{ik_{Zm}(z - z_0)} = \\
&= 2\pi i \lim_{\substack{k_z \to k_{zm} \\ (\tilde{k}_L \to \tilde{k}_{Lm})}} \sum_{m=1}^{P} \alpha_m{}' \frac{\tilde{k}_{Lm}^2(\tilde{k}_L + \tilde{k}_{Lm})\boldsymbol{\varphi'}_{om}}{-(k_Z + k_{Zm})(\tilde{k}^2 - k_Z^2)} e^{ik_{Zm}(z - z_0)} = 2\pi i \cdot \quad (184) \\
&\cdot \lim_{\substack{k_z \to k_{zm} \\ (\tilde{k}_L \to \tilde{k}_{Lm})}} \sum_{m=1}^{P} \alpha_m{}' \frac{(\tilde{k}_L + \tilde{k}_{Lm})\boldsymbol{\varphi'}_{om}}{-(k_Z + k_{Zm})} e^{ik_{Zm}(z - z_0)} = \\
&= 2\pi i \sum_{m=1}^{P} \alpha_m{}' \frac{\tilde{k}_{Lm}\boldsymbol{\varphi'}_{om}}{-k_{Zm}} e^{ik_{Zm}(z - z_0)}.
\end{aligned}$$

Analogically, (Eq. 180) can be expressed as:

$$
\begin{aligned}
\boldsymbol{U}(z)_z &= 2\pi i \textstyle\sum_{m=1}^{P} \lim\limits_{\substack{k_z\to k_{zm}\\(\tilde{k}_L\to\tilde{k}_{Lm})}} (k_z - k_{zm})\, \overline{\boldsymbol{U}}_z e^{ik_{Zm}(z-z_0)} = \\
&= 2\pi i \lim\limits_{\substack{k_z\to k_{zm}\\(\tilde{k}_L\to\tilde{k}_{Lm})}} \textstyle\sum_{m=1}^{P} \alpha_m{}' \dfrac{\tilde{k}_{Lm}^2 k_{Zm}(\tilde{k}_L+\tilde{k}_{Lm})\boldsymbol{\varphi'}_{zm}}{(k_Z-k_{Zm})(k_Z+k_{Zm})(k_Z-\tilde{k})(k_Z+\tilde{k})k_Z}\, e^{ik_{Zm}(z-z_0)} = \\
&= 2\pi i \lim\limits_{\substack{k_z\to k_{zm}\\(\tilde{k}_L\to\tilde{k}_{Lm})}} \textstyle\sum_{m=1}^{P} \alpha_m{}' \dfrac{\tilde{k}_{Lm}^2 k_{Zm}(\tilde{k}_L+\tilde{k}_{Lm})\boldsymbol{\varphi'}_{zm}}{-(k_Z+k_{Zm})(\tilde{k}^2-k_z^2)k_Z}\, e^{ik_{Zm}(z-z_0)} = \\
&= 2\pi i \lim\limits_{\substack{k_z\to k_{zm}\\(\tilde{k}_L\to\tilde{k}_{Lm})}} \textstyle\sum_{m=1}^{P} \alpha_m{}' \dfrac{k_{Zm}(\tilde{k}_L+\tilde{k}_{Lm})\boldsymbol{\varphi'}_{zm}}{-k_Z(k_Z+k_{Zm})}\, e^{ik_{Zm}(z-z_0)} = \\
&= 2\pi i \textstyle\sum_{m=1}^{P} \alpha_m{}' \dfrac{\tilde{k}_{Lm}\boldsymbol{\varphi'}_{zm}}{-k_{Zm}}\, e^{ik_{Zm}(z-z_0)}.
\end{aligned}
\tag{185}
$$

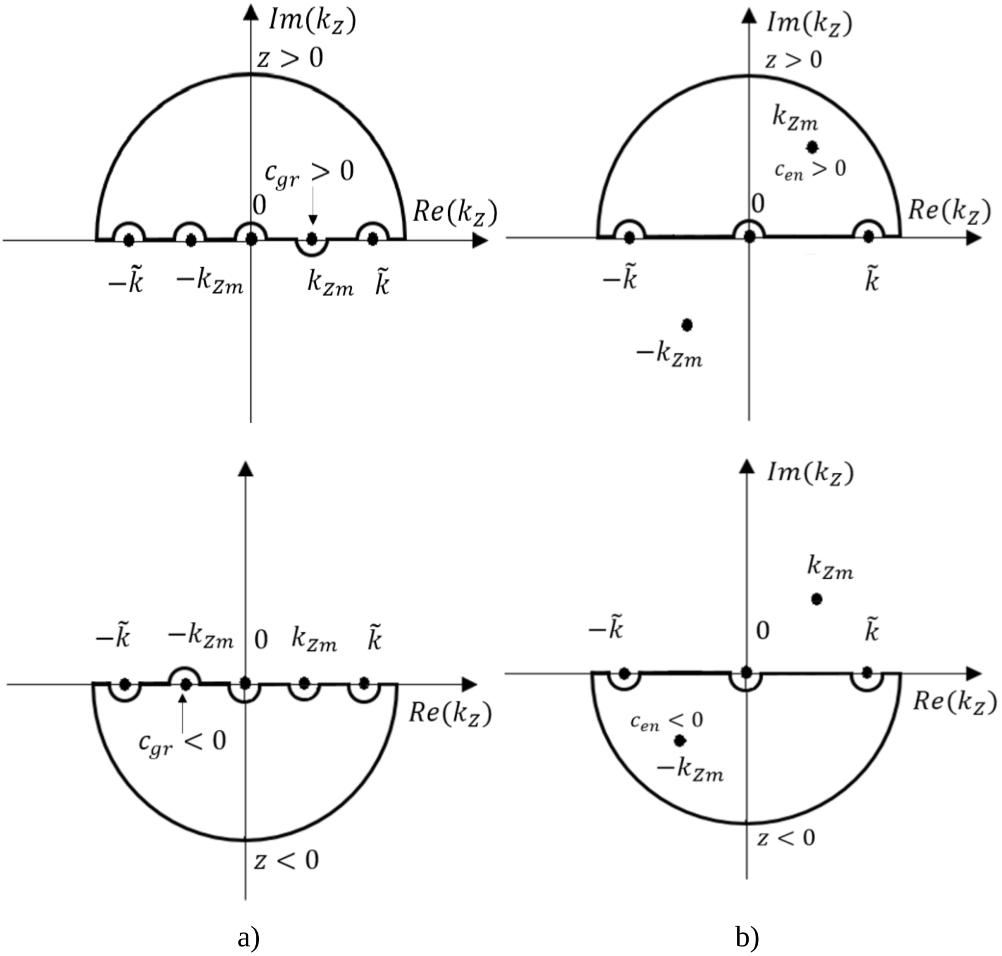

Fig. 4.13. Integration paths when the wavenumber (a) k_Z is real (no energy dissipation); (b) k_Z is complex (energy dissipation is present).

Finally, the displacements in the spatial domain for the response in $z > 0$ region have the following form:

$$\boldsymbol{U}(z) = \begin{pmatrix} \boldsymbol{U}(z)_o \\ \boldsymbol{U}(z)_z \end{pmatrix} = \sum_{m=1}^{P} \alpha_m^+ \boldsymbol{\varphi}_m e^{ik_{Zm}(z-z_0)}, \tag{186}$$

where

$$\alpha_m^+ = 2\pi i \frac{\boldsymbol{W}_m \overline{\boldsymbol{F}}}{\boldsymbol{W}_m \overline{\boldsymbol{F}} \boldsymbol{V}_m} \frac{\tilde{k}_L}{k_Z}. \tag{187}$$

The displacements in the $z > 0$ region are acquired by simply replacing wavenumber k_Z to $-k_Z$:

$$\boldsymbol{U}(z) = \begin{pmatrix} \boldsymbol{U}(z)_o \\ \boldsymbol{U}(z)_z \end{pmatrix} = \sum_{m=1}^{P} \alpha_m^- \boldsymbol{\varphi}_m e^{ik_{Zm}(z-z_0)}, \tag{188}$$

where

$$\alpha_m^- = -2\pi i \frac{\boldsymbol{W}_m \overline{\boldsymbol{F}}}{\boldsymbol{W}_m \overline{\boldsymbol{F}} \boldsymbol{V}_m} \frac{\tilde{k}_L}{k_Z}. \tag{189}$$

When displacements in (Eq. 186) or (Eq. 188) were calculated for each angular frequency ω, this displacement field in the frequency domain can be transformed into displacement field in the time domain applying the inverse Fourier transform (Eq. 44).

4.7 Concluding Remarks

The techniques of acquiring dispersion relations for the damped three-dimensional waveguide immersed in the perfect fluid were discussed, and analysis of the obtained wave modes was performed.

This enables further investigation of quasi-Scholte waves. Up to now, the available scientific publications have only paid scant attention to the 3D quasi-Scholte wave modes which propagate at the interference between the solid (the waveguide) and the fluid.

The coupling of two attenuation mechanisms due to the energy leakage and material damping showed that the models of the immersed waveguide used in this study support only the weak and moderate Rayleigh damping.

The adequacy of the solutions for more severe damping requires to additionally consider the complex conjugate of the wavenumber in the governing finite element formulation, which would lead to non-linear Eigenvalue problems.

Conclusions and Future Directions

One of the efficient methods to study the wave propagation phenomena in the linearly elastic medium is the Semi-Analytical Finite Element (SAFE) method. It enables to analyze waves in 3D waveguides which are uniform geometrically and physically along at least one direction by using 2D mesh discretization of the cross-section only. In this study, the SAFE Method was used to explore the characteristics of guided wave modes and forced wave propagation responses in a rectangular cross-section isotropic waveguide. It was shown that the SAFE model is capable of obtaining adequate results in terms of the wave dispersion curves, phase and group velocities, and also structural propagating wave modes in elastic and viscoelastic waveguides. So far, the SAFE models have mostly been used for waveguides of only light or moderate Rayleigh damping because of the inherent simplifying assumption that the complex part of the wavenumber is always very small. This approach leads to linear Eigenproblem equations, from which, the wave modes are obtained. In this work, the following new elaborations regarding modal and forced wave solutions obtained by the SAFE method were carried out.

In general, Rayleigh damping states proportional frequency dependence; therefore, it should be applied within a limited range of frequencies. The reason is that even in those cases when the physical and geometrical behavior of the waveguide is linear, the Eigenvalue problem still has to be considered as a non-linear one.

1. The full complex Eigenvalue equations have been formulated in order to cope with complex wavenumber exponents which may represent significantly damped waveguides. As an example, only the mass-proportional Rayleigh damping term was used. However, the stiffness-proportional damping component can be included as well without any changes to the computational algorithm.
2. A new approach to the construction of the dispersion relations of the damped wave modes has been proposed. In order to retain the linearity of the Eigenproblem, the solutions in terms of complex time exponents have to be calculated at prescribed modal wavenumbers. However, the wavenumbers are now fully complex and shall be treated as complex space exponents. Therefore, the dispersion relation is obtained as a surface above the complex wavenumber plane rather than a curve over the wavenumber axis.
3. The forced wave response analysis was performed by using the SAFE method for a 3D waveguide for elastic and viscoelastic homogenous materials. The forced response is obtained by using the normal wave modes superposition principle, where transient solutions are obtained via Fourier transformation. We demonstrated that the wave modes, as well as the combined forced responses of the waveguides to harmonic and general excitations during long time intervals, can be obtained at a much lower cost compared to the direct simulation of a waveguide as a solid 3D FE structure. The quantitative evaluation of the gain

cannot be estimated uniquely as it depends on the time interval over which the solution is necessary as well as on the complexity of the time law of excitation. The longer is the time interval form the beginning of the excitation and the less harmonic components does the excitation time law contain, the bigger is the gain. Practically, for the waves used in ultrasonic applications, the computational cost can be reduced many times. Among the advantages of SAFEM there is the ability to acquire steady forced propagating wave responses invariant in time and space. Moreover, SAFE may treat very long waves without any increase of the computational resource needs, while this always leads to difficulties of numerical calculation for the 3D FEM.

4. A good agreement of results obtained by using 3D FEM and SAFEM was demonstrated. This verification task has been performed by simulating sample wave signals of quite limited propagation duration. At such conditions, the same simulations can be performed by SAFEM and 3D FEM, and the results can be compared against each other. In such numerical experiments, the differences between the nodal displacements of the forced response did not exceed 2%.
5. The known approach for acquiring dispersion relations for an immersed plate was extended to the three-dimensional waveguide analysis under similar assumptions about the leaky two-dimensional waves.
6. The theoretical derivation of the forced response of the three-dimensional waveguide immersed into the perfect fluid was performed. This would enable to extract physically meaningful solutions. Furthermore, it would lead to further analysis of a propagating wave pulse, which is via Fourier transform considered as a superposition of evanescing and leaky modes and thus helps to gain fundamental insights into the propagation of leaky waves generated by a traveling impulse.

References

1. KAZYS, R, MAZEIKA, L, RAISUTIS, R, ZUKAUSKAS, E and SLITERIS, R. Application of Ultrasonic Guided Waves for NDE of Composite Structures. *Proceedings of the National Seminar and Exhibition on Non-Destructive Evaluation*. 2009. P. 236–239.
2. VOGT, Thomas Karl. *Determination of Material Properties Using Guidedwaves*. Imperial College of Science, Technology and Medicine London, 2002.
3. BILODEAU, M., QUAEGEBEUR, N. and MASSON, P. Design of a guided wave absorber for Structural Health Monitoring system development. *NDT and E International*. 2017. Vol. 88, no. March, p. 33–41. DOI 10.1016/j.ndteint.2017.03.003.
4. ZHANG, Hong, GAO, Bin, TIAN, Gui Yun, WOO, Wai Lok and BAI, Libing. Metal defects sizing and detection under thick coating using microwave NDT. *NDT and E International*. 2013. Vol. 60, p. 52–61. DOI 10.1016/j.ndteint.2013.07.002.
5. COLOMBO, Matteo and FELICETTI, Roberto. New NDT techniques for the assessment of fire-damaged concrete structures. *Fire Safety Journal*. 2007. Vol. 42, no. 6-7, p. 461–472. DOI 10.1016/j.firesaf.2006.09.002.
6. JULURI, Naresh. *INSPECTION OF COMPLEX STRUCTURES USING GUIDED WAVES*. Imperial College London, 2008.
7. RAIŠUTIS, Renaldas, KAŽYS, Rymantas, ŽUKAUSKAS, Egidijus, MAŽEIKA, Liudas and VLADIŠAUSKAS, Alfonsas. Application of Ultrasonic Guided Waves for Non-Destructive Testing of Defective CFRP Rods with Multiple Delaminations. *NDT & E International*. July 2010. Vol. 43, no. 5, p. 416–424. DOI 10.1016/j.ndteint.2010.04.001.
8. LOVEDAY, Philip W. and LONG, Craig S. Time Domain Simulation of Piezoelectric Excitation of Guided Waves in Rails Using Waveguide Finite Elements. In : TOMIZUKA, Masayoshi, YUN, Chung-Bang and GIURGIUTIU, Victor (eds.). April 2007. p. 65290V.
9. SOROHAN, Ştefan, CONSTANTIN, Nicolae, GĂVAN, Mircea and ANGHEL, Viorel. Extraction of Dispersion Curves for Waves Propagating in Free Complex Waveguides by Standard Finite Element Codes. *Ultrasonics*. May 2011. Vol. 51, no. 4, p. 503–515. DOI 10.1016/j.ultras.2010.12.003.
10. KAZYS, Rymantas, MAZEIKA, Liudas, SLITERIS, Reimondas and RAISUTIS, Renaldas. Measurement of viscosity of highly viscous non-Newtonian fluids by means of ultrasonic guided waves. *Ultrasonics*. 2014. Vol. 54, no. 4, p. 1104–1112. DOI 10.1016/j.ultras.2014.01.007.
11. FAN, Zheng. *Applications of guided wave propagation on waveguides with irregular cross-section*. Imperial College London, 2010.
12. BAUSE, Fabian, RAUTENBERG, Jens, FELDMANN, Nadine, WEBERSEN, Manuel, CLAES, Leander, GRAVENKAMP, Hauke and HENNING, Bernd. Ultrasonic transmission measurements in the characterization of viscoelasticity utilizing polymeric waveguides. *Measurement Science and Technology*. 2016. Vol. 27, no. 10, p. 1–47. DOI 10.1088/0957-0233/27/10/105601.

13. HAYASHI, Takahiro, KAWASHIMA, Koichiro, SUN, Zongqi and ROSE, Joseph L. Analysis of flexural mode focusing by a semianalytical finite element method. *The Journal of the Acoustical Society of America*. 2003. Vol. 113, no. 3, p. 1241–1248. DOI 10.1121/1.1543931.

14. LOVEDAY, Philip W. Semi-Analytical Finite Element Analysis of Elastic Waveguides Subjected to Axial Loads. *Ultrasonics*. 2009. Vol. 49, no. 3, p. 298–300. DOI 10.1016/j.ultras.2008.10.018.

15. POCHHAMMER, L. Ueber die Fortpflanzungsgeschwindigkeiten kleiner Schwingungen in einem unbegrenzten isotropen Kreiscylinder. *Journal für die reine und angewandte Mathematik*. 1876. Vol. 81, p. 324–336.

16. CHREE, C. The Equations of an Isotropic Elastic Solid in Polar and Cylindrical Co-ordinates their Solution and Application. *Transactions of the Cambridge Philosophical Society*. 1889. Vol. 14, p. 250–369.

17. VIKTOROV, Igor A. *Rayleigh and Lamb Waves: Physical Theory and Applications*. Plenum press, 1967.

18. GRAFF, Karl F. *Wave Motion in Elastic Solids*. Oxford : The Clarendon Press, 1975. ISBN 0486667456.

19. LIANG, Yue. *ULTRASONIC VIBRATION POTENTIAL IN STRUCTURAL HEALTH MONITORING FOR PLATE-LIKE STRUCTURES*. The Pennsylvania State University, 2014.

20. LOWE, Stuart. *Plate Waves for the NDT of Diffusion Bonded Titanium*. London Imperial College of Science, 1992.

21. HLADKY-HENNION, A.-C. Finite Element Analysis of the Propagation of Acoustic Waves in Waveguides. *Journal of Sound and Vibration*. July 1996. Vol. 194, no. 2, p. 119–136. DOI 10.1006/jsvi.1996.0349.

22. DAMLJANOVIĆ, Vesna and WEAVER, Richard L. Forced Response of a Cylindrical Waveguide with Simulation of the Wavenumber Extraction Problem. *The Journal of the Acoustical Society of America*. April 2004. Vol. 115, no. 4, p. 1582–1591. DOI 10.1121/1.1675818.

23. ZIENKIEWICZ, Olgierd Cecil and TAYLOR, Robert Leroy. *The Finite Element Method: Solid Mechanics Vol. 2*. Butterworth-Heinemann, 2000.

24. RENNO, Jamil M. and MACE, Brian R. On the Forced Response of Waveguides Using the Wave and Finite Element Method. *Journal of Sound and Vibration*. December 2010. Vol. 329, no. 26, p. 5474–5488. DOI 10.1016/j.jsv.2010.07.009.

25. RENNO, Jamil M. and MACE, Brian R. Calculating the Forced Response of Two-Dimensional Homogeneous Media Using the Wave and Finite Element Method. *Journal of Sound and Vibration*. November 2011. Vol. 330, no. 24, p. 5913–5927. DOI 10.1016/j.jsv.2011.06.011.

26. MANCONI, Elisabetta and SOROKIN, Sergey. On the Effect of Damping on Dispersion Curves in Plates. *International Journal of Solids and Structures*. June 2013. Vol. 50, no. 11-12, p. 1966–1973. DOI 10.1016/j.ijsolstr.2013.02.016.

27. PALERMO, Antonio and MARZANI, Alessandro. Ultrafast Wave Finite Element Method for the computation of dispersion properties in periodic viscoelastic waveguides. *8th European Workshop On Structural Health Monitoring (EWSHM)*.

2016. No. July 2016, p. 5–8.

28. SILVA, P. B., GOLDSTEIN, A. L. and ARRUDA, J. R F. Building Spectral Element Dynamic Matrices Using Finite Element Models of Waveguide Slices and Elastodynamic Equations. *Shock and Vibration*. 2013. Vol. 20, no. 3, p. 439–458. DOI 10.3233/SAV-120760.

29. GRAVENKAMP, Hauke, SONG, Chongmin and PRAGER, Jens. A numerical approach for the computation of dispersion relations for plate structures using the Scaled Boundary Finite Element Method. *Journal of Sound and Vibration*. 2012. Vol. 331, no. 11, p. 2543–2557. DOI 10.1016/j.jsv.2012.01.029.

30. GRAVENKAMP, Hauke, PRAGER, Jens, SAPUTRA, Albert A. and SONG, Chongmin. The simulation of Lamb waves in a cracked plate using the scaled boundary finite element method. *The Journal of the Acoustical Society of America*. 2012. Vol. 132, no. 3, p. 1358–1367. DOI 10.1121/1.4740478.

31. GRAVENKAMP, Hauke, BIRK, Carolin and SONG, Chongmin. Computation of dispersion curves for embedded waveguides using a dashpot boundary condition. *The Journal of the Acoustical Society of America*. 2014. Vol. 135, no. 3, p. 1127–1138. DOI 10.1121/1.4864303.

32. GRAVENKAMP, Hauke, BIRK, Carolin and SONG, Chongmin. Simulation of Elastic Guided Waves Interacting with Defects in Arbitrarily Long Structures Using the Scaled Boundary Finite Element Method. *Journal of Computational Physics*. 2015. Vol. 295, p. 438–455. DOI 10.1016/j.jcp.2015.04.032.

33. MU, Jing and ROSE, Joseph L. Guided Wave Propagation and Mode Differentiation in Hollow Cylinders with Viscoelastic Coatings. *The Journal of the Acoustical Society of America*. 2008. Vol. 124, no. 2, p. 866–874. DOI 10.1121/1.2940586.

34. HAYASHI, Takahiro, SONG, Won-Joon and ROSE, Joseph L. Guided Wave Dispersion Curves for a Bar with an Arbitrary Cross-Section, a Rod and Rail Example. *Ultrasonics*. 2003. Vol. 41, no. 3, p. 175–183. DOI 10.1016/S0041-624X(03)00097-0.

35. VIOLA, Erasmo, MARZANI, Alessandro and BARTOLI, Ivan. Numerical Evaluation of Semi-analytical Finite Element (SAFE) Method for Plates, Rods and Hollow Cylinders. In : *Mechanical Vibration: Where do we Stand?* Vienna : Springer Vienna, 2006. p. 123–138.

36. DOYLE, James F. *Wave Propagation in Structures: Spectral Analysis Using Fast Discrete Fourier Transforms*. New York, NY : Springer New York, 1997. Mechanical Engineering Series. ISBN 978-1-4612-7304-2.

37. TREYSSÈDE, F., NGUYEN, K. L., BONNET-BENDHIA, A. S. and HAZARD, C. Finite Element Computation of Trapped and Leaky Elastic Waves in Open Stratified Waveguides. *Wave Motion*. 2014. Vol. 51, no. 7, p. 1093–1107. DOI 10.1016/j.wavemoti.2014.05.003.

38. HAN, Je-Heon, KIM, Yong-Joe and KARKOUB, Mansour. Wave propagation modeling of fluid-filled pipes using hybrid analytical/two-dimensional finite element method. *Wave Motion*. 2014. Vol. 51, no. 7, p. 1193–1208. DOI 10.1016/j.wavemoti.2014.07.006.

39. QUINTANILLA, F. Hernando, FAN, Z., LOWE, M. J. S. and CRASTER, R. V.

Guided waves’ dispersion curves in anisotropic viscoelastic single- and multi-layered media. *Proceedings of the Royal Society A: Mathematical, Physical and Engineering Science*. 2015. Vol. 471, no. 2183, p. 20150268. DOI 10.1098/rspa.2015.0268.

40. LAGASSE, P. E. Higher-Order Finite-Element Analysis of Topographic Guides Supporting Elastic Surface Waves. *The Journal of the Acoustical Society of America*. April 1973. Vol. 53, no. 4, p. 1116–1122. DOI 10.1121/1.1913432.
41. AALAMI, B. Waves in Prismatic Guides of Arbitrary Cross Section. *American Society of Mechanical Engineers*. 1973. Vol. 40, no. 4, p. 1067–1072.
42. GAVRIĆ, L. Computation of Propagative Waves in Free Rail Using a Finite Element Technique. *Journal of Sound and Vibration*. August 1995. Vol. 185, no. 3, p. 531–543. DOI 10.1006/jsvi.1995.0398.
43. BARTOLI, Ivan, MARZANI, Alessandro, LANZA DI SCALEA, Francesco and VIOLA, Erasmo. Modeling wave propagation in damped waveguides of arbitrary cross-section. *Journal of Sound and Vibration*. 2006. Vol. 295, no. 3-5, p. 685–707. DOI 10.1016/j.jsv.2006.01.021.
44. MARZANI, Alessandro and BARTOLI, Ivan. High frequency waves propagating in octagonal bars: A low cost computation algorithm. *Algorithms*. 2009. Vol. 2, no. 1, p. 227–246. DOI 10.3390/a2010227.
45. GRAVENKAMP, Hauke, MAN, Hou, SONG, Chongmin and PRAGER, Jens. The computation of dispersion relations for three-dimensional elastic waveguides using the Scaled Boundary Finite Element Method. *Journal of Sound and Vibration*. 2013. Vol. 332, no. 15, p. 3756–3771. DOI 10.1016/j.jsv.2013.02.007.
46. DROZDZ, Mickael Brice. *Efficient Finite Element Modelling of Ultrasound in Elastic Media*. Imperial College of Science Technology and Medicine London, 2008.
47. GAO, Huidong. *Ultrasonic guided wave mechanics for composite material structural health monitoring*. The Pennsylvania State University, 2007.
48. TREYSSEDE, F. and FRIKHA, A. A semi-analytical finite element method for elastic guided waves propagating in helical structures. *Proceedings - European Conference on Noise Control*. 2008.
49. TREYSSÈDE, Fabien, FRIKHA, Ahmed and CARTRAUD, Patrice. Mechanical modeling of helical structures accounting for translational invariance. Part 2: Guided wave propagation under axial loads. *International Journal of Solids and Structures*. 2013. Vol. 50, no. 9, p. 1383–1393. DOI 10.1016/j.ijsolstr.2013.01.006.
50. PREDOI, Mihai V., CASTAINGS, Michel, HOSTEN, Bernard and BACON, Christophe. Wave Propagation along Transversely Periodic Structures. *The Journal of the Acoustical Society of America*. 2007. Vol. 121, no. 4, p. 1935–1944. DOI 10.1121/1.2534256.
51. JIANG, W K. a Three-Dimensional Semi-Analytical Model for Predicting Offshore Pile Driving Noise. In : *11th World Congress on Computational Mechanics, 5th European Conference on Computational Mechanics, 6th European Conference on Computational Fluid Dynamics*. 2014.
52. DENG, Qingpeng, JIANG, Weikang, TAN, Mingyi and XING, Jing Tang. Modeling of offshore pile driving noise using a semi-analytical variational formulation. *Applied Acoustics*. March 2016. Vol. 104, p. 85–100. DOI 10.1016/j.apacoust.2015.11.002.

53. TSOUVALAS, A and METRIKINE, A V. A Three-Dimensional Semi-analytical Model for the Prediction of Underwater Noise Generated by Offshore Pile Driving. In : ZHOU, Y., LIU, Y., HUANG, L. and HODGES, D. (eds.), *Fluid-Structure-Sound Interactions and Control. Lecture Notes in Mechanical Engineering*. Springer, Berlin, Heidelberg, 2014. p. 259–264. ISBN 978-3-662-48866-9.

54. CORTES, Daniel H., DATTA, Subhendu K. and MUKDADI, Osama M. Dispersion of Elastic Guided Waves in Piezoelectric Infinite Plates with Inversion Layers. *International Journal of Solids and Structures*. September 2008. Vol. 45, no. 18-19, p. 5088–5102. DOI 10.1016/j.ijsolstr.2008.05.010.

55. KALKOWSKI, Michał K., RUSTIGHI, Emiliano and WATERS, Timothy P. Semi-Analytical Modelling of Piezoelectric Excitation of Guided Waves. In : KUNDU, Tribikram (ed.), *Health Monitoring of Structural and Biological Systems*. March 2015. p. 943820.

56. AHMAD, Z. A. B., VIVAR-PEREZ, J. M. and GABBERT, U. Semi-analytical finite element method for modeling of lamb wave propagation. *CEAS Aeronautical Journal*. 2013. Vol. 4, no. 1, p. 21–33. DOI 10.1007/s13272-012-0056-6.

57. AHMAD, Z. A B and GABBERT, U. Simulation of Lamb wave reflections at plate edges using the semi-analytical finite element method. *Ultrasonics*. 2012. Vol. 52, no. 7, p. 815–820. DOI 10.1016/j.ultras.2012.05.008.

58. BARTOLI, Ivan. *Structural health monitoring by Bayesian updating*. University of California, San Diego, 2007.

59. MAZZOTTI M. *Numerical Methods for the Dispersion Analysis of Guided Waves*. University of Bologna, 2013.

60. LUO, Wei. *Ultrasonic Guided Waves and Waves Scattering in Viscoelastic Coated Hollow Cylinders*. The Pennsylvania State University, 2005.

61. TREYSSÈDE, F. Spectral Element Computation of High-Frequency Leaky Modes in Three-Dimensional Solid Waveguides. *Journal of Computational Physics*. 2016. Vol. 314, p. 341–354. DOI 10.1016/j.jcp.2016.03.029.

62. QI, Xue. *Ultrasonic Guided Waves for Defect Characterization in Composite Structures*. The Pennsylvania State University, 2011.

63. CASTAINGS, Michel and LOWE, Michael. Finite Element Model for Waves Guided along Solid Systems of Arbitrary Section Coupled to Infinite Solid Media. *The Journal of the Acoustical Society of America*. 2008. Vol. 123, no. 2, p. 696–708. DOI 10.1121/1.2821973.

64. FAN, Z., LOWE, M. J. S., CASTAINGS, M. and BACON, C. Torsional Waves Propagation along a Waveguide of Arbitrary Cross Section Immersed in a Perfect Fluid. *The Journal of the Acoustical Society of America*. 2008. Vol. 124, no. 4, p. 2002–2010. DOI 10.1121/1.2968677.

65. NGUYEN, Khac-Long, TREYSSEDE, Fabien, BONNET-BEN DHIA, Anne-Sophie and HAZARD, Christophe. Computation of Dispersion Curves in Elastic Waveguides of Arbitrary Cross-section embedded in Infinite Solid Media. In : *13th International Symposium on Nondestructive Characterization of Materials*. March 2013.

66. NGUYEN, K. L., TREYSSÈDE, F. and HAZARD, C. Numerical modeling of three-dimensional open elastic waveguides combining semi-analytical finite element and

perfectly matched layer methods. *Journal of Sound and Vibration*. 2015. Vol. 344, p. 158–178. DOI 10.1016/j.jsv.2014.12.032.

67. FRANÇOIS, S., SCHEVENELS, M., GALVÍN, P., LOMBAERT, G. and DEGRANDE, G. A 2.5D coupled FE-BE methodology for the dynamic interaction between longitudinally invariant structures and a layered halfspace. *Computer Methods in Applied Mechanics and Engineering*. 2010. Vol. 199, no. 23-24, p. 1536–1548. DOI 10.1016/j.cma.2010.01.001.

68. MAZZOTTI, M., BARTOLI, I., MARZANI, A. and VIOLA, E. A coupled SAFE-2.5D BEM approach for the dispersion analysis of damped leaky guided waves in embedded waveguides of arbitrary cross-section. *Ultrasonics*. 2013. Vol. 53, no. 7, p. 1227–1241. DOI 10.1016/j.ultras.2013.03.003.

69. GRAVENKAMP, Hauke, BIRK, Carolin and VAN, Jason. Modeling ultrasonic waves in elastic waveguides of arbitrary cross-section embedded in infinite solid medium. *Computers and Structures*. 2015. Vol. 149, p. 61–71. DOI 10.1016/j.compstruc.2014.11.007.

70. GRAVENKAMP, Hauke, BIRK, Carolin and SONG, Chongmin. Numerical modeling of elastic waveguides coupled to infinite fluid media using exact boundary conditions. *Computers and Structures*. 2014. Vol. 141, p. 36–45. DOI 10.1016/j.compstruc.2014.05.010.

71. HAYASHI, Takahiro and INOUE, Daisuke. Numerical Analysis of Leaky Lamb Wave Propagation Using a Semi-Analytical Finite Element Method. *41st Annual Review of Progress in Quantitative Nondestructive Evaluation AIP Conf. Proc.* 2015. Vol. 695, p. 695–702. DOI 10.1063/1.4914670.

72. SHEN, Yanfeng and GIURGIUTIU, Victor. Effective Non-Reflective Boundary for Lamb Waves: Theory, Finite Element Implementation, and Applications. *Wave Motion*. November 2015. Vol. 58, p. 22–41. DOI 10.1016/j.wavemoti.2015.05.009.

73. RYDEN, Nils, PARK, Choon B., ULRIKSEN, Peter and MILLER, Richard D. Lamb Wave Analysis for Non-Destructive Testing of Concrete Plate Structures. *Symposium on the Application of Geophysics to Engineering and Environmental Problems 2003*. 2003. No. 1945, p. 782–793. DOI 10.4133/1.2923224.

74. ONEN, Onursal and UZ, Yusuf Can. Investigation of Scholte and Stoneley waves in multi-layered systems. *Physics Procedia*. 2015. Vol. 70, p. 217–221. DOI 10.1016/j.phpro.2015.08.138.

75. LAMKANFI, Ebrahim, DECLERCQ, Nico F., VAN PAEPEGEM, Wim and DEGRIECK, Joris. Scholte-Stoneley waves on an immersed solid dihedral: Generation, propagation and scattering effects. *Ultrasonics*. 2014. Vol. 54, no. 6, p. 1685–1691. DOI 10.1016/j.ultras.2014.02.022.

76. SHULL., Peter J. *Nondestructive Evaluation: Theory, Techniques and Applications*. New York : Marcel Dekker, Inc, 2002. ISBN 0824788729.

77. KRAUTKRAMER, J. and KRAUTKRAMER, H. *Ultrasonic testing of materials*. 4. Berlin : Springer-Verlag, 1990. ISBN 978-3-662-10680-8.

78. NAGY, Peter B and NAYFEH, Adnan H. *Viscosity-induced attenuation of longitudinal guided waves in fluid-loaded rods*. 1996.

79. TREYSSÈDE, Fabien and LAGUERRE, Laurent. Numerical and Analytical

Calculation of Modal Excitability for Elastic Wave Generation in Lossy Waveguides. *The Journal of the Acoustical Society of America*. 2013. Vol. 133, no. 6, p. 3827–3837. DOI 10.1121/1.4802651.

80. RUSOVICI, R. *Modeling of Shock Propagation and Attenuation in Viscoelastic Components*. Virginia Polytechnic Institute, 1999.

81. QAISAR, Mohammad. Attenuation Properties of Viscoelastic Material. In : *Scattering and Attenuation of Seismic Waves, Part II*. Basel : Birkhäuser Basel, 1989. p. 703–713.

82. SIMONETTI, Francesco. *Sound Propagation in Lossless Waveguides Coated with Attenuative Materials*. Imperial College London, 2003.

83. SUWAL, Sajana. Comparative study of 1D codes for Site Response Analyses. *International Journal of Lanslide and Environment*. 2014. No. 2, p. 24–31.

84. SPEARS, R. E. and JENSEN, S. R. Approach for Selection of Rayleigh Damping Parameters Used for Time History Analysis. *Journal of Pressure Vessel Technology*. 2012. DOI 10.1115/1.4006855.

85. BARSHINGER, James N. and ROSE, Joseph L. Guided wave propagation in an elastic hollow cylinder coated with a viscoelastic material. *IEEE Transactions on Ultrasonics, Ferroelectrics, and Frequency Control*. 2004. Vol. 51, no. 11, p. 1547–1556. DOI 10.1109/TUFFC.2004.1367496.

86. LOWE, M J S. Matrix Techniques for Modeling Ultrasonic-Waves in Multilayered Media. *Ieee Transactions on Ultrasonics Ferroelectrics and Frequency Control*. 1995. Vol. 42, no. 4, p. 525–542. DOI 10.1109/58.393096.

87. MCDANIEL, J. G., DUPONT, P. and SALVINO, L. A Wave Approach to Estimating Frequency-Dependent Damping under Transient Loading. *Journal of Sound and Vibration*. 2000. Vol. 231, no. 2, p. 433–449. DOI 10.1006/jsvi.1999.2723.

88. VASUDEVA, Sumit, KAPANIA, Rakesh and CLIFF, Eugene. Estimation of Elastic and Damping Characteristics of Viscoelastically Constrained Carbon Strands. In : *47th AIAA/ASME/ASCE/AHS/ASC Structures, Structural Dynamics, and Materials Conference 14th AIAA/ASME/AHS Adaptive Structures Conference 7th*. Reston, Virigina : American Institute of Aeronautics and Astronautics, May 2006. ISBN 978-1-62410-040-6.

89. ZLATEV, Zahari. *Ultrasonic Guided Wave Propagation in Pipes Coated with Viscoelastic Materials*. Brunel University, 2014.

90. SANCHEZ-SALINERO, I., ROESSET, J. M., STOKOE, I. I., & KENNETH, H. *Analytical Studies of Body Wave of Propagation and Attenuation*. Austin, 1986.

91. SEMBLAT, J. F. Rheological Interpretation of Rayleigh Damping. *Journal of Sound and Vibration*. 1997. Vol. 206, no. 5, p. 741–744. DOI 10.1006/jsvi.1997.1067.

92. AHMAD, Z a B. *Numerical Simulations of Lamb waves in plates using a semi-analytical finite element method*. Otto von Guericke University Magdeburg, 2011.

93. R. BARAUSKAS, R. BELEVIČIUS, R. Kačianauskas. *Baigtinių elementų metodo pagrindai*. Vilnius : “Technika,” 2004.

94. VIOLA, Erasmo, MARZANI, Alessandro and BARTOLI, Ivan. Semi-analytical Formulation for Guided Wave Propagation. In : *Mechanical Vibration: Where do we Stand?* Vienna : Springer Vienna, 2005. p. 105–121.

95. HAYASHI, Takahiro, TAMAYAMA, Chiga and MURASE, Morimasa. Wave Structure Analysis of Guided Waves in a Bar with an Arbitrary Cross-Section. *Ultrasonics*. 2006. Vol. 44, no. 1, p. 17–24. DOI 10.1016/j.ultras.2005.06.006.

96. GAVRIĆ, L. Computation of propagative waves in free rail using a finite element technique. *Journal of Sound and Vibration*. 1995. Vol. 185, no. 3, p. 531–543. DOI 10.1006/jsvi.1995.0398.

97. WAKI, Y., MACE, B. R. and BRENNAN, M. J. Numerical issues concerning the wave and finite element method for free and forced vibrations of waveguides. *Journal of Sound and Vibration*. 2009. Vol. 327, no. 1-2, p. 92–108. DOI 10.1016/j.jsv.2009.06.005.

98. RAO, Jing, RATASSEPP, Madis, LISEVYCH, Danylo, HAMZAH CAFFOOR, Mahadhir and FAN, Zheng. On-Line Corrosion Monitoring of Plate Structures Based on Guided Wave Tomography Using Piezoelectric Sensors. *Sensors*. 2017. Vol. 17, no. 12, p. 2882. DOI 10.3390/s17122882.

99. HAYASHI, Takahiro and INOUE, Daisuke. Calculation of Leaky Lamb Waves with a Semi-Analytical Finite Element Method. *Ultrasonics*. August 2014. Vol. 54, no. 6, p. 1460–1469. DOI 10.1016/j.ultras.2014.04.021.

100. ZUO, Peng, YU, Xudong and FAN, Zheng. Numerical Modeling of Embedded Solid Waveguides Using SAFE-PML Approach Using a Commercially Available Finite Element Package. *NDT and E International*. 2017. Vol. 90, no. March, p. 11–23. DOI 10.1016/j.ndteint.2017.04.003.

101. ÖNEN, Onursal. Dispersion and Sensitivity Analysis of Quasi-Scholte Wave Liquid Sensing by Analytical Methods. *Journal of Sensors*. 2017. P. 1–9. DOI 10.1155/2017/9876076.

102. MAZZOTTI, M., MARZANI, A. and BARTOLI, I. Dispersion analysis of leaky guided waves in fluid-loaded waveguides of generic shape. *Ultrasonics*. January 2014. Vol. 54, no. 1, p. 408–418. DOI 10.1016/j.ultras.2013.06.011.

103. ZUO, Peng and FAN, Zheng. SAFE-PML approach for modal study of waveguides with arbitrary cross sections immersed in inviscid fluid. *Journal of Sound and Vibration* [online]. 2017. Vol. 406, p. 181–196. DOI 10.1016/j.jsv.2017.06.001. Available from: http://dx.doi.org/10.1016/j.jsv.2017.06.001

104. BERNARD, A., LOWE, M. J. S. and DESCHAMPS, M. Guided Waves Energy Velocity in Absorbing and Non-Absorbing Plates. *The Journal of the Acoustical Society of America*. 2001. Vol. 110, no. 1, p. 186–196. DOI 10.1121/1.1375845.

105. HAYASHI, Takahiro. Guided Wave Dispersion Curves Derived with a Semianalytical Finite Element Method and Its Applications to Nondestructive Inspection. *Japanese Journal of Applied Physics*. May 2008. Vol. 47, no. 5, p. 3865–3870. DOI 10.1143/JJAP.47.3865.

106. INOUE, Daisuke and HAYASHI, Takahiro. Transient Analysis of Leaky Lamb Waves with a Semi-Analytical Finite Element Method. *Ultrasonics*. September 2015. Vol. 62, p. 80–88. DOI 10.1016/j.ultras.2015.05.004.

107. THOMPSON, Donald O. and CHIMENTI, Dale E. (eds.). *Review of Progress in Quantitative Nondestructive Evaluation*. Boston, MA : Springer US, 1995. ISBN 978-1-4613-5819-0.

108. KIEŁCZYŃSKI, P., SZALEWSKI, M. and BALCERZAK, A. Effect of a viscous liquid loading on Love wave propagation. *International Journal of Solids and Structures*. 2012. Vol. 49, no. 17, p. 2314–2319. DOI 10.1016/j.ijsolstr.2012.04.030.

109. BRUM, J., BERNAL, M., GENNISSON, J. L. and TANTER, M. In vivo evaluation of the elastic anisotropy of the human Achilles tendon using shear wave dispersion analysis. *Physics in Medicine and Biology*. 2014. Vol. 59, no. 3, p. 505–523. DOI 10.1088/0031-9155/59/3/505.

110. NGUYEN, Thu-Mai, COUADE, M., BERCOFF, J. and TANTER, M. Assessment of viscous and elastic properties of sub-wavelength layered soft tissues using shear wave spectroscopy: Theoretical framework and in vitro experimental validation. *IEEE Transactions on Ultrasonics, Ferroelectrics and Frequency Control*. 2011. Vol. 58, no. 11, p. 2305–2315. DOI 10.1109/TUFFC.2011.2088.

111. SUN, Hong Xiang and ZHANG, Shu Yi. Thermoviscoelastic finite element modeling of laser-generated ultrasound in viscoelastic plates. *Journal of Applied Physics*. 2010. Vol. 108, no. 12. DOI 10.1063/1.3520675.

112. MORSE, P. M. and FESHBACH, H. *Methods of Theoretical Physics*. New York : McGraw-Hill, 1953.

List of Publications

Papers in Master List Journals of Institute of Scientific Information (ISI)

1. Barauskas, Rimantas; **Nečiūnas, Audrius**; Patašius, Martynas. (2016). Elastic Wave Simulation Based on Modal Excitation in 3D Medium // Journal of Vibroengineering. Kaunas: JVE International. ISSN 1392-8716. 2016, Vol. 18, iss. 8, pp. 5321–5336. DOI: 10.21595/jve.2016.18101.
2. Barauskas, Rimantas; **Nečiūnas, Audrius**; Patašius, Martynas. (2018). Calculating Dispersion Relations for Waveguide Immersed in Perfect Fluid // Mathematical Modelling and Analysis, 2018, *23*(2), pp. 309–326. DOI: 10.3846/mma.2018.019.

SL344. 2018-05-31, 13,5 leidyb. apsk. l. Tiražas 14 egz. Užsakymas 195 .
Išleido Kauno technologijos universitetas, K. Donelaičio g. 73, 44249 Kaunas
Spausdino leidyklos „Technologija“ spaustuvė, Studentų g. 54, 51424 Kaunas